CCM-79-1

Center for Composite Materials

PROPERTIES OF SMC COMPOSTIES

D. G. TAGGART
R. B. PIPES
R. A. BLAKE
J. W. GILLESPIE, JR.
R. PRABHAKARAN
J. M. WHITNEY

College of Engineering
University of Delaware
Newark, Delaware

DISCLAIMER NOTICE

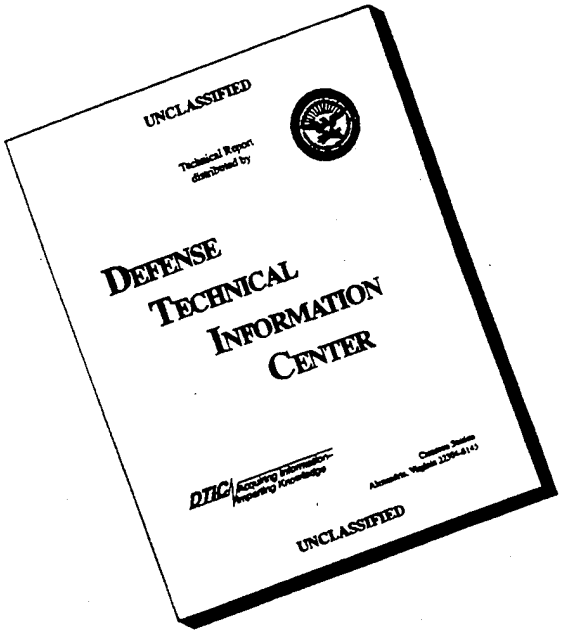

THIS DOCUMENT IS BEST QUALITY AVAILABLE. THE COPY FURNISHED TO DTIC CONTAINED A SIGNIFICANT NUMBER OF PAGES WHICH DO NOT REPRODUCE LEGIBLY.

Properties of SMC Composites

D. G. Taggart
R. B. Pipes
R. A. Blake
J. W. Gillespie, Jr.
R. Prabhakaran*
J. M. Whitney*

Center for Composite Materials
University of Delaware
Newark, Delaware 19711

February 1, 1979

Prepared for:

General Motors Technical Center
Manufacturing Development
Warren, Michigan 48090

---

*Consultants

Abstract

The mechanical properties of five glass fiber sheet molding compounds are investigated in this research program. The materials studied are SMC-25, SMC-30, SMC-65, SMC-C20/R30 and XMC-3. The specific properties include the tensile, compressive and shear response, as well as the strain rate sensitivity, impact resistance, notch sensitivity, statistical strength properties and bolted joint characteristics. A discussion of experimental test methods includes an evaluation of three shear test methods and a description of non-destructive inspection techniques.

TABLE OF CONTENTS

LIST OF TABLES

LIST OF FIGURES

LIST OF FIGURES (Continued)

1. INTRODUCTION

The purpose of this study is to investigate the mechanical properties of various sheet molding compound composites. The materials which were tested are all glass fiber reinforced polyester composites. The SMC-25, SMC-30 and SMC-65 materials contain randomly oriented short glass fibers. The weight fraction of fibers is 25%, 30% and 65%, respectively, and the average fiber length is approximately one inch. The SMC-C20/R30 composite has unidirectionally oriented continuous fibers in the surface plies with randomly oriented short fibers in the center. The XMC-3 material consists of continuous fibers which are oriented approximately $\pm 6°$ to the longtidinal material axis.

In order to effectively design components molded from sheet molding compounds, it is first necessary to determine the many mechanical properties. The intrinsic strength and stiffness properties for these composites were measured in tension, compression and inplane shear. The directional variation of these properties was also investigated. The effect of strain rate on ultimate tensile strength of SMC-25, SMC-30 and SMC-65 was examined. The impact resistance of SMC-25, SMC-30 and SMC-65 was measured using the instrumented Izod test method. Relative notch sensitivity factors for SMC-65, SMC-C20/R30 and XMC-3 were determined by measuring the effect of various size circular notches on ultimate tensile strength. Due to the large scatter in notched strength data for some of these materials, the statistics of strength for SMC-25 and SMC-65 are investigated. The behavior of single fastener bolted joints for SMC-25 and

SMC-65 is studied. Finally, ultrasonic inspection and scanning electron microscopy is used for flaw detection and investigation.

The first section of this report deals with the mechanical properties of these materials which were measured in this study. The second section gives a detailed explanation of test methods used to determine these properties. Finally, conclusions are drawn regarding the use of these materials in automotive applications.

2. COMPARATIVE MATERIAL PROPERTIES

2.1 Tensile Properties

In an attempt to determine the anisotropic elastic properties of the SMC composites with random fiber orientation, coupons were cut from the supplied material at orthogonal directions such that the loading direction would be parallel and transverse to the sides of the plate. Average values of Young's modulus, Poisson's ratio, tensile strength and tensile strain to failure for SMC-25 and SMC-65 (12 tests - 2 materials x 2 orientations x 3 replicates) are summarized in Table I. Obviously, the sheet molding compound materials are not isotropic since there is considerable difference in moduli and strength for the longitudinal and transverse specimens. The relative magnitudes of the moduli indicate a greater percentage of fibers oriented in the longitidinal direction. Consequently, the ultimate strength of the longitudinal specimens is considerably greater than the strength of the transverse specimens as shown in Table I.

The effect of volume fraction of glass fibers on the tensile properties is clearly shown in Table I. An increase from 25 to 65 percent by weight results in an 11-14% increase in modulus, a 138% increase in ultimate tensile strength and an 85% reduction in strain to failure. Typical stress-strain response for SMC-25 is shown in Figure 1.

To determine the tensile properties of the SMC C20/R30 system, samples were tested parallel and transverse to the surface fiber direction. Table II shows the average values of Young's modulus, Poisson's ratio, tensile strength and ultimate strain to failure for the SMC-C20/R30 (10 tests - 2 orientations x 5 replicates). The effect of the unidirectional surface plies in the SMC-C20/R30 can be seen by comparing the tensile properties to those of SMC-25. The ultimate strength in the longitudinal direction is more than tripled while the strength in the transverse direction is not greatly affected. The Young's modulus in the longitudinal direction is increased by nearly 50% with no significant change in the transverse Young's modulus.

The tensile properties of the XMC-3 composite were measured by cutting specimens in two directions. Longitudinal specimens were fabricated so that the fibers were oriented approximately $\pm 6°$ to the loading direction. Transverse specimens were cut so that the fibers were oriented approximately $\pm 84°$ to the loading direction. The average values of Young's modulus, Poisson's ratio, tensile strength and ultimate strain to failure for XMC-3 are also given in Table II (10 tests - 2 orientations x 5 replicates). The tensile results for the XMC-3 material show its

highly anisotropic nature. This composite is eight times stronger in the longitudinal direction than the transverse direction. The Young's modulus in the longitudinal direction is nearly three times greater than the Young's modulus in the transverse direction.

Typical failed specimens are shown in Figure 2. Note the brooming type failure for the longitudinal SMC-C20/R30 and XMC-3 materials. This type of failure is typical for highly aligned continuous fiber composites.

2.2 Compressive Properties

Compression specimens of the SMC composites were fabricated to give the same material property directions as the tensile specimens. Thus all materials were tested in two directions. The compressive properties (Young's modulus, Poisson's ratio, ultimate strength and strain to failure) for SMC-25 and SMC-65 are given in Table III (8 tests - 2 materials x 2 orientations x 2 replicates). Once again, the orthotropy of the material is evident. The moduli and strength of the longitudinal specimens were significantly greater than the values for the transverse specimens. The effect of volume fraction of glass fibers upon compressive properties was completely analogous to the trends observed for the tensile tests. Also note that the ultimate compressive strength and strain to failure are greater than the corresponding tensile values. A typical compressive stress-strain curve for the SMC-25 material is shown in Figure 3.

The compressive properties for SMC-C20/R30 and XMC-3 composites are given in Table IV (20 tests - 2 materials x 2

orientations x 5 replicates). Note that the ultimate compressive strength of the transverse specimen is much greater than the corresponding tensile strength while for the longitudinal specimens, the compressive and tensile strengths are virtually equivalent. Consequently, the compressive strain to failure for the transverse specimens is much greater than the tensile strain to failure. This behavior is typical of highly aligned fiber composites. The tensile and compressive Young's moduli for both the longitudinal and transverse specimens are virtually equal, as would be expected. Fractured specimens of SMC-C20/R30 and XMC-3 materials are shown in Figure 4.

2.3 Shear Properties

The shear properties of SMC-25, SMC-30, SMC-65, SMC-C20/R30 and XMC-3 were measured using the tension, two-rail shear test method. Shear test results for the SMC-25, SMC-30 and SMC-65 materials are presented in Table V (15 tests - 3 materials x 5 replicates). The SMC-65 material possesses both the greatest shear modulus and shear strength, followed by SMC-25 and SMC-30, respectively. Also note that the shear strain to failure is virtually of equal magnitude for these three random fiber molding compound materials. Typical shear stress-strain curves for SMC-25, SMC-30 and SMC-65 are shown in Figures 5, 6, and 7, respectively. Figure 8 shows typical fractured specimens of these materials.

The shear properties of SMC-C20/R30 and XMC-3 were measured at two temperatures: 23°C (73°F) and 93°C (200°F). The XMC-3 specimens were tested in two directions. The longitudinal

specimens have fibers oriented $\pm$6° to the shearing direction and the transverse specimens have fibers oriented $\pm$84° to the shearing direction. Due to the limited amount of SMC-C20/R30 available, this material was only tested in one direction. In these tests, the surface fibers were oriented parallel to the shearing direction. Typical fractured specimens are shown in Figure 9.

The results for the SMC-C20/R30 and XMC-3 are shown in Table VI. The effect of increasing the temperature from 23°C (73°F) to 93°C(200°F) was virtually the same for both SMC-C20/R30 and XMC-3. This temperature increase resulted in a 40-50% reduction in both the shear modulus and ultimate shear strength. The shear strain to failure, however, was not greatly reduced. It would be expected that the shear strength and shear modulus of the transverse XMC-3 specimens would be greater than that of the longitudinal specimens. This trend was verified but the difference was not appreciable.

It can be seen that the sheet molding compound with the largest shear strength and shear modulus is the SMC-65 material. The SMC-C20/R30 material has a greater shear strength than SMC-25 and SMC-30 but has a smaller shear modulus than SMC-25. As a result, the continuous surface fibers enhance the shear strength but do not greatly effect the shear modulus. The ultimate strain to failure is considerably greater for the continuous fiber systems than the random fiber systems.

2.4 Tensile Strain Rate Sensitivity

The influence of strain rate upon the tensile strength of SMC-25, SMC-30 and SMC-65 was examined. The results of the

strain rate study are summarized in Table VII. Results for SMC-25 are shown in Figure 10. These data indicate little or no sensitivity over the range 0.01 - 100 min^{-1}, but show a strengthening in the range 100 - 10,000 min^{-1}. The total energy absorbed versus strain rate is shown in Figure 11 for SMC-25. The data suggests a region of minimum energy absorption in the region 1 - 100 min^{-1}. Total energy absorbed is calculated from the force-time response of the specimen as the strain rate multiplied by the product of gage length and the impulse ($\int_T Fdt$).

The results for maximum stress for the SMC-30 material exhibits a near linear monotomic increase with increase in strain rate as shown in Figure 12. However, total energy absorbed decreases slightly in the region 10 - 100 min^{-1} before exhibiting an exponential increase from 100 - 10,000 min^{-1} (Figure 13).

Data presented for the SMC-65 exhibit a discontinuity in the region 1 - 10 min^{-1}. An increase in both maximum stress and energy absorbed is shown (Figures 14 and 15) from 0.01 to 1.0 min^{-1}. There is, however, an abrupt drop between 1.0 and 10 min^{-1}; followed by a monotomic increase between 10 and 10,000 min^{-1}. These results again suggest the existence of a region of minimum energy absorption in the range of 1 - 100 min^{-1}.

A typical fracture for each material is shown in Figure 16.

2.5 Impact Resistance

The instrumented Izod test method was employed to determine the impact resistance of SMC-25, SMC-30, SMC-65 and 5182-0 aluminum materials. The measured properties are defined in the section entitled Experimental Test Methods (pages 25-27).

Test results are summarized in Table VIII (32 tests - 4 materials x 8 replicates). The maximum load normalized by the cross sectional area at the notch is observed to increase in direct proportion to the fiber volume fraction while the initiation, propagation, as well as the total impact energies, vary inversely with fiber volume fraction. The initiation energy should be proportional to the fiber volume fraction and unnotched ultimate strength, but unfortunately the notch sensitivity also increases with volume fraction so that the initiation energy is actually reduced. The propagation energy is observed to decrease as the fiber weight fraction is increased from 25 to 65%. This reflects the importance of the matrix material in arresting crack growth. The SMC-25 material is the only material which possessed greater resistance to fracture than the 5182-0 aluminum. The total impact energy for the SMC-30 and SMC-65 were considerably less than the aluminum. The Sensitivity Index discussed previously was calculated using the aluminum as the reference material, σ_f = 207 MPa (30 Ksi). The SMC-25 and SMC-30 are found to be less notch sensitive than the aluminum while the SMC-65 is an order of magnitude more notch sensitive. Typical fractures are shown in Figure 17.

2.6 Notch Sensitivity

The experimental results of the notch sensitivity tests are used in conjunction with a strength model [6] to predict notch strength. The model assumes that failure occurs when the stress at some characteristic length from the edge of the hole, d_o, reaches the unnotched strength of the material, σ_o.

This characteristic length is assumed to be dependent upon two parameters, m and C, which are constant for a given material system, and the radius of the circular notch, R. This dependence is assumed to be of the form

$$d_o = \frac{(R/R_o)^m}{C} \tag{1}$$

where R_o is taken to be 1 in (2.54 cm) to nondimensionalize the quantity (R/R_o). Thus, the experimental results are used to determine the parameters m and C for each material system.

The stress distribution in an infinite orthotropic plate containing a circular hole is given by the approximate elasticity solution as

$$\frac{\sigma_{y(x)}}{\bar{\sigma}} = 1/2\{2 + (\frac{R}{x})^2 + 3(\frac{R}{x})^4 - (K_T^\infty - 3)[5(\frac{R}{x})^6 - 7(\frac{R}{x})^8]\} \tag{2}$$

where

$$K_T^\infty = 1 + \sqrt{2(\sqrt{\frac{E_y}{E_x}} - \nu_{xy}) + \frac{E_y}{G_{yx}}} \tag{3}$$

$\bar{\sigma}$ is the average stress in the plate and x is the distance from the center of the hole. Thus, by imposing the assumed failure condition, the notched tensile strength can be expressed as a function of notch radius.

$$\frac{\sigma_n}{\sigma_o} = 2\{2 + (\lambda)^2 + 3(\lambda)^4 - (K_T^\infty - 3)[5(\lambda)^6 - 7(\lambda)^8]\}^{-1} \tag{4}$$

where

$$\lambda = (1 + R^{m-1}R_o^{-m}C^{-1})^{-1} \tag{5}$$

The m and C parameters for a particular material are determined by fitting the experimental data to the strength prediction (4). The effect of varying the m and C parameters is shown in Figures 18 and 19.

It is possible to shift the notched strength relation (4) for a given material to a master curve for all materials. The magnitude of this shift gives a measure of relative notch sensitivity. The master curve is characterized by an arbitrary set of parameters, m* and C*. In order to superimpose the two curves

$$\lambda^* = \lambda \tag{6}$$

$$R^{*m^*-1} R_o^{-m^*} C^{*-1} = R^{m-1} R_o^{-m} C^{-1} \tag{7}$$

The generalized shift parameter, a_{cm}, can be defined such that

$$\log R^* = \log R + \log a_{cm} \tag{8}$$

The parameter a_{cm} can be determining from equation (7) and is given by

$$a_{cm} = \left(\frac{C^*}{C}\right)^{\left(\frac{1}{m^*-1}\right)} R_o^{\left(\frac{m^*-m}{m^*-1}\right)} R^{\left(\frac{m-m^*}{m^*-1}\right)} \tag{9}$$

The relative notch sensitivity is defined as

$$R_{ns} = \log_{10} R^* - \log_{10} R \tag{10}$$

and the reference system is chosen as $m^* = 0.0$, $C^* = 1.0$ in^{-1} and $R = .1$ in. Thus, it can be seen that

$$R_{ns} = \log_{10} a_{cm} = m + \log_{10} C \tag{11}$$

It should be noted that the relative notch sensitivity for two materials can be compared only if both systems possess the same K_T^{∞}.

Due to the large amount of scatter and the apparent insensitivity to notches up to 1.27 cm(.5 in) in diameter of the SMC-25 material (Table IX), this data was not fit to the model. This insensitivity implies that the effect of natural defects dominates the strength properties. For this reason, most of the failures for this material did not occur through the circular hole (Figure 20). As a result, the data for the SMC-25 material is analyzed in the section entitled, Statistical Strength Properties.

The notched strength of the SMC-65, SMC-C20/R30 and XMC-3 materials in plotted against log R in Figures 21, 22, and 23. The fractured specimens are shown in Figures 24, 25, and 26. The m and C parameters for each material were determined by fitting a curve to the data points. Table X gives the m and C parameters for each material as well as K_T^{∞} and the relative notch sensitivity, R_{ns}. The notch sensitivity curves for these materials are compared in Figure 27. It can be seen that the XMC-3 material is more sensitive to smaller holes. This fact is reflected in the larger value of the R_{ns} parameter for this material.

Examination of Figures 21, 22, and 23 reveals that the amound of scatter in the data seems to be a function of hole size. The standard deviation of the notch strength data is

plotted versus hole diameter in Figure 28, 29, 30, and 31 for the SMC-25, SMC-65, SMC-C20/R30 and XMC-3 materials. A decrease in scatter with hole size is observed for all materials except XMC-3.

It should be reported that many of the notch sensitivity specimens for the SMC-C20/R30 were fabricated from panel (C). As discussed in the Microscopic Examination section (p. 18), this panel was found to have an incorrect stacking sequence of the continuous and randomly oriented plies. Although it has been shown that the stacking sequence of laminated plates does affect notch sensitivity [7], the results from specimens fabricated from panel (C) seem to agree with results from specimens with the correct stacking sequence.

In summary, the notch sensitivity parameters enable the designer to predict notched strength as a function of notch radii for the material systems investigated. Furthermore, notch sensitivity has been shown to be a function of process conditions [6]. Consequently, variations in process conditions may appreciable affect the notch sensitivity parameters determined in this study.

2.7 Statistical Strength Properties

The notch sensitivity results for the SMC-25 and SMC-65 were also used to investigate the statistical strength characteristics of these materials. For the SMC-65 material, each five sample data set of notched and unnotched specimens was fit to a two parameter Weibull distribution which states that the probability of survival, P, at a stress level, σ, is given

by

$$P(\sigma) = \exp\left[-\left(\frac{\sigma}{\hat{\sigma}}\right)^{\alpha}\right] \tag{12}$$

where $\hat{\sigma}$ is a location parameter of the distribution, often referred to as the characteristic strength, and α is the shape parameter. The coefficient of variation for this distribution can be approximated by $1/\alpha$. Thus, the shape parameter is a direct measure of scatter. The larger α, the tighter the distribution.

Data were fit to equation (12) by taking double natural logs, with the result

$$\ln \hat{\sigma} + \frac{1}{\alpha} \ln\left[-\ln P(\sigma)\right] = \ln \sigma \ . \tag{13}$$

A linear regression analysis was used in conjunction with the data and equation (13). The inverse slope of the resulting straight line yields α and the y- intercept is the natural log of $\hat{\sigma}$. Another parameter, Π, is the coefficient of correlation.

Equation (12) was used in the form

$$P(\sigma_o) = \exp\left[-\left(\frac{\sigma_o}{\hat{\sigma}_o}\right)^{\alpha}\right] \tag{14}$$

for unnotched strength and in the form

$$P(\sigma_N) = \exp\left[-\left(\frac{\sigma_N}{\hat{\sigma}_N}\right)^{\alpha}\right] \tag{15}$$

for notched strength, where σ_o and σ_N are used to denote unnotched and notched strength, respectively.

An estimate of $\hat{\sigma}$ can be obtained from a small sample size, while a precise estimate of α requires a very large sample size. This difficulty can be overcome by considering Weibull's initial theory for the statistical failure of brittle materials. This theory implies that the shape parameter for unnotched specimens and specimens containing circular holes of various diameters under uniaxial tension should be identical. Using this premise, a data pooling scheme was used to combine all of the notched and unnotched data into one larger sample size of 40 to obtain an estimate of α. This procedure involves using the distribution

$$P(X) = \exp(-X^{\alpha}P), \quad 0 \leq X \leq 1. \tag{16}$$

where α_p is the pooled value of α and X is normalized parameter given by

$$X = \frac{\sigma_o}{\bar{\sigma}_o} \tag{17}$$

for unnotched strength and

$$X = \frac{\sigma_N}{\bar{\sigma}_N} \tag{18}$$

for notched strength. Thus each data set was normalized by its location parameter and the resulting data used to determine α_p in the same manner as for the separate data sets (See Table XI). If the pooling scheme is valid, the location parameter of the pooled distribution should be unity. Note that the pooled re-

sults for SMC-65 shown in the table yielded a location parameter, $\hat{\sigma}_p$, of 0.9987 and a good correlation coefficient of 0.9873 was also obtained. The data in the table also illustrates how much α varies for the various data sets. This is due to the small sample size of 5 contained in each data set. The pooled value of the shape parameter was 18.6 showing a reasonably tight distribution for tensile strength of SMC-65.

Since the data on the SMC-25 showed no clear sensitivity to circular holes, all of the data was pooled for statistical analysis without any normalization. Fitting the entire 40 sample set of data to a two parameter Weibull distribution yielded

$$\alpha = 5.89, \ \hat{\sigma} = 10{,}411 \text{ psi}, \ \Pi = 0.9829.$$

It would appear on the surface that almost complete notch insensitivity of the SMC-25 is a real plus for design considerations. This apparent notch insensitivity is most likely due to the large scatter in tensile strength, which indicates that the implanted holes have no more effect than the natural occurring flaws in the material. From a design standpoint, consider the consequences of the large scatter in the following example:

$$P(\sigma) = \exp\left[-\left(\frac{\sigma}{10{,}411}\right)^{5.89}\right]. \qquad (19)$$

For $P(\sigma) = 0.9$, $\sigma = 7{,}105$ psi. Thus, the design stress is only about 7 ksi for 90 percent survivability.

2.8 Bolted Joint Behavior

The bolted joint behavior of SMC-25 and SMC-65 was investigated in this study. The experimental test results are shown in Table XI, XII, XIII, and XIV (60 tests - 2 materials x 6 geometries x 5 replicates). Those data show the sample failure load and failure mode (net tension, shear-out or bearing). The results for the SMC-25 material are plotted in Figure 32. Typical failed specimens are shown in Figure 33. For specimens with a specimen width-to-hole diameter ratio (W/D) of 3.69, the failure load increases with an increase in the edge distance-to-hole diameter ratio (e/D). In addition, the failure mode changes from cleavage to net tension as e/D is increased from 1.85 to 5.54. For specimens of W/D = 7.38, failure at e/D = 1.85 is observed to be a combination of interlaminar and bearing failure. However, as e/D is increased, the failure mode changes to bearing and combined bearing and cleavage.

Test results for the SMC-65 materials are shown in Tables XIII and XIV. It is interesting to note that the primary failure mode for the SMC-65 material is net tension. This is due in part to the increased stiffness of the material. Test results shown in Figure 34 indicate that the material reaches an optimum strength near e/D = 3.69-5.54 for both specimen widths. The failure mode for e/D = 5.54 was primarily net tension although one specimen failed in bearing.

2.9 Nondestructive Test Results

The ultrasonic pulse echo technique was used to study the SMC-25 and SMC-65 materials. The scan of SMC-25 shown in Figure 35 shows a homogeneous mixture of random fibers. The

natural defect size in this material is between 1/2 and 1 3/4 inches implying that this material would be notch insensitive to holes below these diameters.

Natural delaminations were not found in the SMC-25, however; 0.013 inch diameter holes were drilled into the material from the end and through the thickness. Figure 37 shows C-scans comparing holes .010 inches in diameter in plexiglas with the .013 inch diameter holes in the SMC-25. The plexiglas was scanned in two ways. One method shows only the holes and the other method shows both the holes and the plexiglas. The SMC-25 was scanned to show both holes and SMC-25. The through the thickness holes in SMC-25 are difficult to see due to the natural defect size in the SMC-25 being on the same order as the hole diameter. During the drilling process the SMC-25 delaminated around one of the holes; this is shown clearly in the scan.

Volume fraction was determined for SMC-25 and SMC-65 by standard ashing and matrix digestion techniques. The average fraction of fibers by weight for SMC-65 was 63.82% fibers by weight with a standard deviation of .0733 and the fraction of fibers by weight for SMC-25 was 28.55% fibers by weight with a standard deviation of .0516.

In an attempt to determine fiber orientation of SMC-65, various focusing and gating techniques were investigated. The general trend of this study is shown in Figures 38, 39, & 40. A scan of SMC-65 with the gate set as close to the front surface as possible is shown in Figure 41. This scan also indicates much information about the surface texture of the SMC-65 material.

These scans, however, do not indicate much information on fiber orientation due to the fiber density and homogeneity of the material.

Figure 42 shows a C-scan of XMC-3 with the front of the gate set close to the front surface and the gate width containing the back surface. The $\pm$6° fiber orientation of this material is readily discernible in the scan.

In a further attempt to discern fiber orientation, dark field C-scan was employed. Transducer angles from 5 to 35 degrees were used. Figures 43, 44, and 45 show results of the 10, 20 and 30 degree scans. Some individual fibers can be seen in these scans, however the overall fiber orientation cannot be evaluated.

Figure 46 shows a scan of a disc of SMC-65 material with naturally occurring voids. Void diameters range from 1/16 inch to 1/4 inch. The material was sectioned and a photomicrograph taken of the void region; this is shown in Figure 47.

Artificial delaminations were introduced in a disc of SMC-65 material by centrally loading the disc and supporting the disc on its edges. Due to the attenuation of sound in SMC-65, even delaminations of this size are difficult to see when the delamination is on the under side of the materials, however Figure 48 shows a C-scan of the extent of the delamination on the front surface.

2.10 Microscopic Examination

Sections of SMC-25 and SMC-65 were made at 0 and 90 degrees to the samples longitudinal direction. A total of three sections

in each direction for each material were made. Representative photomicrographs of the 0 and 90 degree sections are shown in Figures 49 and 50 for SMC-65 and Figures 51 and 52 for SMC-25. The photomicrographs of SMC-65 show highly random fiber orientation while the photomicrographs of SMC-25 show less random orientation. The photomicrographs of SMC-25 also indicate a much higher void, matrix rich, content. In addition to the through the thickness sections, surface samples were polished and photographed. The surface of SMC-25 shown in Figure 53 shows a sparse population of fiber bundles with very little curvature. The surface of SMC-65 shown in Figure 54 indicates an interlocking structure, the fibers of which have a large amount of curvature.

Scanning electron micrographs of SMC-25 magnified 2750 times is shown in Figure 55 and a section of SMC-65 magnified 384 times is shown in Figure 56. The surfaces shown were machined with a diamond blade. Figure 56 shows the random fiber orientation and matrix rich regions in the SMC-65 material. The extent of damage caused by the diamond blade is also visible. Figure 55 shows a fiber bundle on the SMC-25 material.

Microscopic examination of the SMC-C20/R30 material revealed that while panels (A) and (B) have unidirectional surface plies and randomly oriented center plies, panel (C) possessed one unidirectional surface ply and one randomly oriented surface ply. The stacking sequence for this panel was [0/random/0/random] while the sequence for panels (A) and

and (B) was [0/random/random/0]. This can be seen in the photomicrographs shown in Figure 57.

3. EXPERIMENTAL TEST METHODS

3.1. Tension Test

The tensile test specimen used in this study was 228.5 mm (9.0 in) in length and 25.4 mm (1.0 in) in width. In order to avoid stress concentrations near the gripping region of this straight-sided specimen, beveled end tabs were adhesively bonded to the specimen. Thus, the test section length was 152.4 mm (6.0 in). The tensile test specimen is shown in Figure 58.

The tensile end tabs are fabricated from (.125 in) thick woven fiber glass circuit board material (EG-873 Phenolite). This material is first cut into strips approximately 508 mm (20 in) by 44.5 mm (1.75 in). These strips are then beveled by supporting them at an angle of 60 degrees and cutting an edge with an end mill. The resulting strip is 38.1 mm (1.5 in) wide with one beveled edge of 30 degrees. The strips are then cut into strips approximately 170 mm (6.7 in) long. The end tabs are bonded to a 229 mm (9 in) by approximately 127 mm (5 in) plate of the material to be tested by means of 3.2 mm (.125 in) diameter alignment pins and 6.4 mm (.25 in) diameter bolts. The end tab bonding fixture is shown in Figure 59. After the end tab material has been bonded to the plate, the tensile test specimens are cut to a width of 25.4 mm (1 in) with a 203 mm (8 in) diamond blade. The specimen width and thickness are then measured with a micrometer.

The tensile specimens were instrumented with longitudinal and transverse strain gages. Testing was performed in a static Instron testing machine (model TT-C) with a constant crosshead speed of .51 $^{mm}/_{min}$ (.02 $^{in}/_{min}$). The specimens were loaded to failure with strain recorded at load intervals with a Datran II Strain Indicator and Printer. This data is reduced to determine Young's modulus, Poisson's ratio, ultimate tensile strength and strain to failure.

3.2 Compression Test

A modified IITRI compression test fixture was used to determine the compressive properties of these materials (Figure 60). The overall specimen dimensions were 152.4 mm (6 in) long by 12.7 mm (.5 in) wide. The test section length was varied to insure against buckling. Thus the test section length was determined by considering specimen thickness, width, Young's modulus and ultimate strength. For the SMC-25 and SMC-65 materials, the test section length was 12.7 mm (.5 in) whereas the SMC-C20/R30 and XMC-3 test section length was 15.9 mm (.625 in). This length was varied by altering the dimensions of the end tabs. The compression test specimen is shown in Figure 61.

The compression test end tabs were fabricated from the same material as the tensile end tabs. Instead of being beveled, however, they are machined using the precision diamond saw to yield the desired dimensions. The end tabs are bonded to the specimen and then cut to the desired width in the same manner as the tension specimens. Figure 62 shows the compression end tab bonding fixture.

The compression test specimens were instrumented with a longitudinal strain gage on each side of the specimen. These gages were used to determine Young's modulus in compression and also to indicate the onset of specimen instability. The SMC-25 and SMC-65 materials were also instrumented with both longitudinal and transverse strain gages to determine Poisson's ratio. The modified IITRI compression test fixture was mounted on the crosshead of an Instron static testing machine (model TT-C) with a 5,000 kg compression load cell. The specimens were loaded to failure at a speed of .51 $^{mm}/_{min}$ (.02 $^{in}/_{min}$).

3.3 Shear Tests

Three shear test methods were investigated in this study. The test specimen geometries for the tension and compression two rail shear and the three rail shear test methods are shown in Figures 63, 64 and 65, respectively. Specimens are instrumented with strain gage rosettes in order that shear strain may be calculated. Schematics of the two rail tension and compression and three rail shear test specimens are shown in Figure 66 and 67. Specimens are inserted into the fixtures and held in place by 3.2 mm (.125 in) diameter pins. High strength fasteners are torqued to 52.9 N-m (475 in-lb) and the locating pins are then removed. Specimens are loaded to failure at a rate of .51 $^{mm}/min$ (.02 $^{in}/min$) in an Instron static test machine (model TT-C). Load-strain measurements are taken at regular intervals so that the shear stress-strain curve can be generated. Shear modulus is determined from a

least-squares fit of the data points which lie in the initial linear regime.

Typical shear stress-strain curves for SMC-25 material for the shear test methods are shown in Figure 5, 68 and 69. Average values of shear modulus, shear strength and shear strain to failure for SMC-25 are presented in Table XV for the three test methods considered (15 tests - 3 test methods x 5 replicates). Comparison of the test results indicates that the compression two rail shear test is judged adequate while yielding shear property data of the greatest magnitudes among the test methods. Although the properties obtained from the two rail tensile test were similar to those obtained by the three rail test, the three rail shear test was found to be inferior because it was an inherently more complicated test method and required a larger specimen size. Both the fixture and specimen geometry were more complex and the specimen alignment in the fixture was more critical. In addition, duplicate instrumentation may be required for the three rail shear test. Consequently, the largest amount of scatter in the data was observed for this test method and is reflected by the large standard deviation of shear modulus for the three rail test method (see Table XV). Therefore, the tension two rail shear test method was employed to characterize the shear response of the sheet molding compound composites.

Due to the expense associated with electrical resistance strain instrumentation, an extensometer was developed to determine the shear strain directly for the tension two rail shear

test specimen. The developed extensometer is shown in Figure 70. The device measures the relative extension of the adjacent probes located at the center of the extensometer. The shear strain is then determined by dividing the relative extension by the lateral distance between probes. To increase sensitivity, the output of the extensometer was amplified. Unfortunately, the absolute correlation of results with strain gage data is poor as shown in Figure 71. Also note that the initial slope of the extensometer shear stress-strain response is inaccurate due to the lack of sensitivity of the instrument or poor attachment of probes at low loads levels. However, Table XVI shows a correlation of shear modulus based upon the extensometer and strain gage data (see Figure 71) which indicates that the extensometer results are directly proportional to the actual shear modulus. Consequently, the instrument must be calibrated with respect to strain gage measurements to determine the proportionality constant. In all probability, this constant will vary with fixture and specimen geometry and possibly with material type. Therefore, caution must be exercised if this approach is to be extended to other materials and test conditions.

3.4 Tensile Strain Rate Sensitivity Test

In order to examine the tensile strain rate sensitivity of sheet molding compounds, dog bone tensile specimens were machined from panels of SMC-25, SMC-30 and SMC-65 in the longitudinal direction. Specimen dimensions are shown in Figure 72. Tests were performed in the servohydraulic high strain rate test

facility employing specially designed slip grips. The grip design allowed the actuator to establish a uniform velocity prior to engaging the specimen. Force and displacement were recorded as a function of time by means of a storage oscilloscope. Strain rate was taken as actuator velocity divided by the specimen test section length (50.8 mm, 2 in). Strain rate data was established for rates of 0.01, 1, 10, 100, 1000, and 10,000 min^{-1}.

3.5 Instrumental Izod Impact Test

The instrumented Izod test method was employed to determine the impact resistance of SMC-25, SMC-30, SMC-65 and 5182-0 aluminum materials. The notched specimen geometry is shown in Figure 73. The impact energy and the load-history for each specimen were measured. Typical load-histories for the materials under investigation are shown in Figure 74. The impact energy represents the resistance of a given specimen to fracture when subjected to a specific dynamic loading. However, the impact energy does not provide a complete description of the fracture behavior of the material. For example, a brittle high strength material may possess a large initiation energy, E_i, and a small propagation energy, E_p; while a low strength ductile material may possess a small E_i and a large E_p. Thus, even though the impact energy for two materials may be identical, their fracture behavior may be quite different. For unnotched specimens of similar geometries, the relative percentage of energy absorbed in fracture initiation and propagation provides a qualitative measure of the ductility of the material. Assuming the velocity of the impact striker is approximately constant during fracture,

the Ductility Index (DI) is defined simply as the ratio of the area under the load-time curve after maximum load (E_p) to the area under the curve prior to maximum load (E_i), as shown schematically in Figure 75. However, for notched specimens the initiation energy is greatly reduced by the stress concentration at the notch tip. Consequently the Ductility Index does not reflect the material ductility for notched test specimens.

The Ductility Index does enable the magnitudes of the initiation and propagation energies to be calculated from the total impact energy as follows:

$$E = E_i + E_p + E_i\ (1 + DI)$$

$$E_i = \frac{E}{1+DI},\quad E_p = E - E_i$$

The initiation energy is directly proportional to the square of the ultimate unnotched strength (σ_f) and inversely proportional to the Young's modulus. Therefore

$$E_i = \alpha\ \sigma_f^2/E$$

Where α is a function of specimen geometry. A notch sensitive material would be one in which the ratio of the theoretical to the actual initiation energy exceeds unity:

$$\frac{(\alpha\sigma_f^2/E)}{E_i} > 1$$

For notched specimens of similar geometry, we may define a Sensitivity Index (SI) with respect to a reference material as follows:

$$S.I. = \frac{\frac{\sigma_f^2}{EE}}{\left(\frac{\sigma_f^2}{EE_i}\right)_{reference}}$$

Values of S.I. greater than on imply qualitatively that the material is more notch sensitive than the reference material.

3.6 Notch Sensitivity Test

The notch sensitivity test specimen was fabricated in the same manner as a tensile test specimen with the exception that the overall specimen length was 305 mm (12.0 in) and the specimen width was 38.1 mm (1.5 in). The end tab geometry was the same as in the tensile test. The circular holes were machined into the specimens using a diamond core drill. The hole sizes for the SMC-25 and SMC-65 materials were 1.60 mm (0.63 in), 3.18 mm (.125 in), 4.78 mm (.188 in), 6.35 (.250 in), 7.94 mm (.313 in), 9.53 mm (.375 in), 12.7 mm (.5 in). Five unnotched specimens for each material were also tested. For the SMC-C20/R30 and XMC-3 specimens, the holes sizes were 3.18 mm (.125 in), 4.78 mm (.188 in), 6.35 mm (.250 in), 7.94 mm (.313 in), 9.53 mm (3.75 in), 11.1 mm (.438 in), 12.7 mm (.5 in) and unnotched. The ultimate strength of the SMC-25 and SMC-65 specimens was measured using friction grips in andInstron static testing machine (Model TT-C) with a crosshead speed .51 mm/min (.02 in/min). Since the strength of the SMC-C20/R30 and XMC-3

specimens exceeds the load capacity of the Instron load cell, these specimens were tested in a Tinius-Olson 120 KN static testing machine. It was not possible to directly control the strain rate but all tests were performed at approximately the same speed.

3.7 Bolted Joint Test [8]

The test coupon geometry shown in Figure 76 was fabricated for each bolted joint test. The test coupon geometry was 150 mm (6 in) in length. Load is introduced through beveled end tabs bonded to the laminate and reacted by a pin through the hole located approximately fifteen hole diameters from the tabs. This coupon configuration was designed to eliminate load history as a test variable and provide uniform load introduction without interaction with the joint area. Specimens were cut to widths of 19.1 mm (.75 in) and 38.1 mm (1.5 in) using a precision diamond saw. Holes were drilled using a diamond core drill and then reamed to 5.16 mm (.203 in) in diameter. Visual and ultrasonic inspection of the holes revealed negligible machining damage. The holes were centered with respect to the specimen width and located either 9.53 mm (.375 in), 19.1 mm (.75 in) or 28.6 mm (1.125 in) from the end of the coupon.

Standard Instron friction grips were used for load introduction at the tab end of the coupon while a special fixture was designed to simulate the bolted load reaction through the hole. The clevis fixture shown in Figure 77 was used to simulate the bolted joint conditions. For out-of-plane constraint the inserts shown in Figure 78 were used, where the washers were machined

to constrain a contact area of 64.5 mm^2 (.100 in^2) around the hole. In order to simply inhibit out-of-plane deformation while applying minimal frictional load transfer around the hole, the constraining washers were torqued finger tight. The tests were conducted with a crosshead speed of .51 mm/min (.02 in/min) and the load-displacement curve recorded for each test. Failure load was determined as the maximum load attained before the load drop accompanying failure of the joint.

The failed coupons were subjected to ultrasonic "C" scan inspection. This inspection revealed information about the size and nature of damage inflicted at failure. All coupons of the same material were scanned under identical conditions to allow valid comparison of the damaged areas. The typical scans are shown in Figure 79.

3.8 Nondestructive Ultrasonic Tests

C-scan is a method of NDE which employs ultrasonic waves to interrogate a material in an effort to determine anomalies in its structure. The primary uses of C-scan are:

(1) to determine fiber orientation in a composite material
(2) to detect voids or delaminations
(3) to detect changes in thickness
(4) to determine flow patterns in injection molded composites
(5) to detect "knit" lines in compression molded composites.

The C-scan itself is a 1:1 grayscale image of the material's internal structure. The grayscale is composed of ten discrete shades of gray and the image is composed of equally spaced lines of dots. The shade of the dot is determined by either the amplitude of the reflected ultrasonic wave or by the amplitude

of a given frequency component of the reflected wave.

Theory of Operation

A wide band pulse of short duration is emitted by the transducer. The wave reflected from the specimen is then received by the same transducer and enters the gating circuitry. The gating circuitry isolates a selected portion of the ultrasonic waveform for analysis (see Figure 80). The gated waveform can then be analyzed on a peak amplitude base or on a frequency base depending on the type of C-scan desired.

Peak Amplitude Base C-Scan

When a peak amplitude base C-scan is desired, the amplitude of the largest peak in the gated waveform is converted into a D.C. voltage. The polarity of the peak is user selectable. Therefore, the positive and negative halves of the wave may be investigated independently. The D.C. voltage is quantized into 10 regions ranging from 0 to 10 volts in 1 volt increments. Each region corresponds to a different shade of gray of the recorder with 10 corresponding to the darkest. A quantized D.C. voltage is then sent to current limiting circuitry which controls the output to the "hot pen." The voltage at the pen tip remains constant and the current is varied so that different amounts of oxide are burned off of the ink impregnated, oxide coated paper. The image is then formed by scan lines composed of dots whose shade of gray corresponds to the amplitude of the reflected wave at that point on the specimen (Figure 81).

Frequency Based C-Scan

When a frequency based C-scan is done the gated waveform is sent to either a spectrum analyzer or a digital computer. Here

the wave is analyzed using analog techniques or by incorporating a fast Fourier transform algorithm in the case of the digital computer. In either case the result is an amplitude spectrum based on the components of the waveform of each frequency. Due to the structure of the specimen, some frequencies will be enchanced while others are attenuated. A frequency to be monitored is chosen such that the amplitude of the frequency component changes as the structure of the material changes. The amplitude of this frequency component is then amplified such that its output falls in the 0 to 10 volt region of the quantizer. Processing then proceeds as before. It should be noted that the size of the smallest detectable structure is on the order of the wavelength of chosen frequency. Also, if too great a frequency is chosen, diffraction and Moiré patterns may develop.

Dark Field C-Scan

The waveform of a fiber near the front surface of a composite may be lost in the front surface echo. A method of isolating echos near the front surface is by inclining the transducer at an angle θ to the perpendicular of the sample (Figure 83). The reflected waveform is then analyzed using standard methods. A scan made in this way is called a dark field C-scan.

4. SUMMARY AND CONCLUSIONS

The mechanical property measurements performed in this study reveal much information of use to the designer of SMC components. It was found that for random fiber SMC composites

the tensile and compressive properties are anisotropic and an increase in volume fraction of fibers has a large effect on strength properties and a small effect on Young's modulus. The addition of unidirectional surface plies in the SMC-C20/R30 material resulted in considerable enhancement of strength and modulus properties in the surface fiber direction with little effect on the transverse properties. The XMC-3 composite was found to be highly anisotropic with a relatively high Young's modulus and strength in the longitudinal direction.

The material with the greatest shear strength and shear modulus of all the materials investigated is the SMC-65 material. The effect of increased temperature on the shear properties of SMC-C20/R30 and XMC-3 was determined. Surprisingly, the shear response of the XMC-3 material was virtually the same for both test directions.

The strain rate sensitivity test results show an increase in tensile strength with increased strain rate as well as a region of minimum energy absorption in the region 1-100 min^{-1}. The results of the impact resistance tests show that the initiation, propagation and total impact energies vary inversely with fiber volume fraction.

The notch sensitivity parameters were determined for three material systems. These parameters allow the prediction of notched strength as a function of hole diameter. The scatter in the notch sensitivity test data was also analyzed to predict the reliability of the SMC-25 and SMC-65 materials. The bolted joint behavior of two random fiber systems was also studied.

The ultrasonic C-scan techniques and microscopic examination revealed voids, matrix rich regions and fiber orientations of these materials.

In conclusion, the SMC-65 is a relatively high quality general purpose sheet molding compound. The SMC-C20/R30 and XMC-3 materials should be used in specialized applications where enhanced strength and modulus properties are required.

REFERENCES

1. Weibull, W., "A Statistical Theory of the Strength of Materials," Ingeniorsventenkapsakademiens Handlinger NR 151, pp. 5-45, 1939.

2. Whitney, J. M. and Nuismer, R. J., "Stress Fracture Criteria for Laminated Composites Containing Stress Concentrations," Journal of Composite Materials, Vol. 8, 1974, pp. 253-265.

3. Nuismer, R. J. and Whitney, J. M., "Uniaxial Failure of Composite Laminates Containing Stress Concentrations," Fracture Mechanics of Composites, ASTM STP 593, American Society for Testing and Materials, 1975, pp. 117-142.

4. Weil, N. A. and Daniel, J. M., "Analysis of Fracture Probabilities in Nonuniformly Stressed Brittle Materials," Journal of the American Ceramic Society, Vol. 47, June 1974, pp. 268-274.

5. Wolff, R. V. and Lemon, G. H., "Reliability Prediction for Composite Joints--Bonded and Bolted," Air Force Technical Report AFML-TR-197, May 1974.

6. Pipes, R. B., Wetherhold, R. C., and Gillespie, J. W., "A Superposition Method for the Notched Strength of Composite Materials," Journal of Composite Materials, Vol. 13, April 1979.

7. Pipes, R. B., Gillespie, J. W. and Wetherhold, R. C., "Superposition of the Notched Strength of Composite Laminates" in review Journal of Polymer Engineering and Science.

8. Wilson, D. W. and Pipes, R. B., "Behavior of Composite Bolted Joints at Elevated Temperature" Center for Composite Materials - CCM-1-78, May 1978.

TABLE I

Tensile Properties for SMC-25 and SMC-65*

Longitudinal	SMC-25	SMC-65
E_L^t GPa (Msi)	14.48 (2.1)	16.55 (2.4)
ν_{LT}^t	0.30	0.33
F_L^{tu} MPa (Ksi)	90 (13.1)	215 (31.2)
ε_L^{tu} (μ in/in)	11,400	1,500
Transverse		
E_T^t GPa (Msi)	12.41 (1.8)	13.79 (2.0)
ν_{TL}^t	0.30	0.23
F_T^{tu} MPa (Ksi)	68 (9.9)	163 (23.7)
ε_T^{tu} (μ in/in)	10,700	1,600

*Average based on 3 tests

TABLE II

Tensile Properties for SMC-C20/R30 and XMC-3*

Longitudinal	SMC-C20/R30	XMC-3
Young's Modulus GPa(Msi)	21.5 (3.12)	36.2 (5.25)
Poisson's Ratio	.300	.310
Ultimate Tensile Strength MPa(Ksi)	375.4 (54.44)	581.6 (84.35)
Ultimate Tensile Strain (μ in/in)	21211	17797
Transverse		
Young's Modulus GPa(Msi)	14.9 (2.16)	12.7 (1.84)
Poisson's Ratio	.183	.116
Ultimate Tensile Strength MPa(Ksi)	96.4 (13.98)	69.2 (10.03)
Ultimate Tensile Strain (μ in/in)	5658.4	5538

*Average based on 5 tests

TABLE III

Compressive Properties for

SMC-25 and SMC-65

Longitudinal	SMC-25	SMC-65
Young's Modulus GPa (Msi)*	12.41 (1.8)	23.44 (3.4)
Poisson's Ratio	0.28	0.44
Ultimate Compressive Strength MPA (Ksi)**	204 (29.6)	284 (41.2)
Ultimate Compressive Strain (μ in/in)*	20,600	12,700
Transverse		
Young's Modulus GPa (Msi)*	11.03 (1.6)	12.41 (1.8)
Poisson's Ratio	0.28	0.29
Ultimate Compressive Strength MPA (Ksi)**	162 (23.5)	223 (32.3)
Ultimate Compressive Strain (μ in/in)*	22,500	23,500

* Average values based on 2 tests

** Average based on 8 tests

TABLE IV

Compressive Properties for SMC-C20/R30 and XMC-3

Longitudinal	SMC-C20/R30	XMC-3
Young's Modulus GPa(Msi)	20.3 (2.94)	35.2 (5.10)
Ultimate Compressive Strength MPa(Ksi)*	407.1 (59.05)	577.9 (83.82)
Ultimate Compressive Strain (μ in/in)*	22,265	16,964
Transverse		
Young's Modulus GPa(Msi)**	11.9 (1.73)	14.3 (2.07)
Ultimate Compressive Strength MPa(Ksi)*	170.5 (24.73)	185.7 (26.93)
Ultimate Compressive Strain (μ in/in)**	18,731	17,853

* Average based on 5 tests

** Average based on 4 tests

TABLE V

Shear Properties of SMC-25, SMC-30 and SMC-65*

	G	τ^{us}	γ^{us}
	GPa (Msi)	MPa (Ksi)	(μ mm/mm)
SMC-25	4.48 (0.65)	79 (11.4)	28.000
SMC-30	2.69 (0.39)	65 (9.4)	31,500
SMC-65	5.38 (0.78)	128 (18.5)	30,000

*Average values based on 5 tests

Two rail tensile test

TABLE VI

Shear Properties of SMC-C20/R30 and XMC-3

	Shear Modulus GPa(Msi)	Ultimate Shear Strength MPa(Ksi)	Ultimate Shear Strain (μ mm/mm)
SMC-C20/R30			
23°C	4.09(.593)[a]	85.4(12.39)[a]	40,148[b]
93°C	2.28(.331)[a]	50.8(7.37)[a]	37,392[b]
XMC-3			
Longitudinal			
23°C	4.47(.649)[a]	91.2(13.22)[c]	44,496[c]
93°C	2.34(.339)[a]	55.4(8.04)[b]	39,509[b]
Transverse			
23°C	4.67(.678)[a]	95.5(13.85)[c]	49,773[d]
93°C	2.39(.346)[e]	59.8(8.67)[e]	42,790[e]

[a] Average based on 5 tests

[b] Average based on 4 tests

[c] Average based on 3 tests

[d] Average based on 2 tests

[e] Average based on 1 test

TABLE VII

Strain Rate Results*

Maximum Stress

MPa (Ksi)

Strain Rate ($min.^{-1}$)

Material	0.01	1	10	100	1000	10,000
SMC-25	73.8 (10.7)	73.8 (10.7)	67.6 (9.8)	78.6 (11.4)	109.6 (15.9)	109.6 (15.9)
SMC-30	45.5 (6.6)	49.6 (7.2)	67.6 (9.8)	66.9 (9.7)	80.0 (11.6)	87.6 (12.7)
SMC-65	202.7 (29.4)	244.1 (35.4)	165.5 (24.0)	222.0 (32.2)	236.5 (34.3)	287.5 (41.7)

Energy Absorbed

Cross Sectioned Area $\frac{J}{mm^2}$ $(\frac{in\text{-}lb}{in^2})$

SMC-25	0.10 (570)	0.12 (670)	0.05 (290)	0.08 (440)	0.14 (790)	0.30 (1700)
SMC-30	0.09 (510)	0.07 (400)	0.06 (330)	0.06 (360)	0.09 (520)	0.25 (1410)
SMC-65	0.35 (2000)	0.57 (3250)	0.25 (1450)	0.16 (890)	0.43 (2450)	0.49 (6520)

*Average based on 5 tests

TABLE VIII

Izod Impact Results*

	Cross Sectional Area mm^2 (in^2)	Maximum Load / Cross Sectional Area $\frac{Kg}{mm^2}$ ($\frac{lb}{in^2}$)	Energy Absorbed / Cross Sectional Area $\frac{J}{mm^2}$ ($\frac{in\text{-}lb}{in^2}$)			Propagation Energy / Initiation Energy	Sensitivity** Index
			Initiation Energy, E_i	Propagation Energy, E_p	Total Energy		
SMC-25	27.7 (0.043)	5.1 (7210)	0.037 (210)	0.123 (700)	0.160 (910)	3.3	0.65
SMC-30	24.5 (0.038)	5.8 (8210)	0.013 (76)	0.042 (237)	0.055 (313)	3.1	0.69
SMC-65	19.4 (0.030)	6.3 (9000)	0.006 (32)	0.028 (160)	0.034 (192)	5.0	28.28
5182-0 Al	22.6 (0.035)	- -	0.040 (226)	0.072 (408)	0.112 (634)	1.8	1.00

*Average based on 8 tests

**Sensitivity Index relative to 5182-0 Al
(Ultimate Strength ≈ 207 MPa (30 Ksi))

TABLE IX: SMC-25 NOTCHED STRENGTH DATA

SPECIMEN NO.	DESCRIPTION	ULTIMATE LOAD	AREA (IN^2)	σ ULT (PSI)	AVERAGE	$\frac{\sigma_H}{\sigma_o}$
29-6B	Unnotched	865	0.203	9,374		
29-5B	"	815	0.212	8,458		
29-5M	"	770	0.210	8,067	8,759	1.00
32-4B	"	715	0.180	8,739		
32-3B	"	820	0.197	9,157		
29-3T	0.0625"dia	560	0.200	6,160		
29-5T	"	690	0.212	7,160		
32-4T	"	1040	0.202	11,327	8,404	0.96
32-5T	"	1020	0.198	11,333		
32-7T	"	585	0.213	6,042		
32-1B	0.125" dia	920	0.202	10,020		
32-2T	"	940	0.198	10,444		
32-5M	"	1280	0.200	14,080	10,996	1.26
32-5B	"	1000	0.201	10,945		
32-7M	"	910	0.211	9,488		
32-2B	0.1875"dia	955	0.199	10,558		
32-2M	"	1090	0.199	12,050		
32-3T	"	860	0.192	9,854	11,265	1.29
32-6T	"	1280	0.204	13,804		
32-7B	"	960	0.210	10,057		
32-3M	0.250" dia	790	0.194	8,959		
32-6B	"	1170	0.209	12,316		
32-8B	"	1100	0.196	12,347	11,142	1.27
32-8M	"	790	0.192	9,052		
32-8T	"	1120	0.189	13,037		
29-2B	0.375" dia	700	0.195	7,897		
29-4B	"	1020	0.202	11,109		
29-6M	"	840	0.208	8,885	8,988	1.03
29-6T	"	800	0.208	8,462		
32-6M	"	800	0.205	8,585		
29-2M	0.3125"dia	670	0.194	7,598		
29-3M	"	860	0.199	9,508		
29-4M	"	910	0.201	9,960	9,562	1.09
29-4T	"	910	0.202	9,911		
32-1M	"	980	0.199	10,834		
29-1B	0.500" dia	660	0.192	7,562		
29-1M	"	665	0.186	7,866		
29-1T	"	560	0.183	6,732	8,155	0.93
29-2T	"	775	0.191	8,927		
29-3B	"	885	0.201	9,687		

TABLE X

NOTCH SENSITIVITY PROPERTIES

	m	C $in^{-1}(cm^{-1})$	K_T^{∞}	R_{ns}
SMC-65	.07	6.0(2.36)	3.15	.848
SMC-C20/R30	.17	5.1(2.01)	3.66	.878
XMC-3	.12	9.4(3.70)	4.29	1.093

TABLE XI

NOTCH SENSITIVITY TABULATED RESULTS--65% SMC

R(IN)	$\hat{\sigma}_N$(PSI)	$\hat{\sigma}_N/\hat{\sigma}_o$	α
0	24,971	1.00	9.37
0.03125	24,051	0.963	13.4
0.06250	25,376	1.02	9.90
0.09375	21,035	0.842	16.4
0.1250	18,778	0.752	21.9
0.15625	18,336	0.734	27.2
0.1875	18,050	0.723	15.8
0.2500	15,234	0.610	49.1

$\alpha_P = 18.6$, $\hat{\sigma}_P = 0.9987$,

$\pi = 0.9873$

TABLE XII:BOLTED JOINT TEST RESULTS--SMC-25

e/D	W/D	SAMPLE NO.	FAILURE MODE			LOAD (LBS)
			NET TENSION	BEARING	SHEAR	
1.85	3.69	30-1L-4T		✓	✓	551
		30-1L-5B			✓	511
		30-2L-1T			✓	489
		30-2L-2T			✓	820
		30-2L-3T			✓	866
3.69	3.69	30-1L-1B	✓			1085
		30-1L-2T	✓			1213
		30-1L-5T	Failed at Tab			750
		30-2L-2B	✓	✓		1124
		30-2L-3B				1153
5.54	3.69	30-1L-3T		✓		974
		30-1L-3B	✓	✓		1131
		30-1L-4B		✓		983
		30-2L-4B	✓			1047
		30-2L-5T	✓	✓		1010

TABLE XIII: BOLTED JOINT TEST RESULTS--SMC-25 (CONT'D)

e/D W/D	SAMPLE NO.	FAILURE MODE			LOAD (LBS)
		NET TENSION	BEARING	SHEAR	
1.85 7.38	30-3LBL		✓	*	745
	30-3LMR		✓	*	871
	30-3LML		✓	*	862
	30-3LBR		✓	✓	783
	30-3RTL		✓	*	765
3.69 7.38	30-1RML		✓	✓	1151
	30-1RTR		✓	✓	992
	30-3RTR		✓	✓	1074
	30-2RTR		✓	✓	1243
	30-1RMR		✓	✓	1140
5.54 7.38	30-2RMR		✓	✓	1303
	30-2RBL		✓	✓	1413
	30-2RBR		✓		1323
	30-3RML		✓		1168
	30-1RTL		✓	✓	1063

*Interlaminar

TABLE XIV: BOLTED JOINT TEST RESULTS--SMC-65

e/D	W/D	SAMPLE NO.	FAILURE MODE			LOAD (LBS)
			NET TENSION	BEARING	SHEAR	
1.85	3.69	65-17-1L	✓	✓		1318
		65-17-1R	✓	✓		1171
		65-72R	✓			1237
		65-17-4R	✓			1415
		65-74R	✓	✓		1321
3.69	3.69	65-17-2R	✓	✓		1411
		65-17-2L	✓			1468
		65-73L	✓			1351
		65-71R		✓		1151
		65-17-3L	✓	✓		1481
5.54	3.69	65-72L	✓	✓		1274
		65-74L	✓	✓		1389
		65-73R		✓		1151
		65-17-3R	✓			1459
		65-17-4L	✓			1325

TABLE XV: BOLTED JOINT TEST RESULTS--SMC-65 (CONT'D)

e/D	W/D	SAMPLE NO.	FAILURE MODE			LOAD (LBS)
			NET TENSION	BEARING	SHEAR	
1.85	7.38	65-21-BL		✓	✓	1279
		65-21-TR		✓		1131
		65-22-BR		✓	✓	1312
		65-22-BL		✓	✓	1243
		65-22-TL		✓		1250
3.69	7.38	65-21-TL			✓	1477
		65-22-ML			✓	1393
		65-11-BL			✓	1645
		65-12-TL			✓	1389
		65-12-BR			✓	1398
5.54	7.38	65-12-TR			✓	1431
		65-11-TR			✓	1495
		65-11-TL			✓	1651
		65-22-MR			✓	1276
		65-12-BL			✓	1504

TABLE XVI

Shear Properties for SMC-25*

Test Method	Shear Modulus G GPa (Msi)	Standard Deviation GPa (Msi)	Ultimate Strength τ^{us} MPa (Msi)	Ultimate Strain γ^{us} (μ mm/mm)
Compression Two Rail	53.80 (0.78)	3.65 (.053)	90	(13.0) 34,000
Tension Two Rail	44.80 (0.65)	3.10 (.045)	79	(11.4) 28,000
Three Rail	40.70 (0.59)	4.48 (.065)	80	(11.6) 32,000

*Average values based on 5 tests

TABLE XVII

Correlation of Extensometer

and Strain Gage Measurements

Shear Modulus GPa (Msi)

Test	Extensometer Shear Modulus	Strain Gage Shear Modulus	Calibration Constant
1	19.86 (2.88)	40.70 (0.59)	0.21
2	29.58 (4.29)	49.00 (0.71)	0.17
3	32.68 (4.74)	49.60 (0.72)	0.15
Average	27.37 (3.97)	46.90 (0.68)	0.18

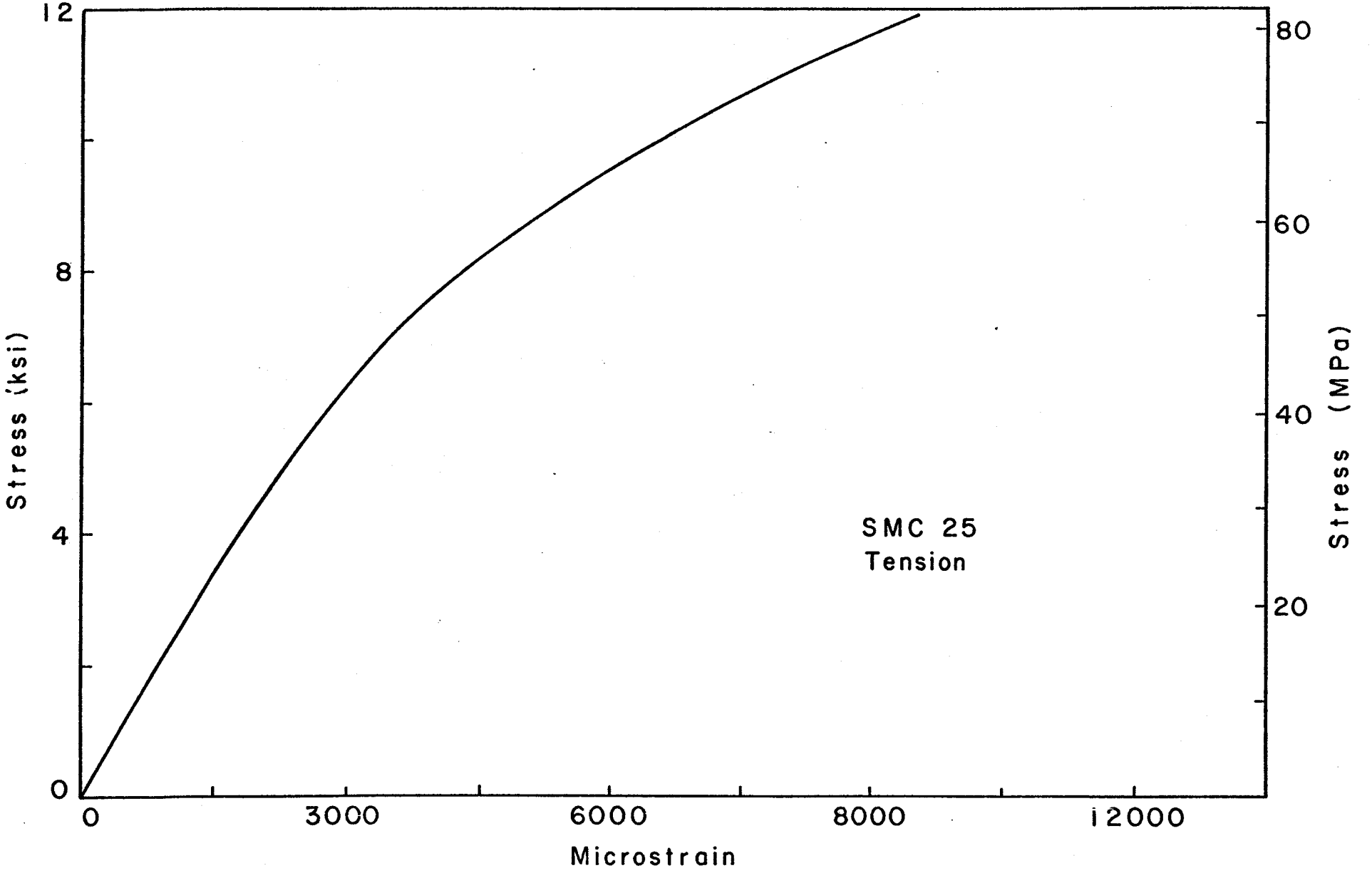

FIGURE 1. SMC-25 TENSILE STRESS-STRAIN RESULTS

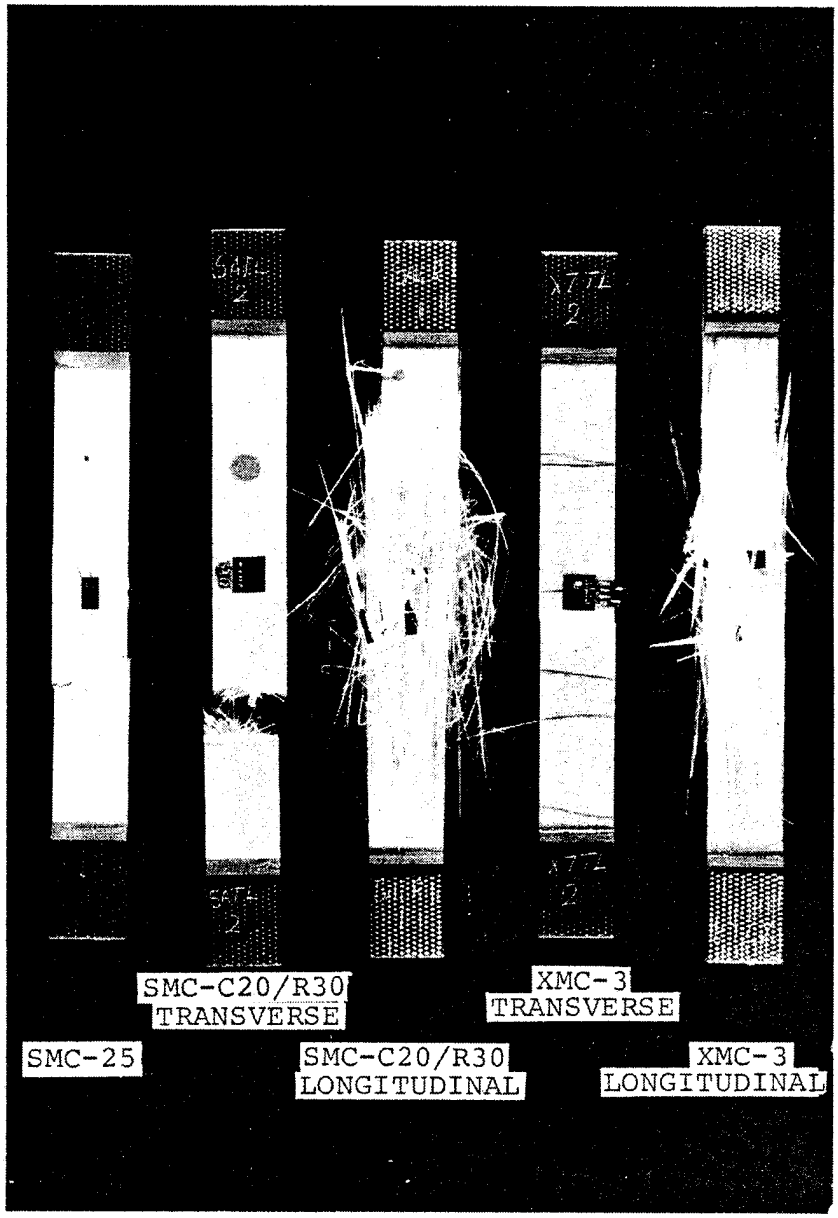

FIGURE 2. FRACTURED TENSILE SPECIMENS

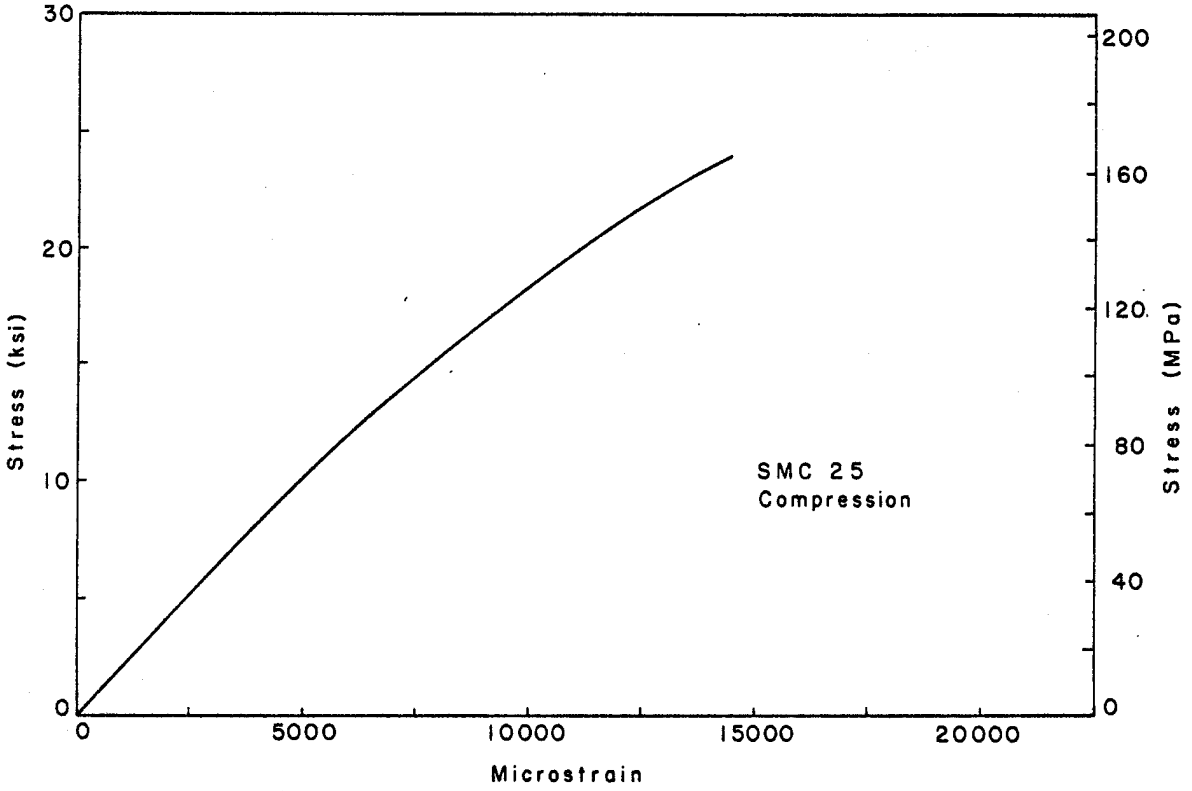

FIGURE 3. SMC-25 COMPRESSIVE STRESS-STRAIN RESULTS

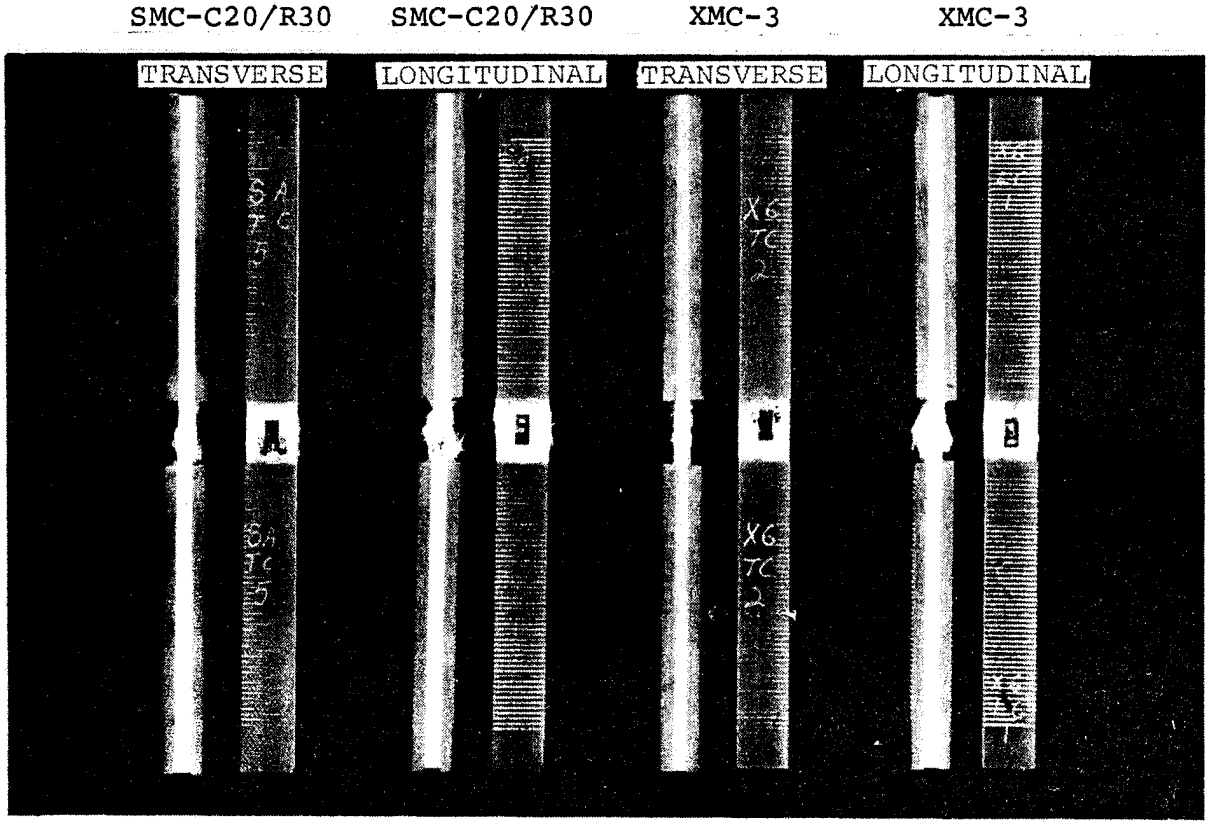

FIGURE 4. FRACTURED COMPRESSIVE SPECIMENS

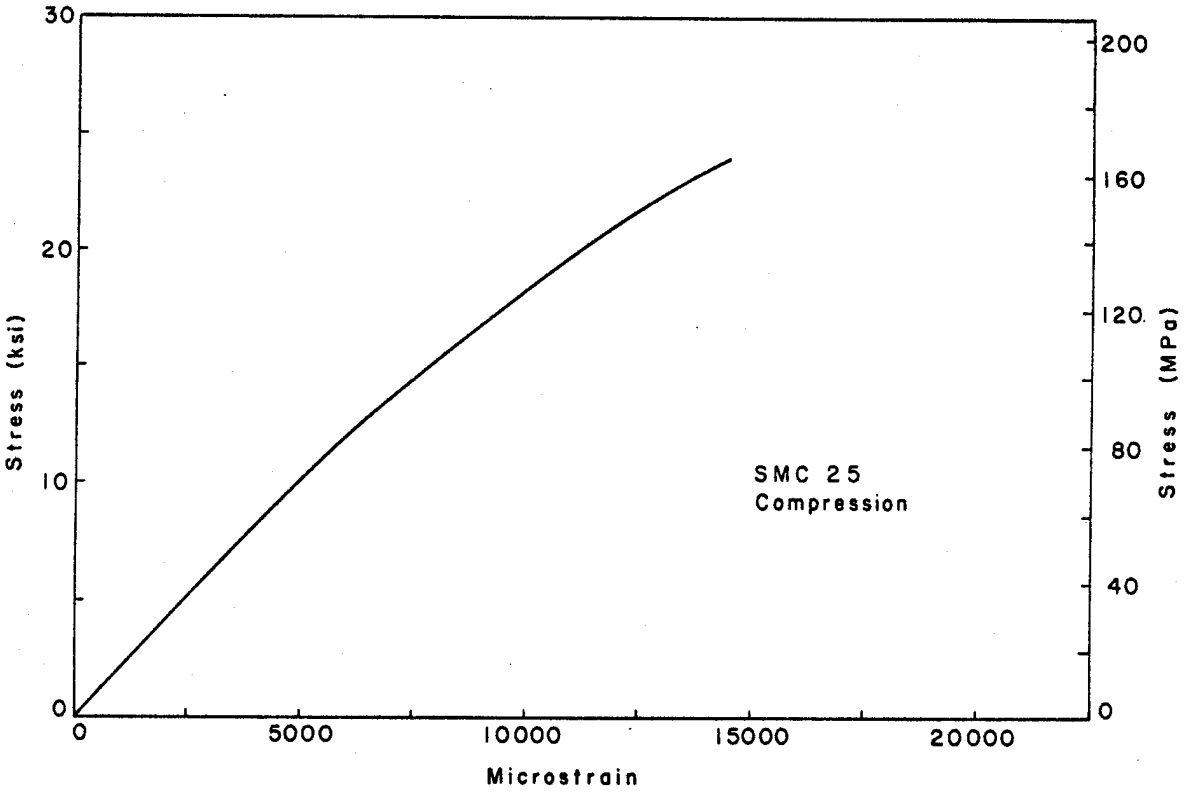

FIGURE 3. SMC-25 COMPRESSIVE STRESS-STRAIN RESULTS

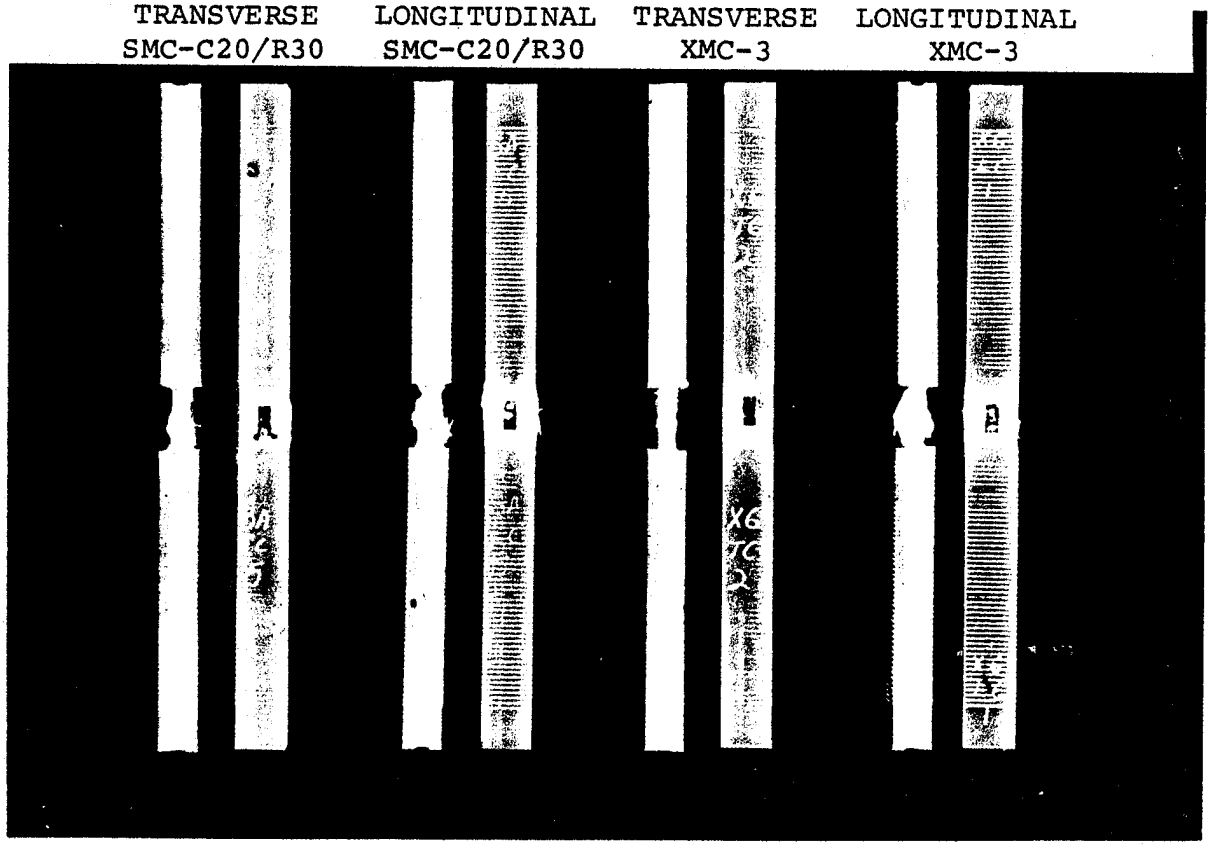

FIGURE 4. FRACTURED COMPRESSIVE SPECIMENS

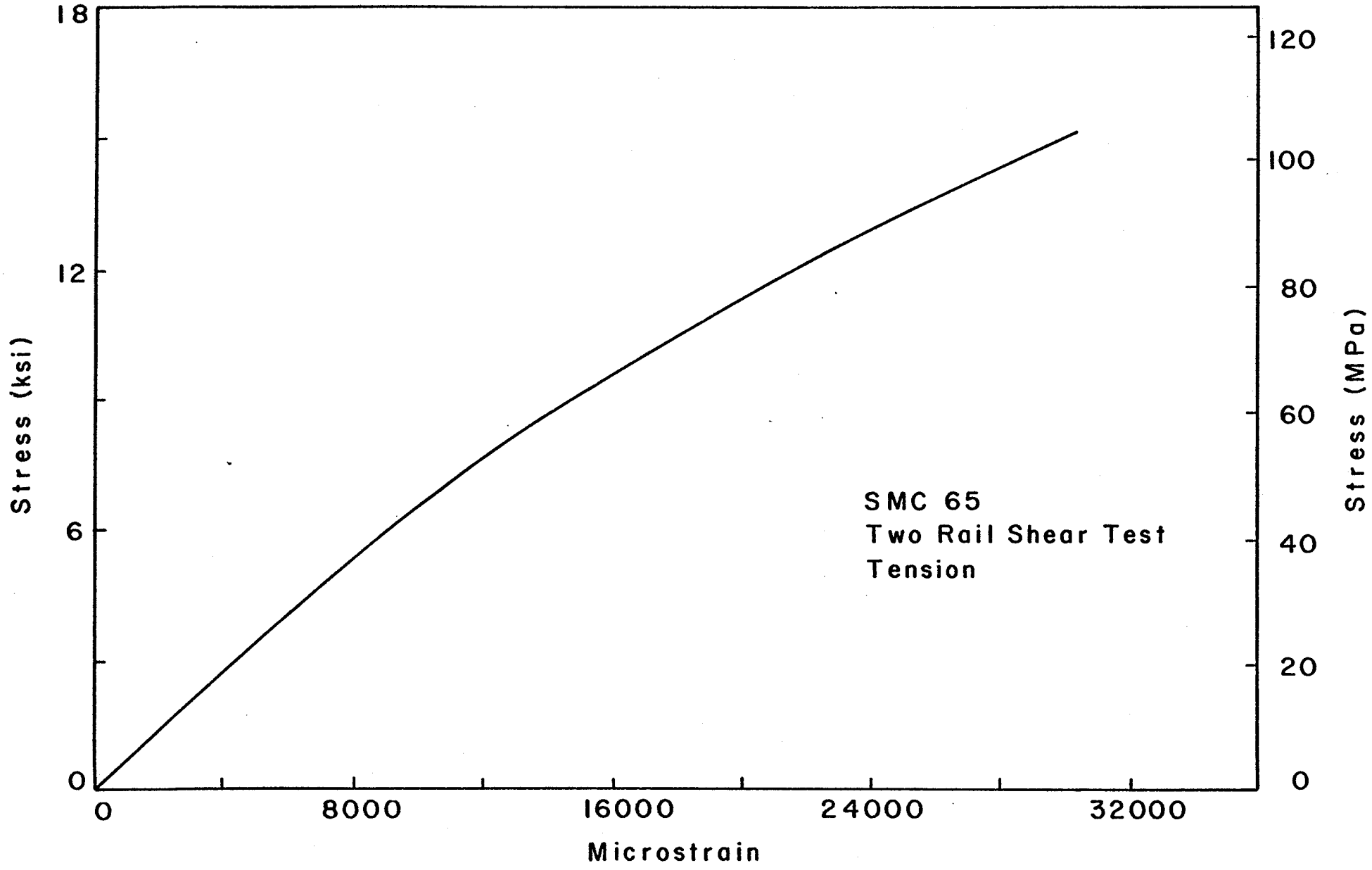

FIGURE 7. SHEAR STRESS-STRAIN RESULTS - TWO RAIL TENSILE SMC-65

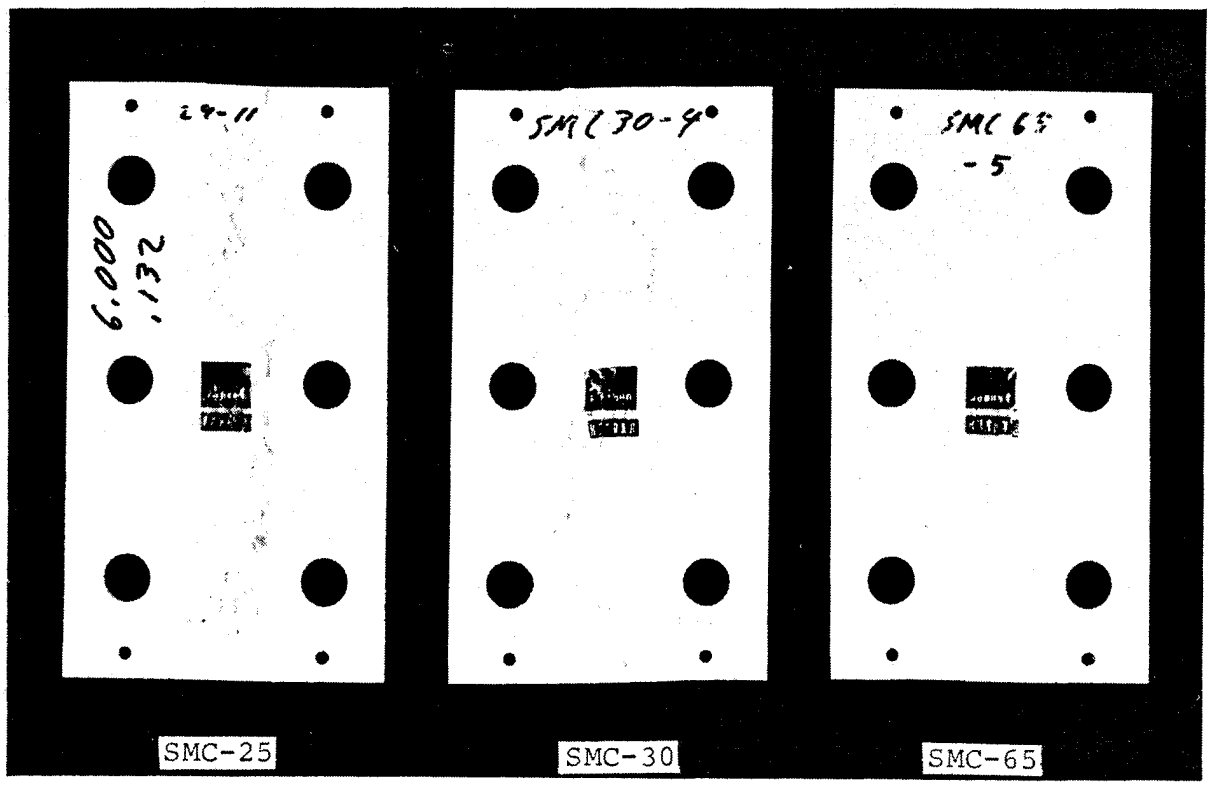

FIGURE 8. FRACTURED RAIL SHEAR SPECIMENS - SMC-25, SMC-30, SMC-65

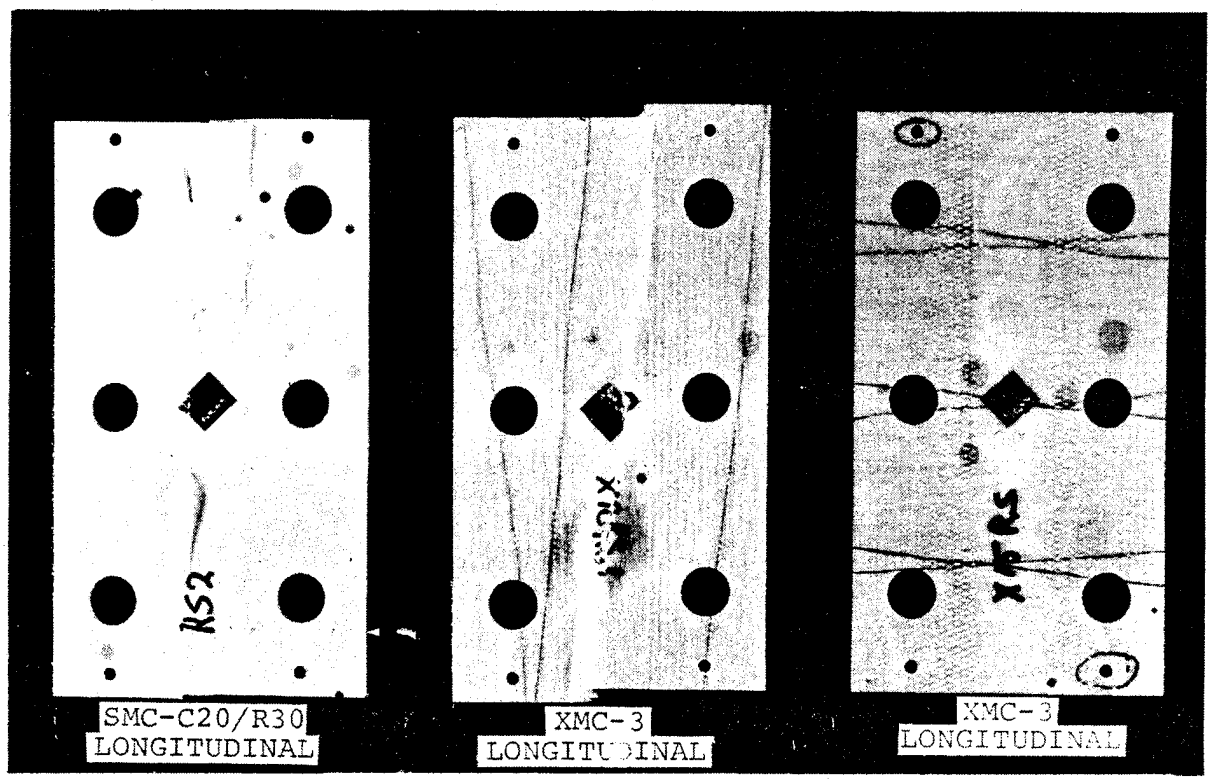

FIGURE 9. FRACTURED RAIL SHEAR SPECIMENS - SMC-C20/R30. XMC-3

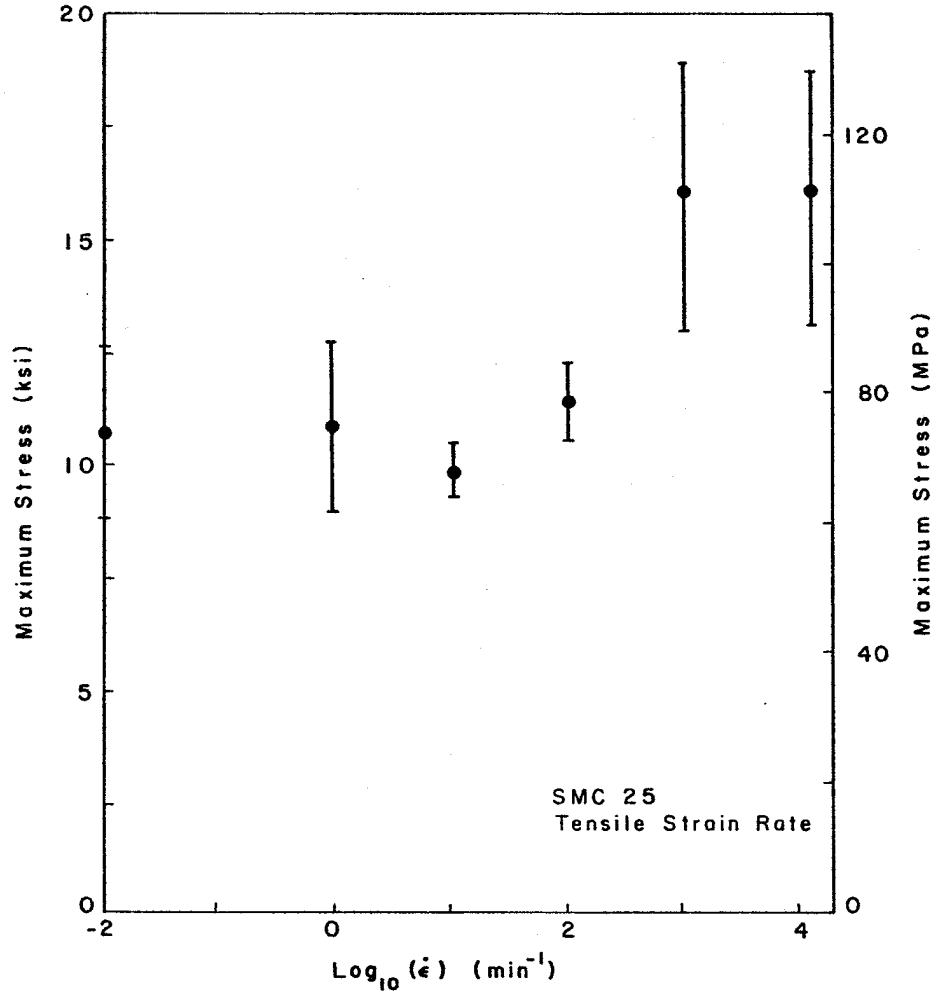

FIGURE 10. SMC-25 STRAIN RATE RESULTS - MAXIMUM STRESS

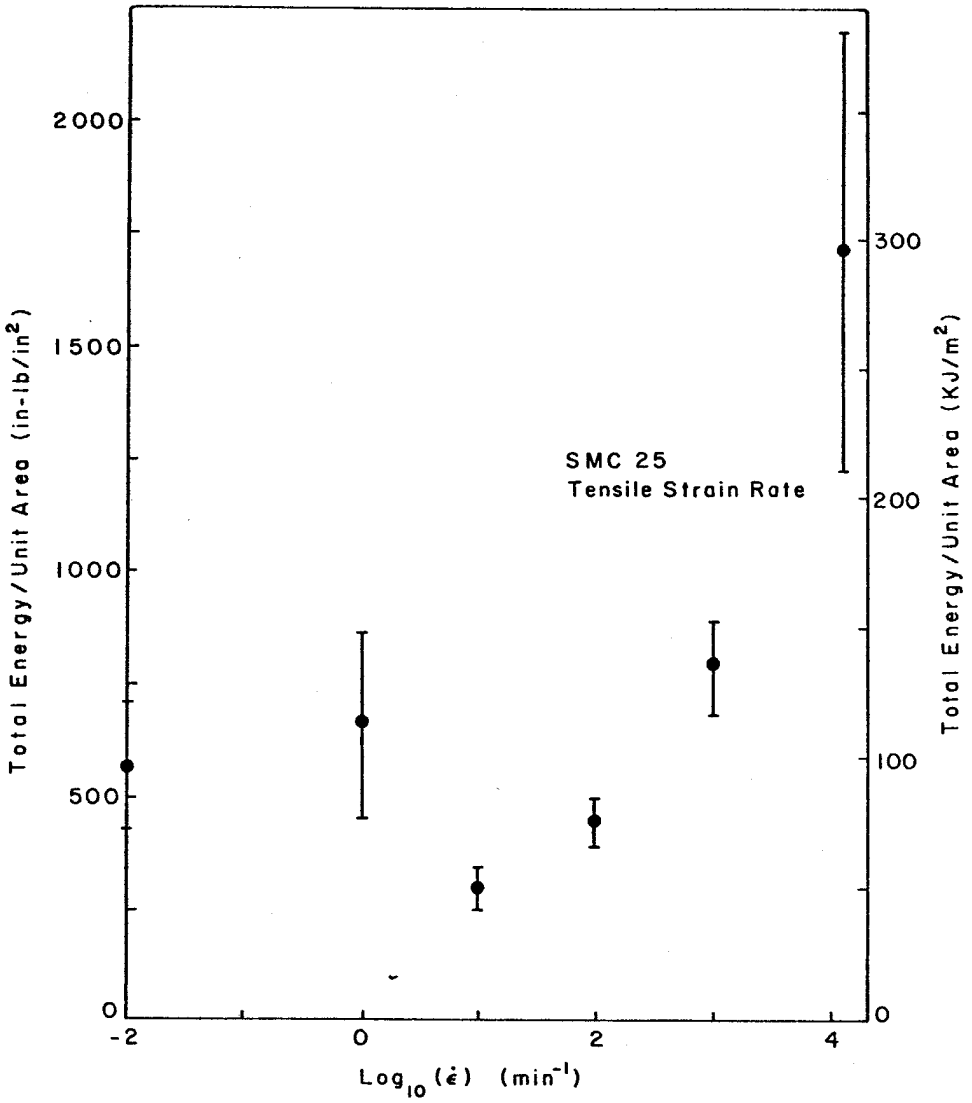

FIGURE 11. SMC-25 STRAIN RATE RESULTS - ENERGY

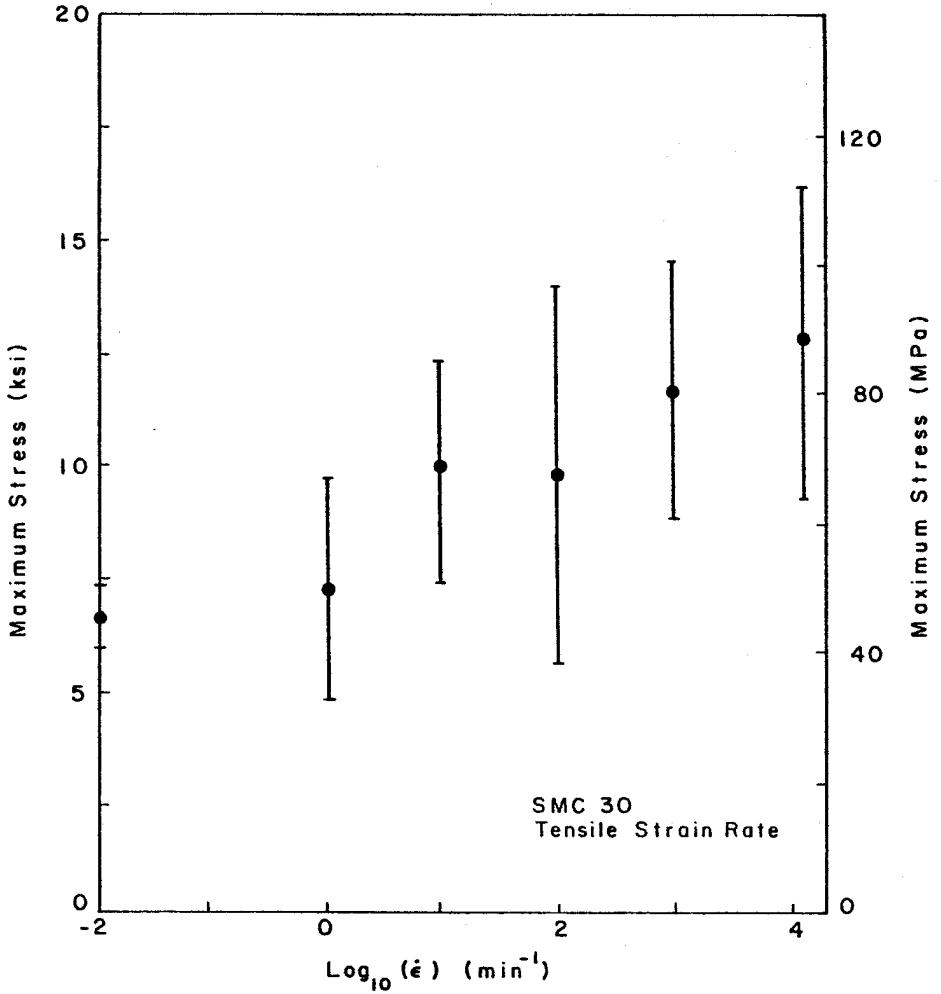

FIGURE 12. SMC-30 STRAIN RATE RESULTS - MAXIMUM STRESS

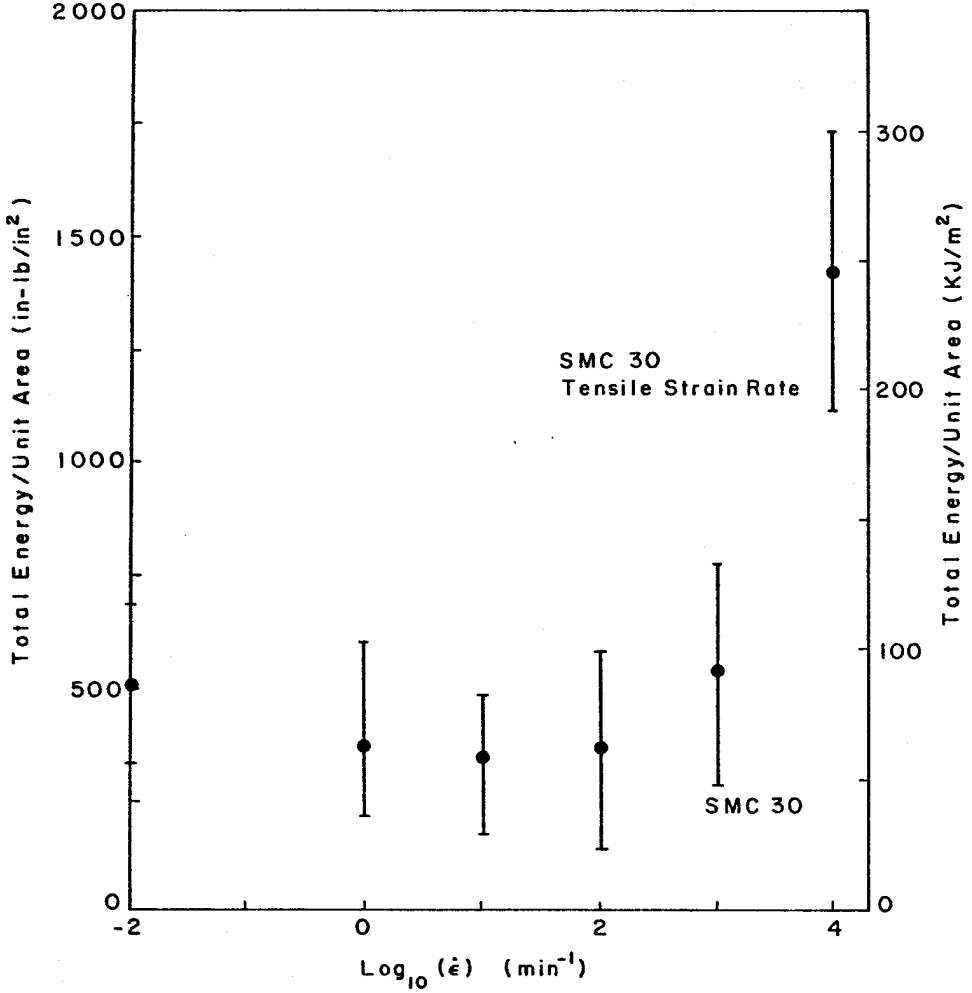

FIGURE 13. SMC-30 STRAIN RATE RESULTS - ENERGY

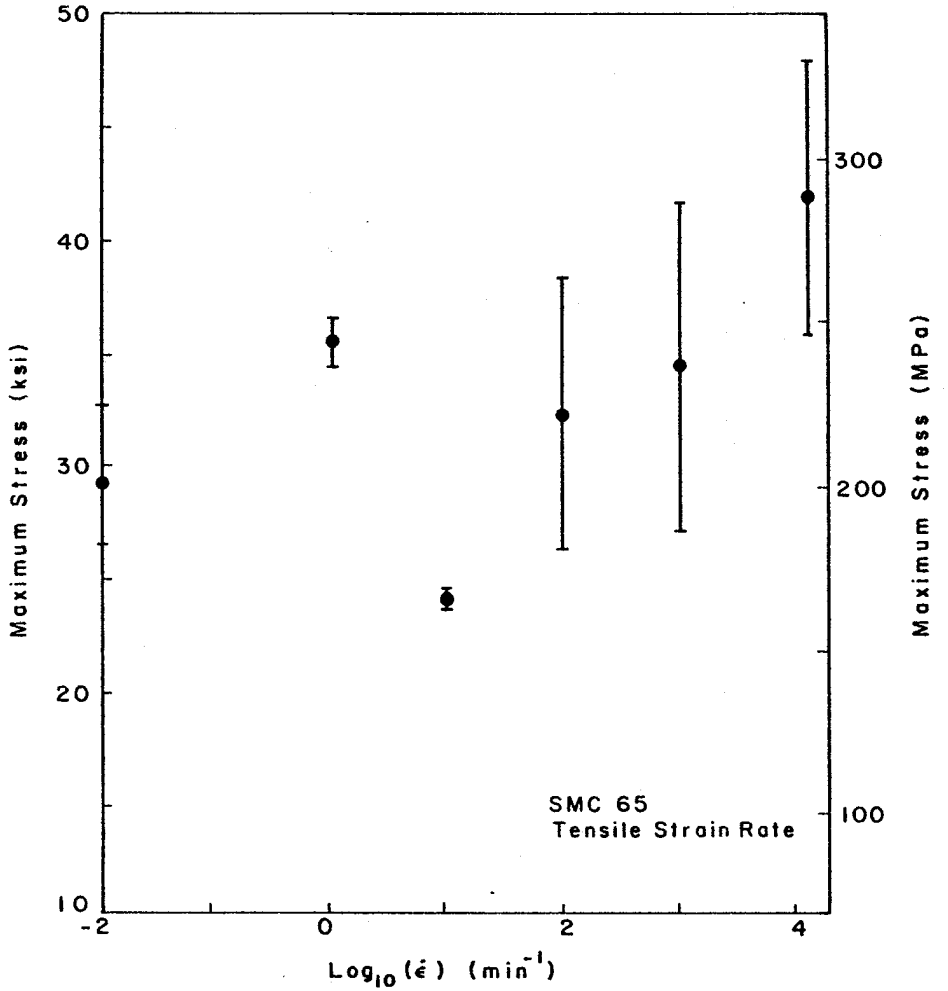

FIGURE 14. SMC-65 STRAIN RATE RESULTS - MAXIMUM STRESS

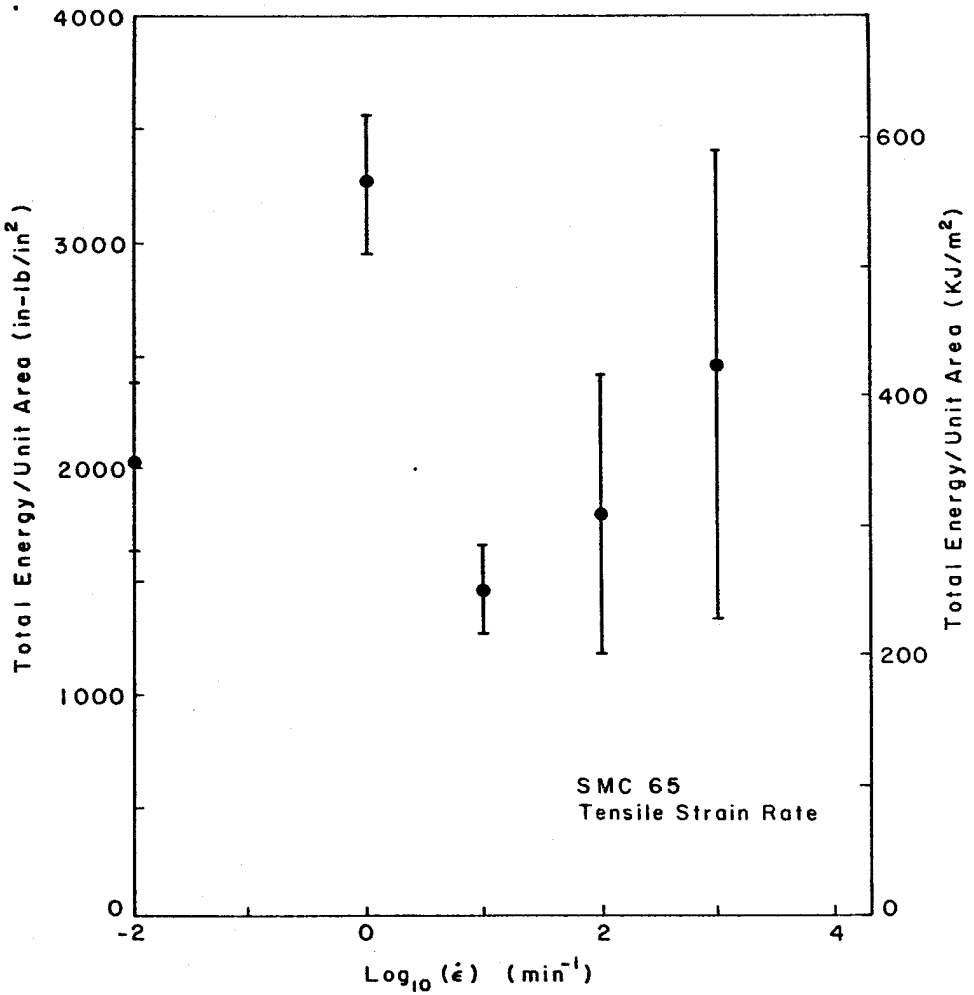

FIGURE 15. SMC-65 STRAIN RATE RESULTS - ENERGY

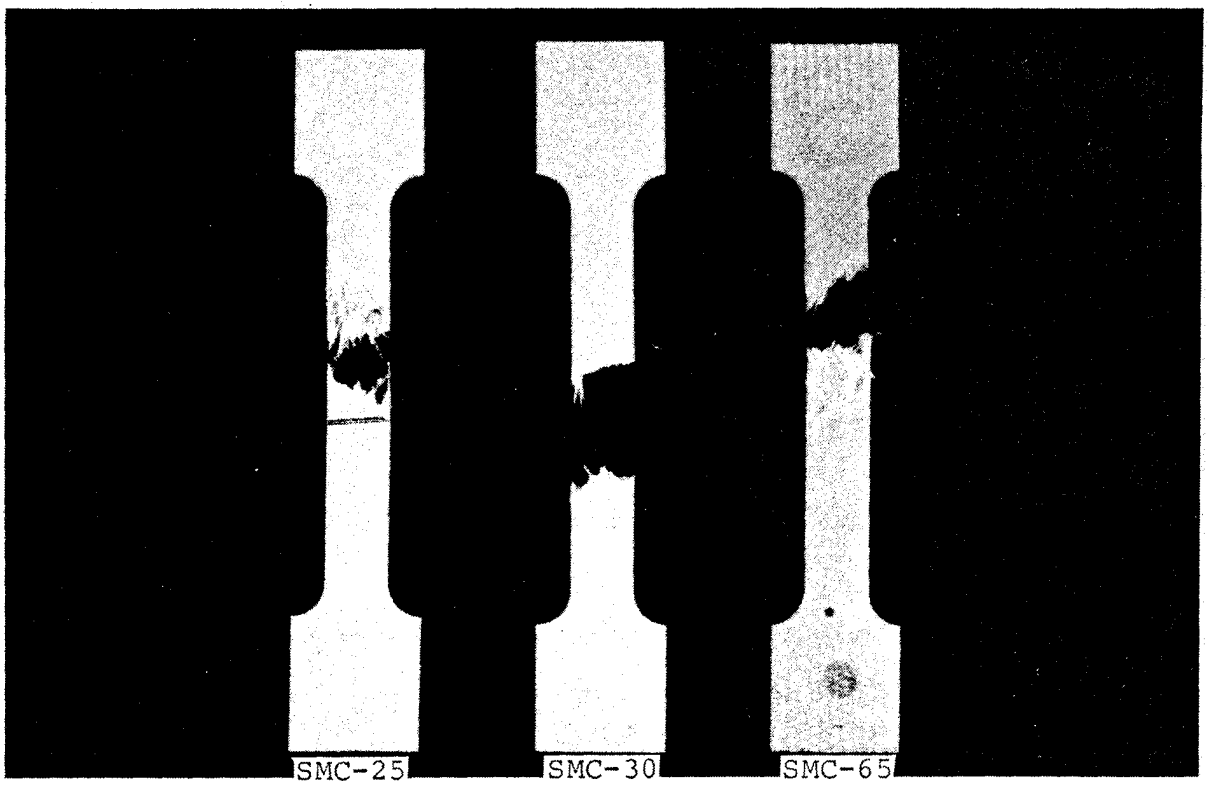

FIGURE 16. FRACTURED STRAIN RATE SPECIMENS

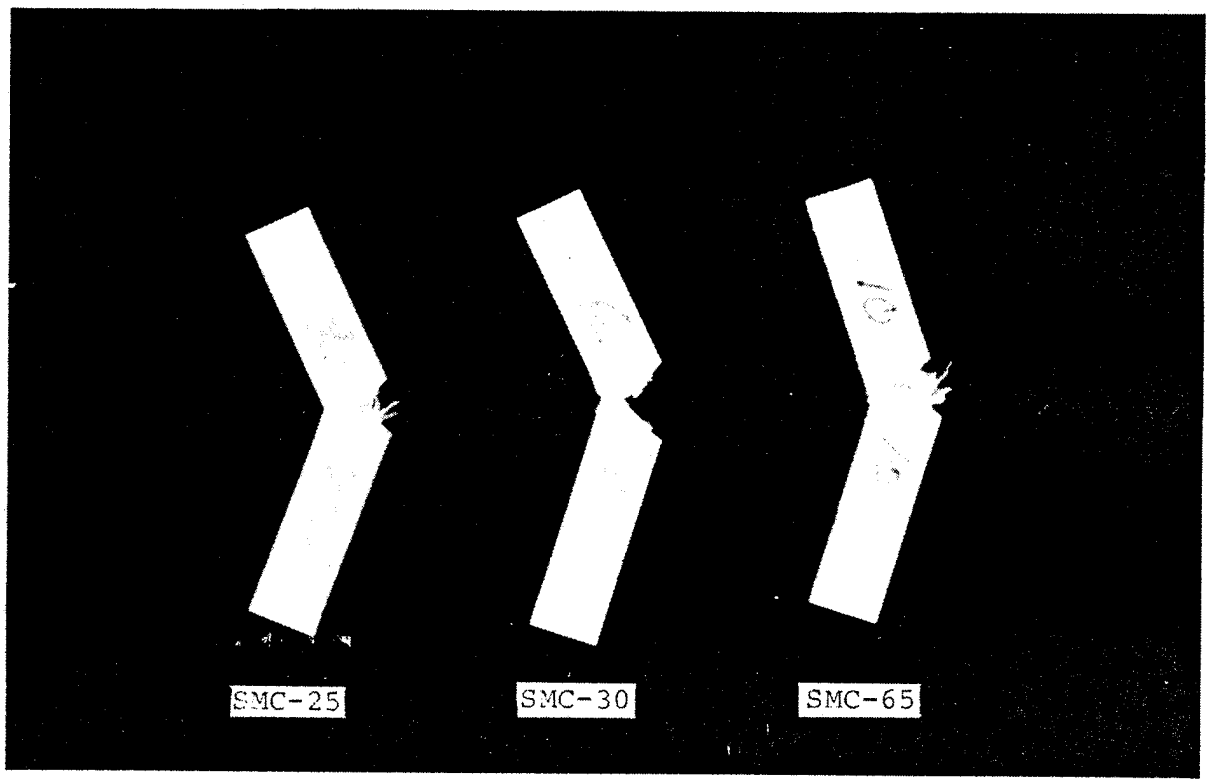

FIGURE 17. FRACTURED IZOD IMPACT SPECIMENS

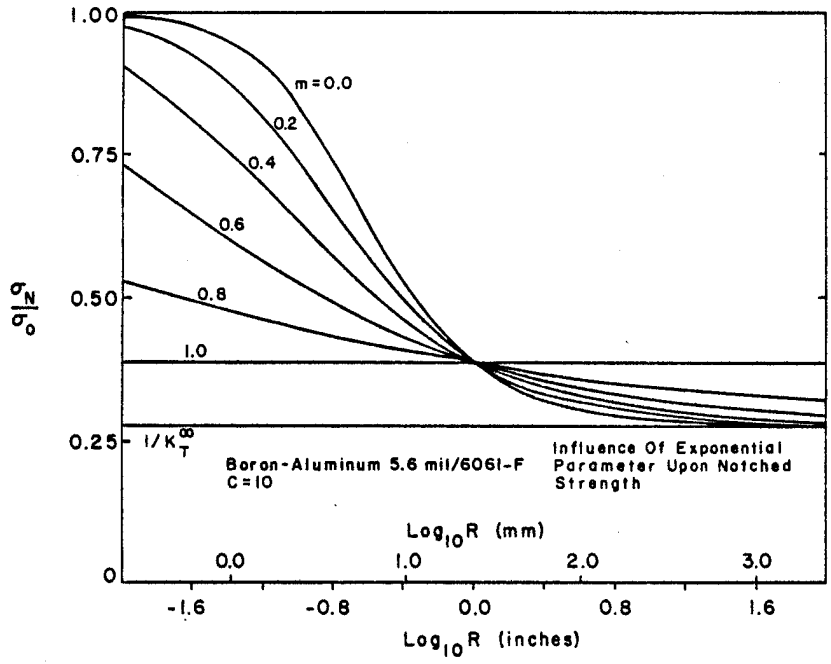

FIGURE 18. EFFECT OF VARYING m ON NOTCH SENSITIVITY

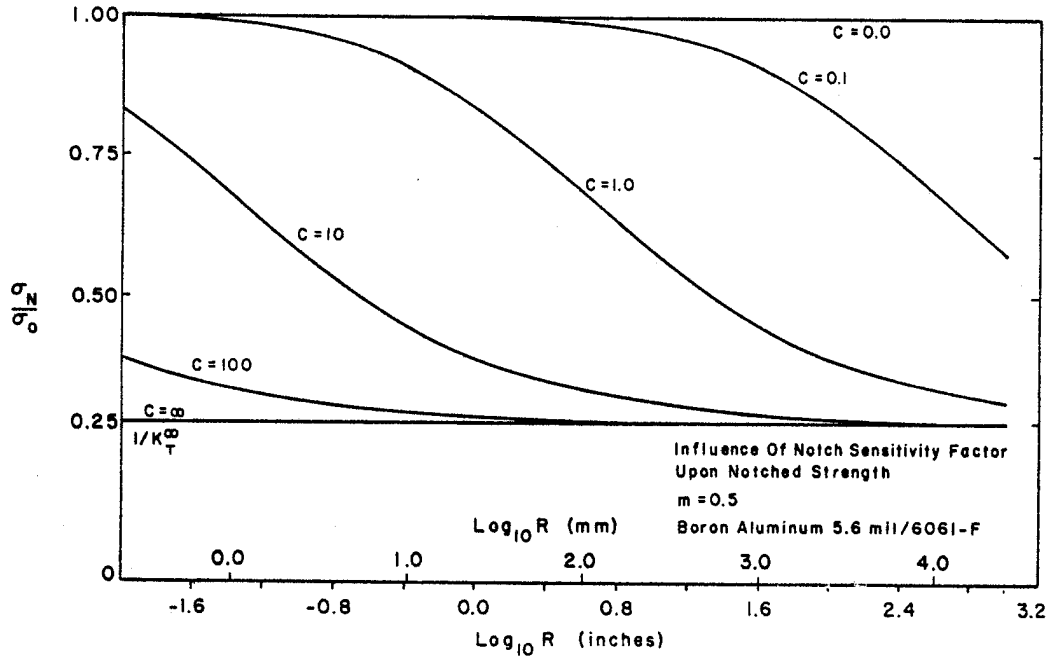

FIGURE 19. EFFECT OF VARYING C ON NOTCH SENSITIVITY

FIGURE 20. SMC-25 FRACTURED NOTCH SENSITIVITY SPECIMENS

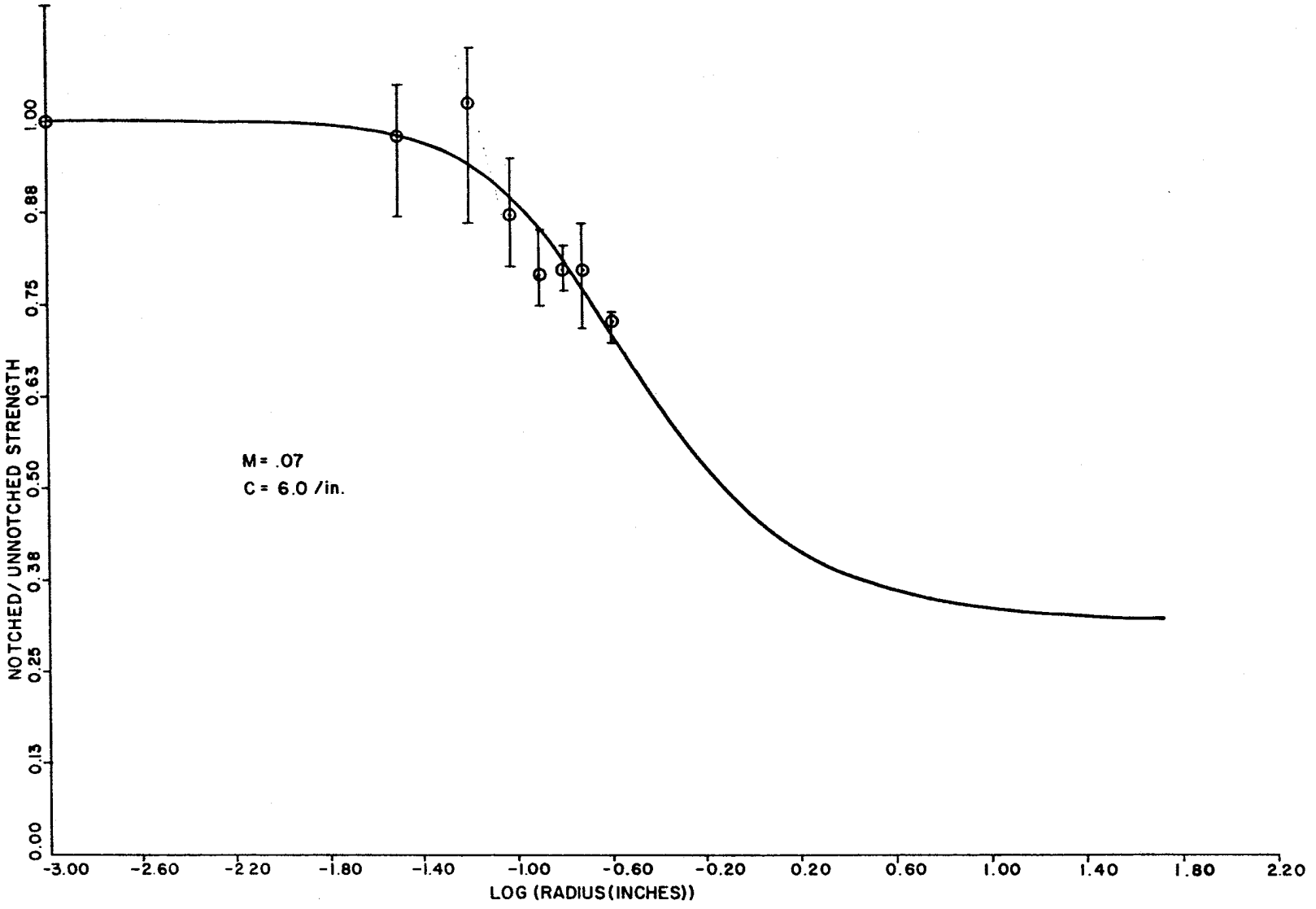

FIGURE 21. NOTCH SENSITIVITY OF SMC-65

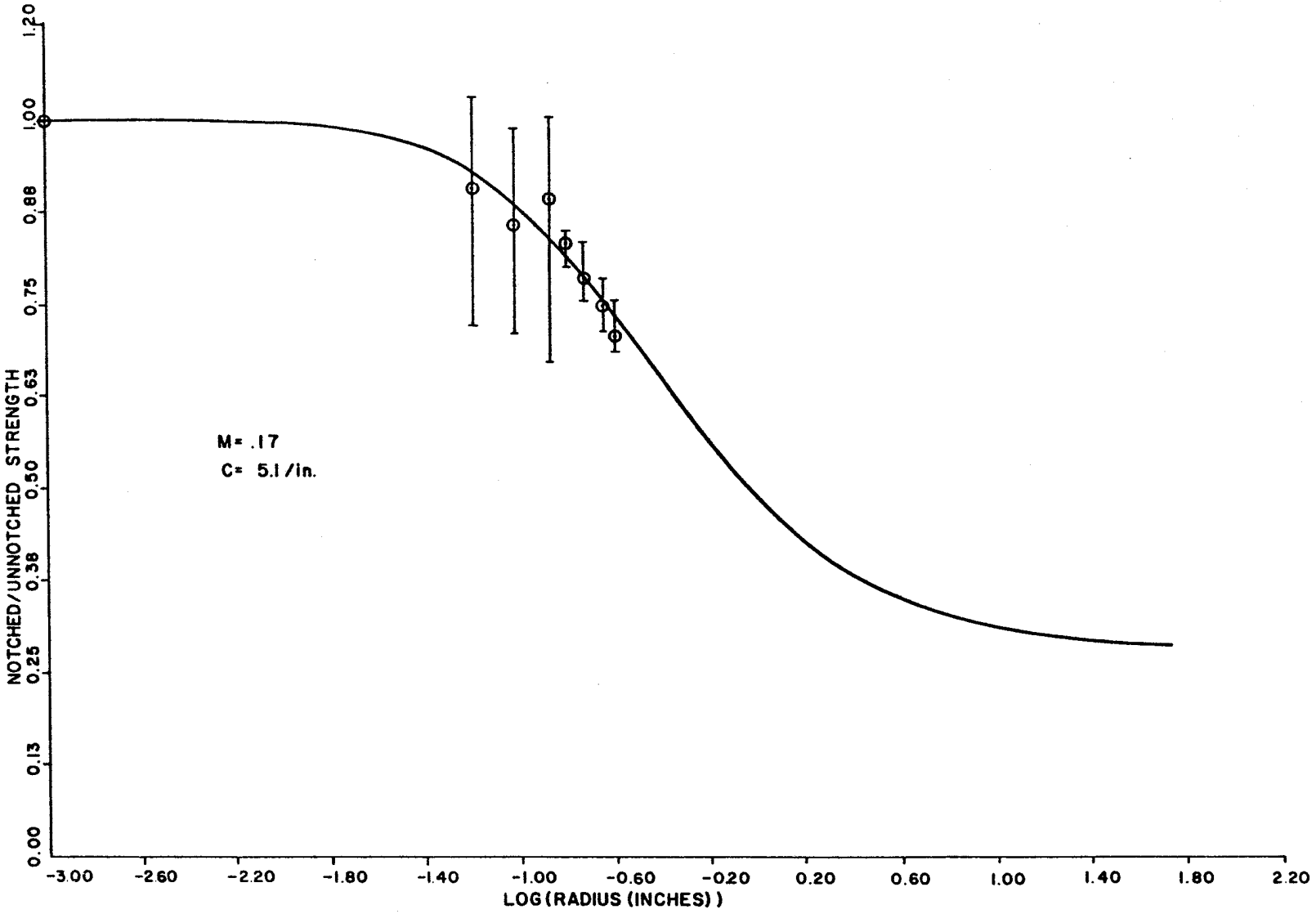

FIGURE 22. NOTCH SENSITIVITY OF SMC-C20/R30

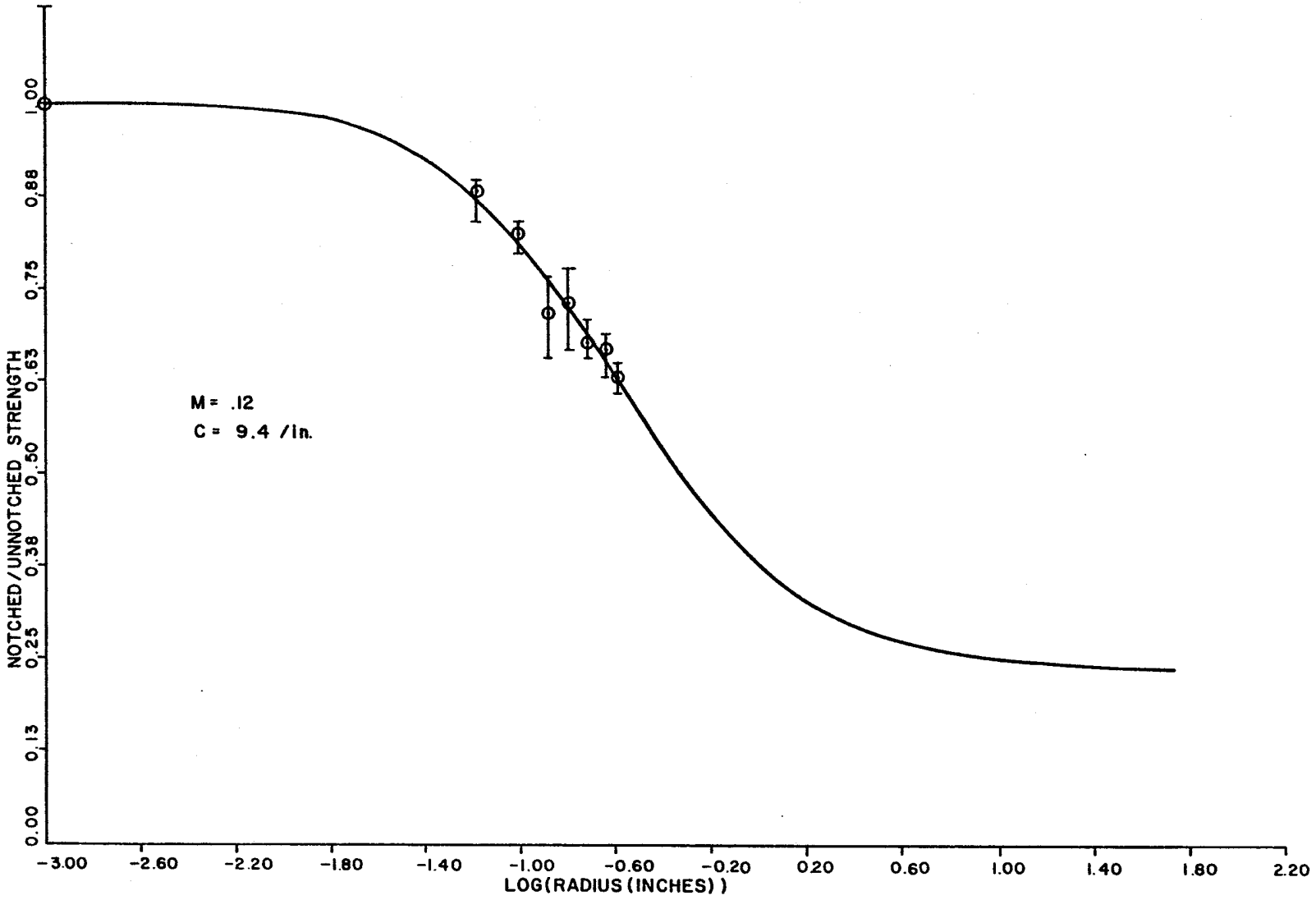

FIGURE 23. NOTCH SENSITIVITY OF XMC-3

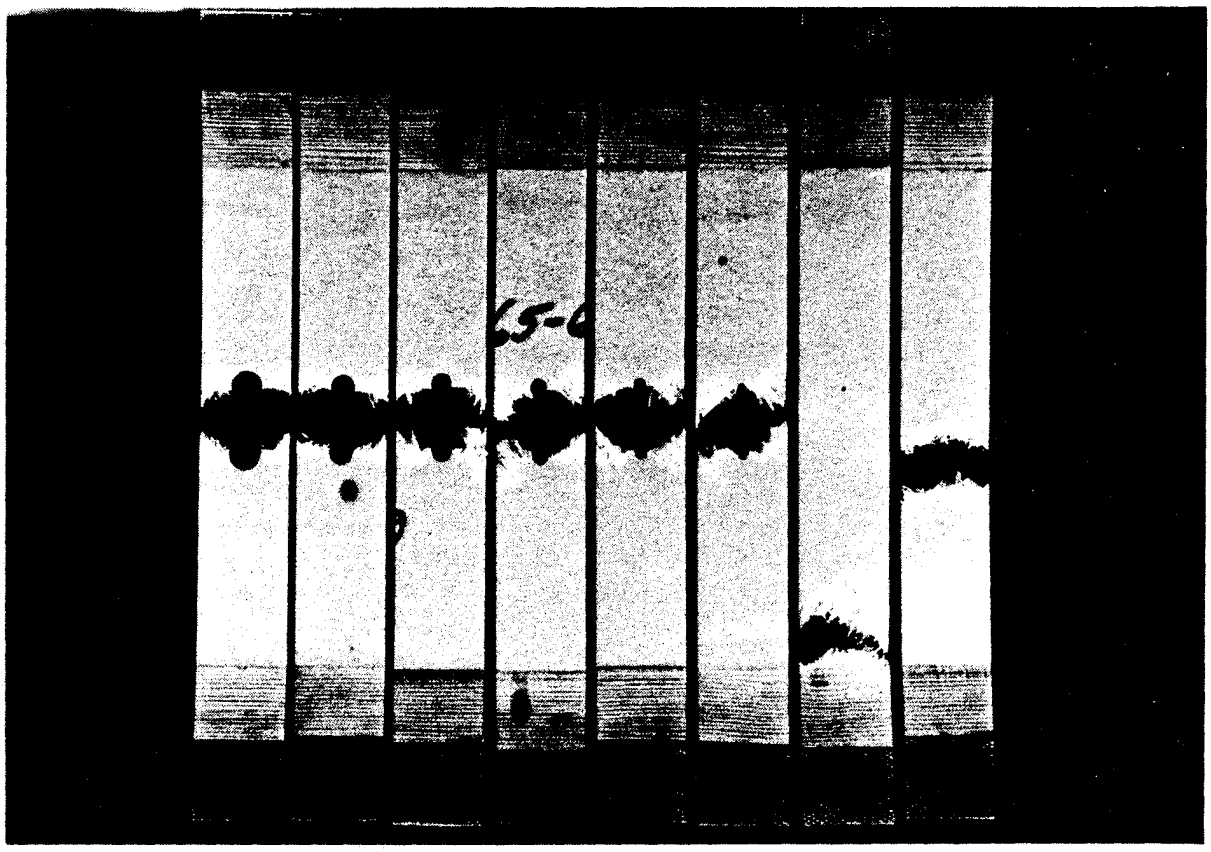

FIGURE 24. SMC-65 FRACTURED NOTCH SENSITIVITY SPECIMENS

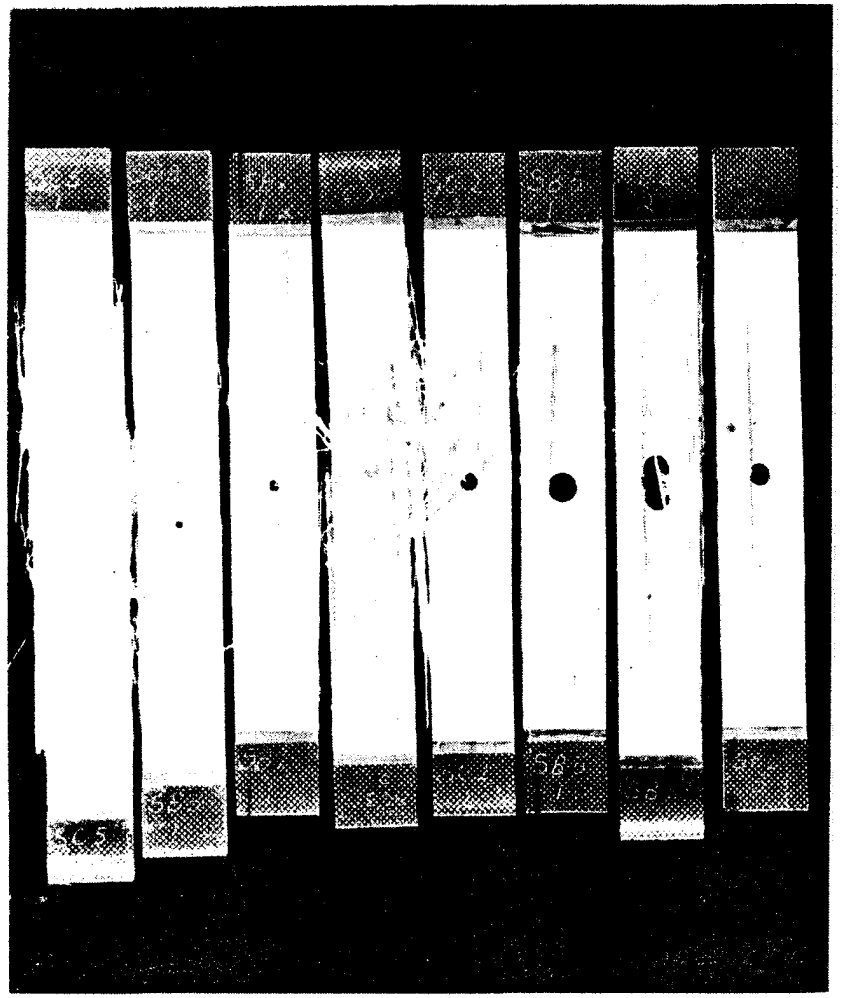

FIGURE 25. SMC-C20/R30
FRACTURED NOTCH SENSITIVITY SPECIMENS

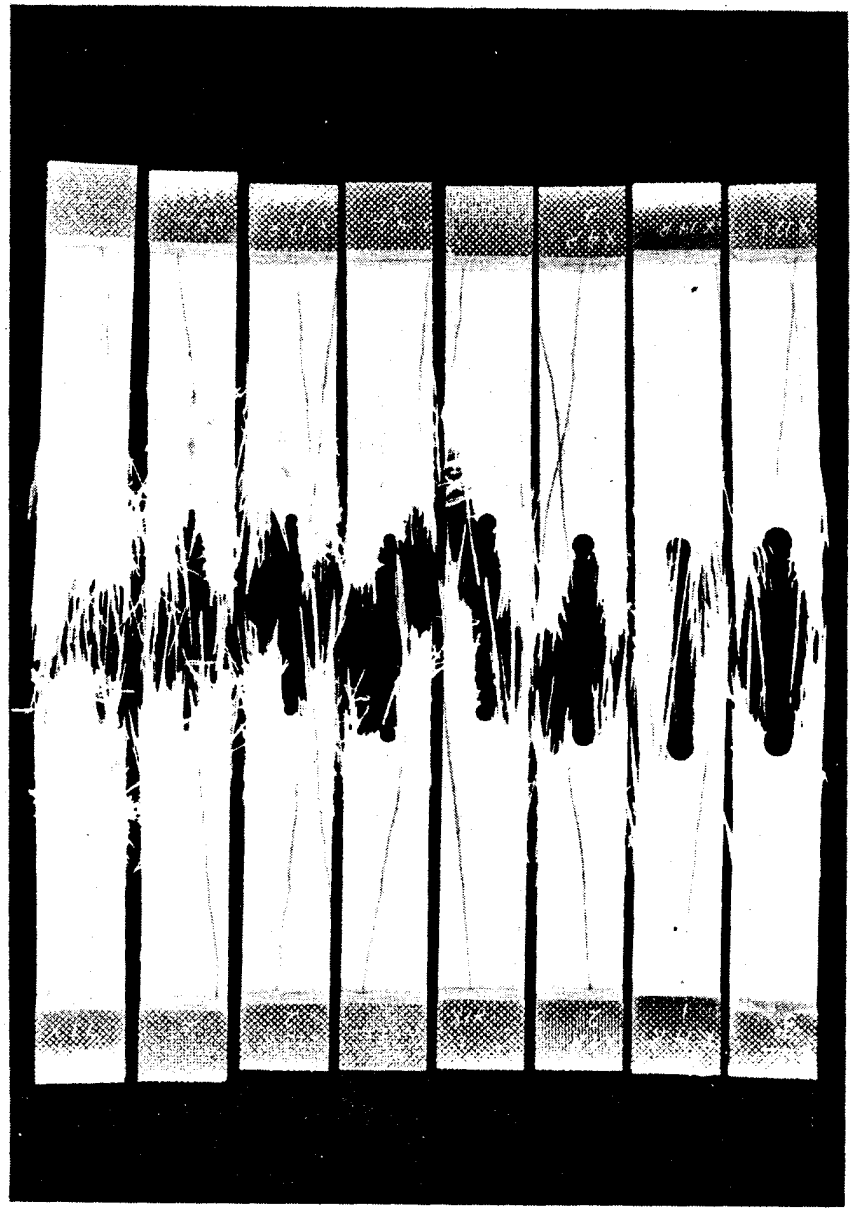

FIGURE 26. XMC-3 FRACTURED NOTCH SENSITIVITY SPECIMENS

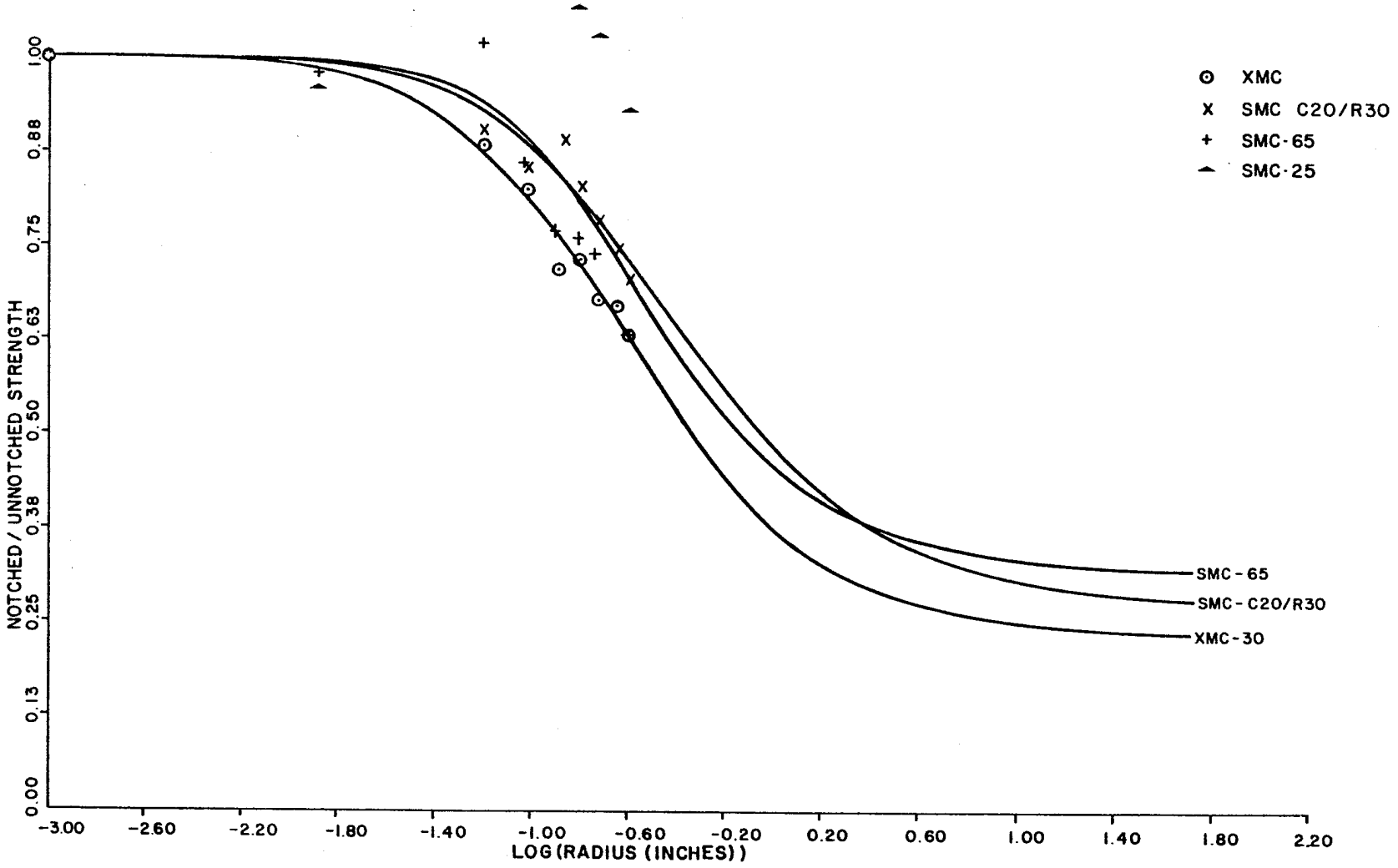

FIGURE 27. NOTCH SENSITIVITY CURVES FOR SMC-65, SMC C20/R30, XMC-3

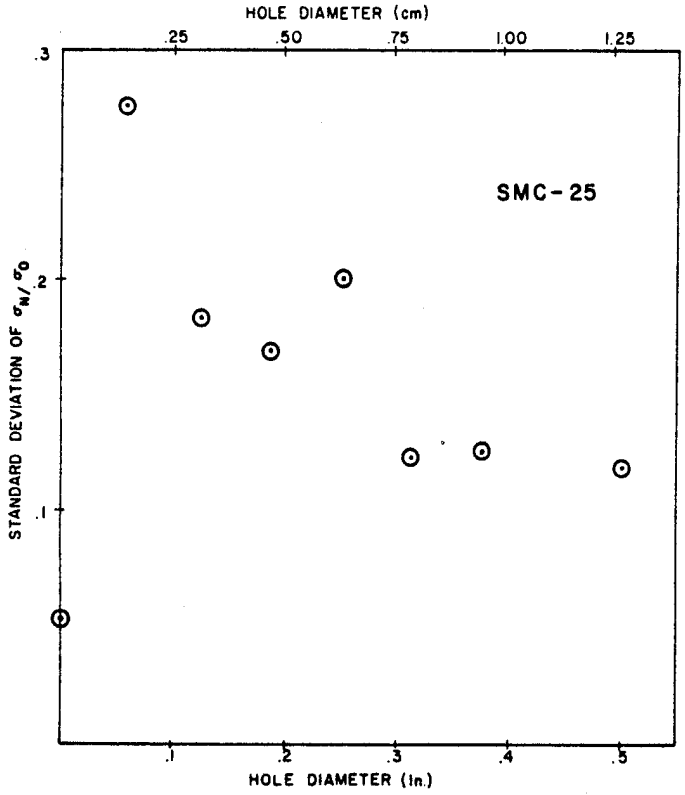

FIGURE 28. NOTCHED STRENGTH DATA - STANDARD DEVIATION VS. HOLE DIAMETER - SMC-25

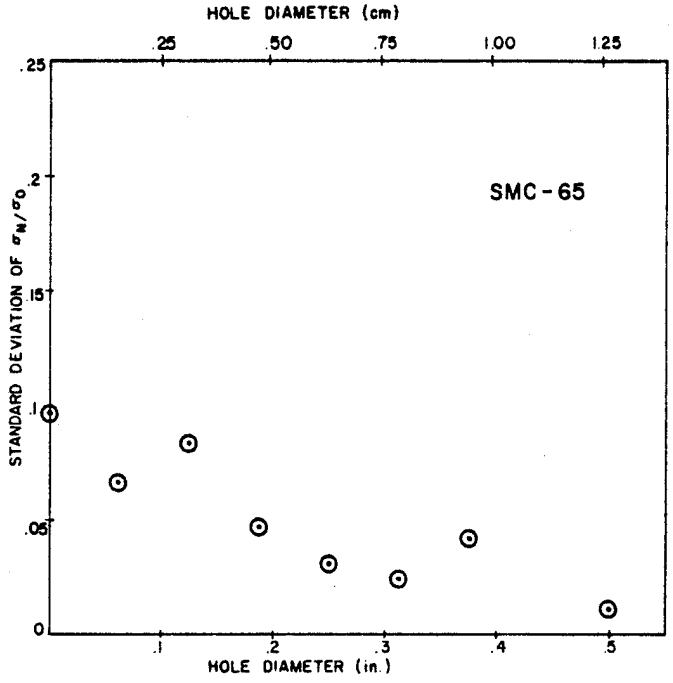

FIGURE 29. NOTCHED STRENGTH DATA - STANDARD DEVIATION VS. HOLE DIAMETER - SMC-65

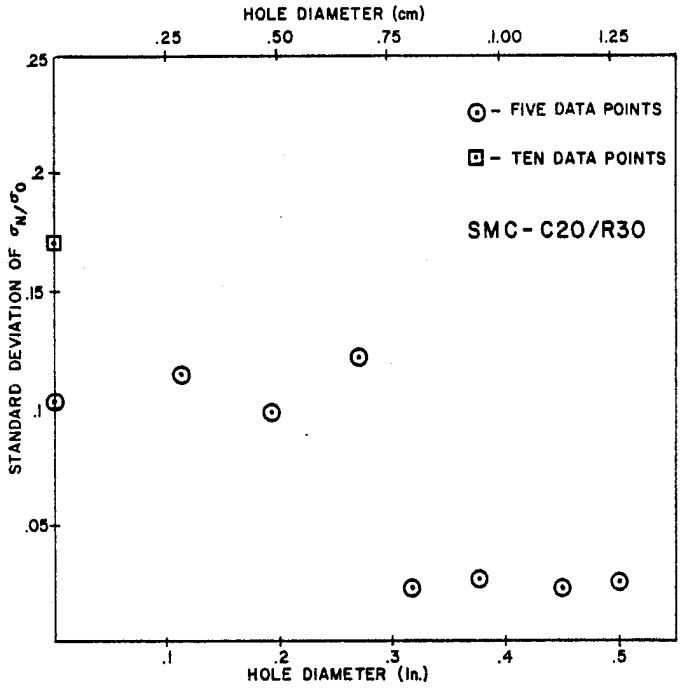

FIGURE 30. NOTCHED STRENGTH DATA - STANDARD DEVIATION VS. HOLE DIAMETER - SMC-C20/R30

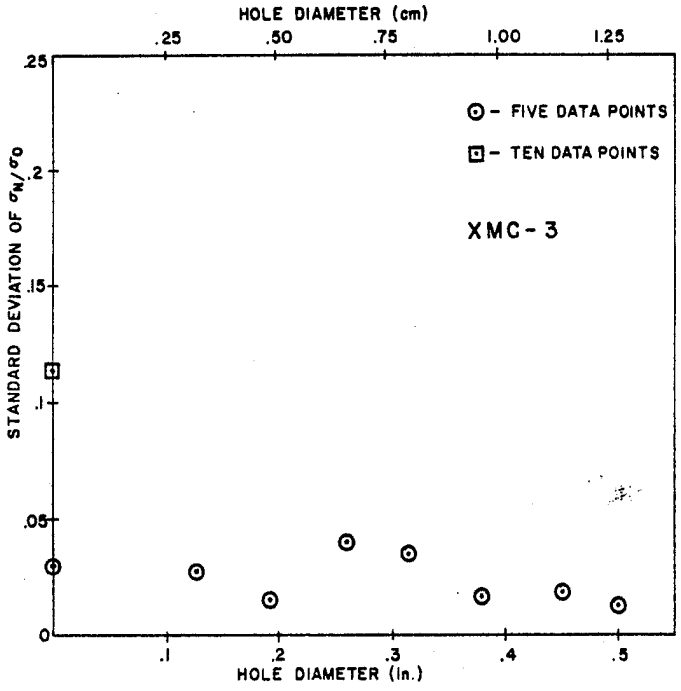

FIGURE 31. NOTCHED STRENGTH DATA - STANDARD DEVIATION VS. HOLE DIAMETER - XMC-3

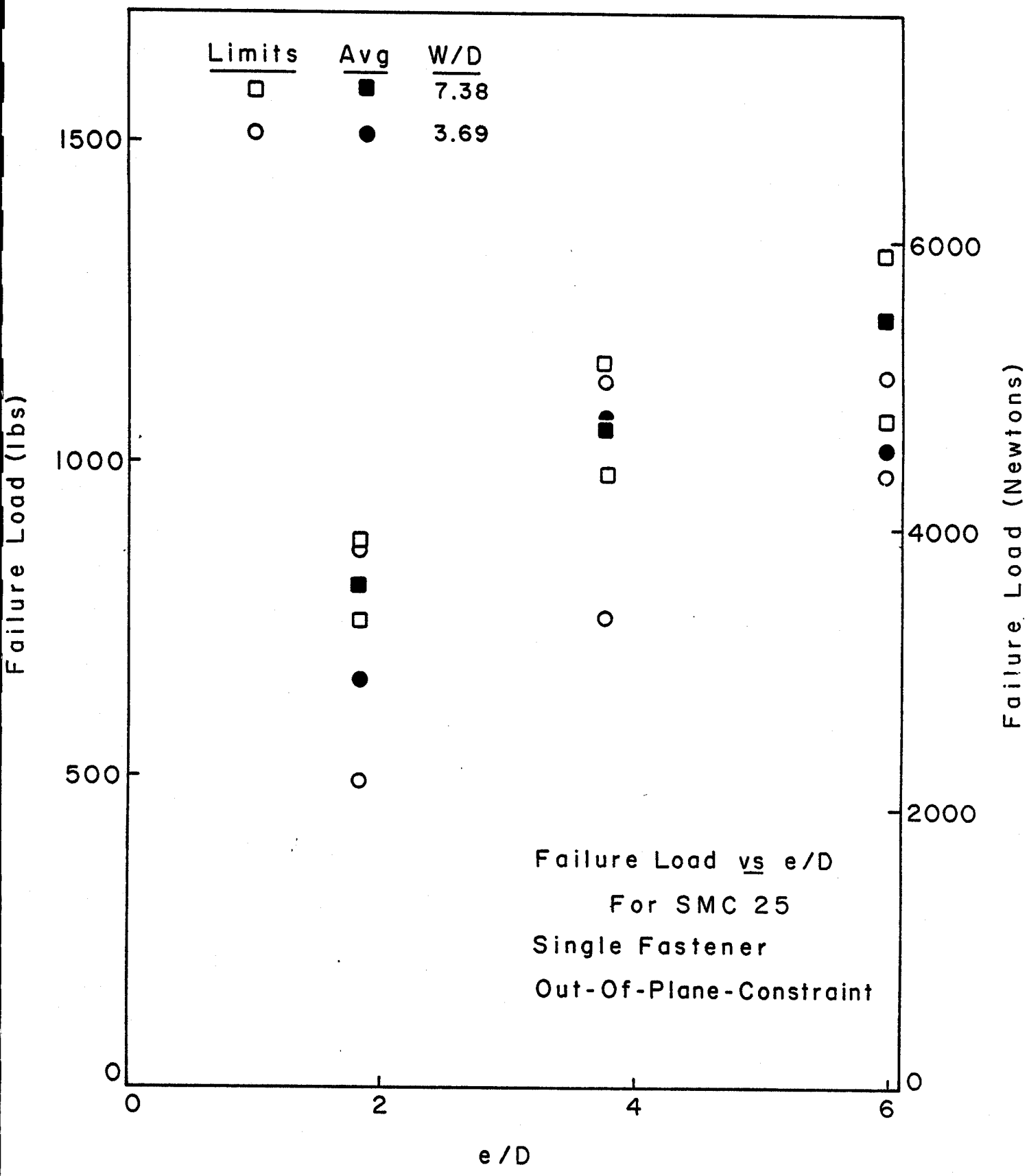

FIGURE 32. BOLTED JOINT TEST RESULTS FOR SMC-25

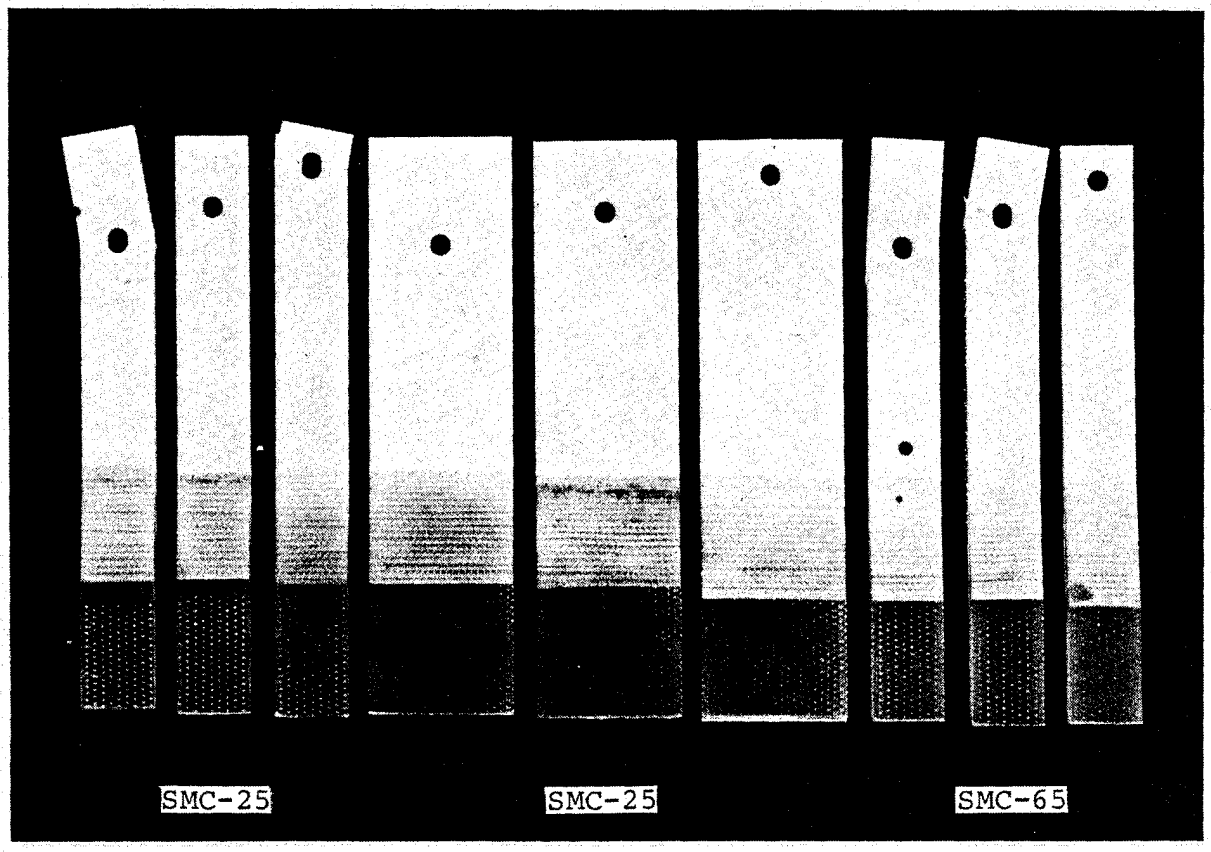

FIGURE 33. FRACTURED BOLTED JOINT SPECIMENS

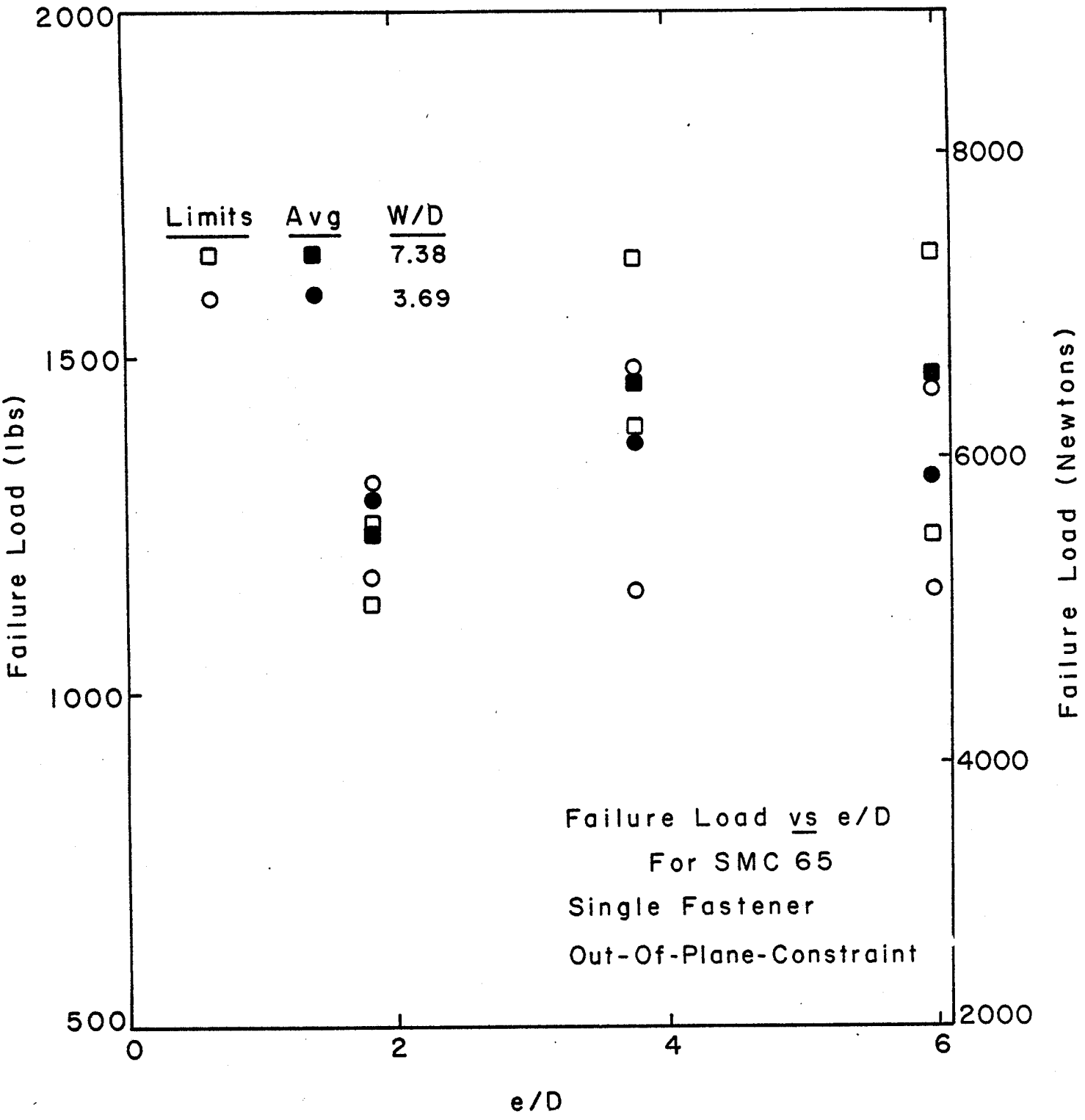

FIGURE 34. BOLTED JOINT TEST RESULTS FOR SMC-65

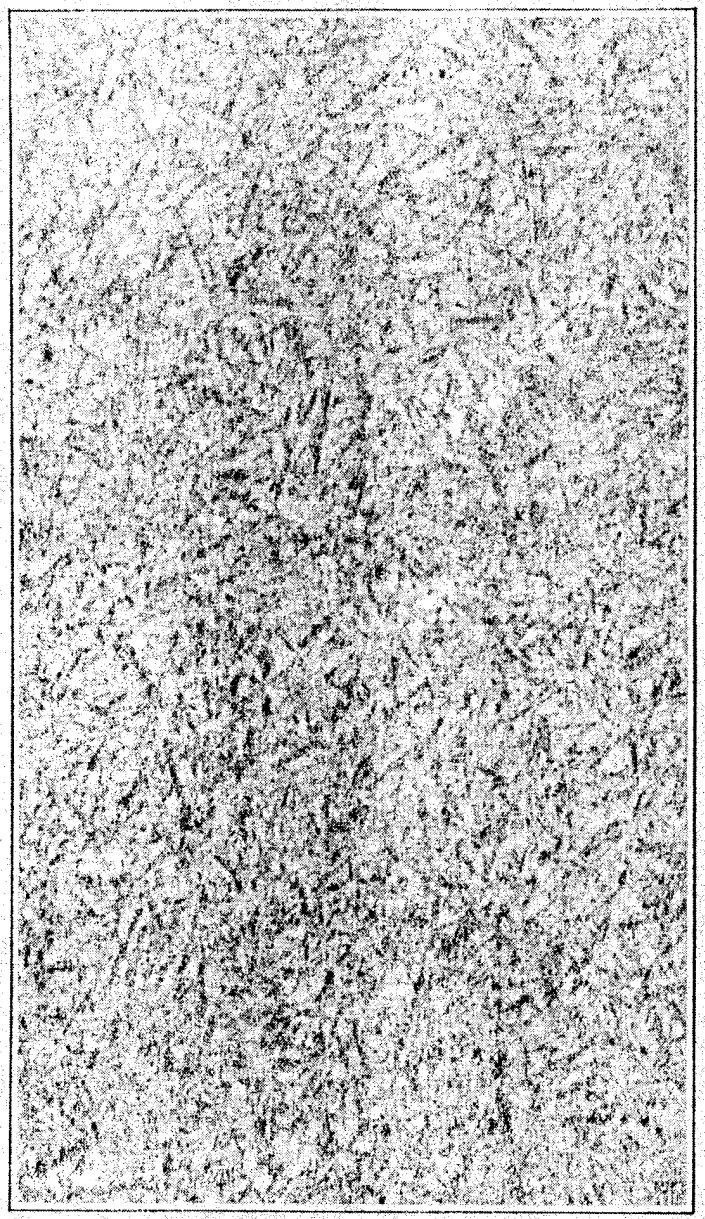

FIGURE 35. C-SCAN - SMC - 25

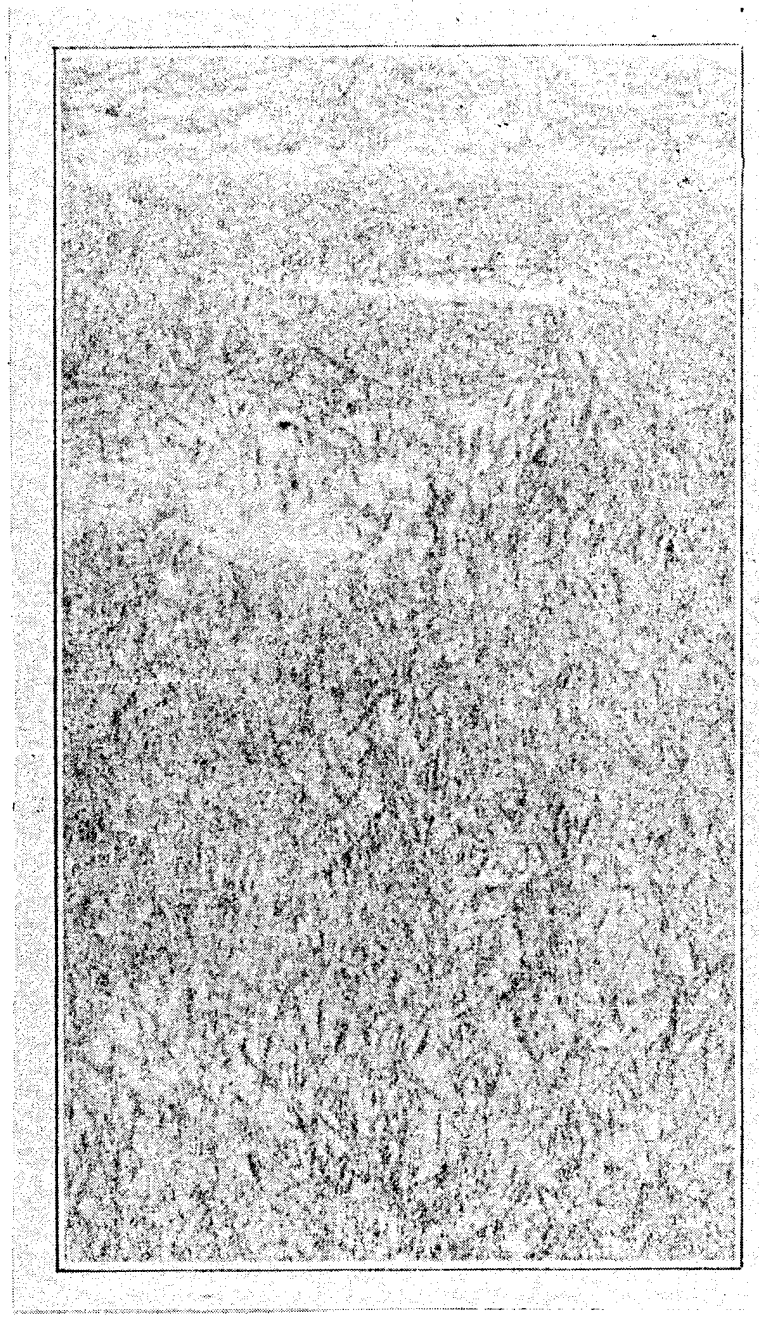

FIGURE 36. FIBER DEPLETED REGIONS IN SMC - 25

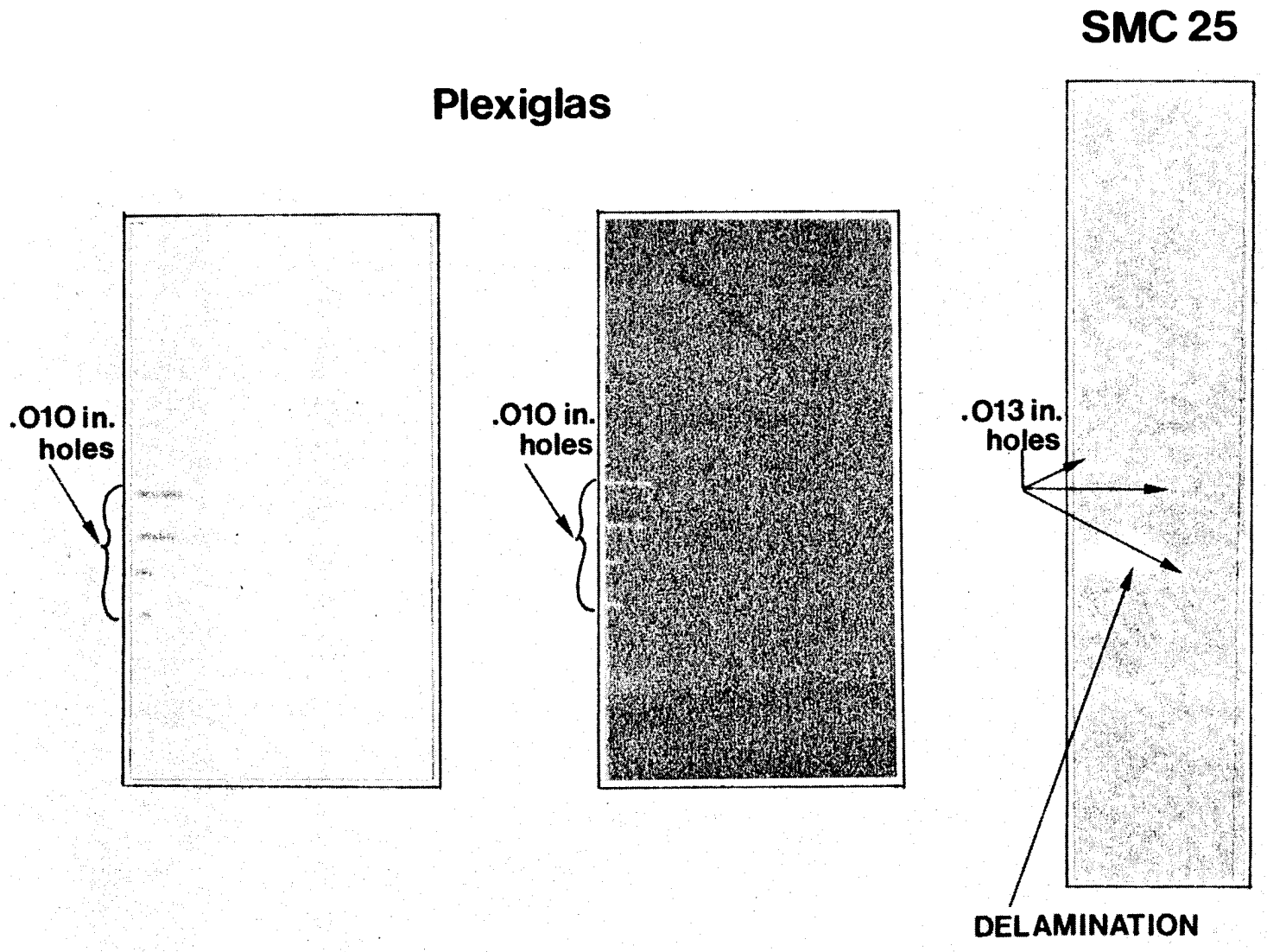

FIGURE 37. C-SCANS OF HOLES IN SMC - 25 AND PLEXIGLAS

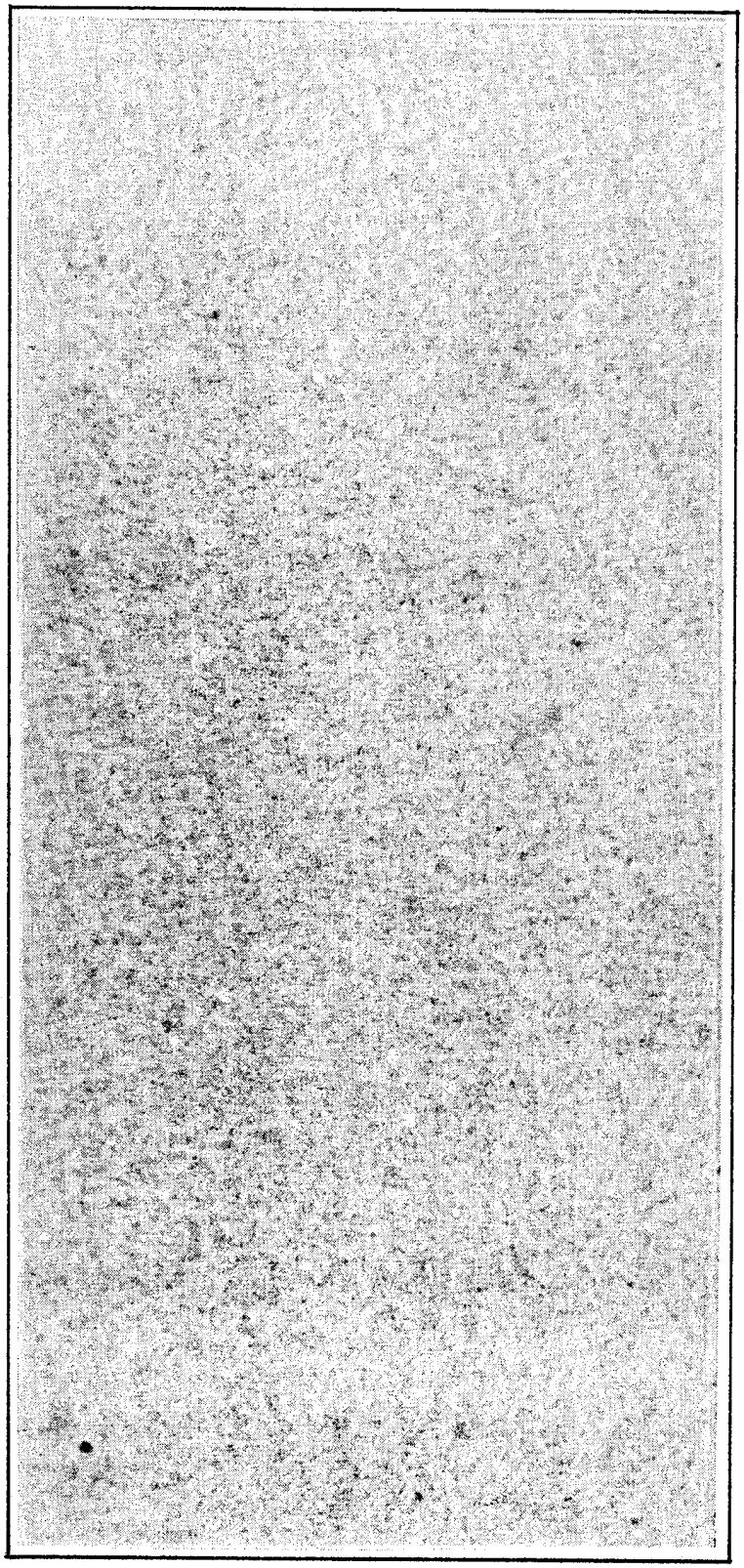

FIGURE 38. NEAR FIELD SMC-65 BACK SURFACE GATE

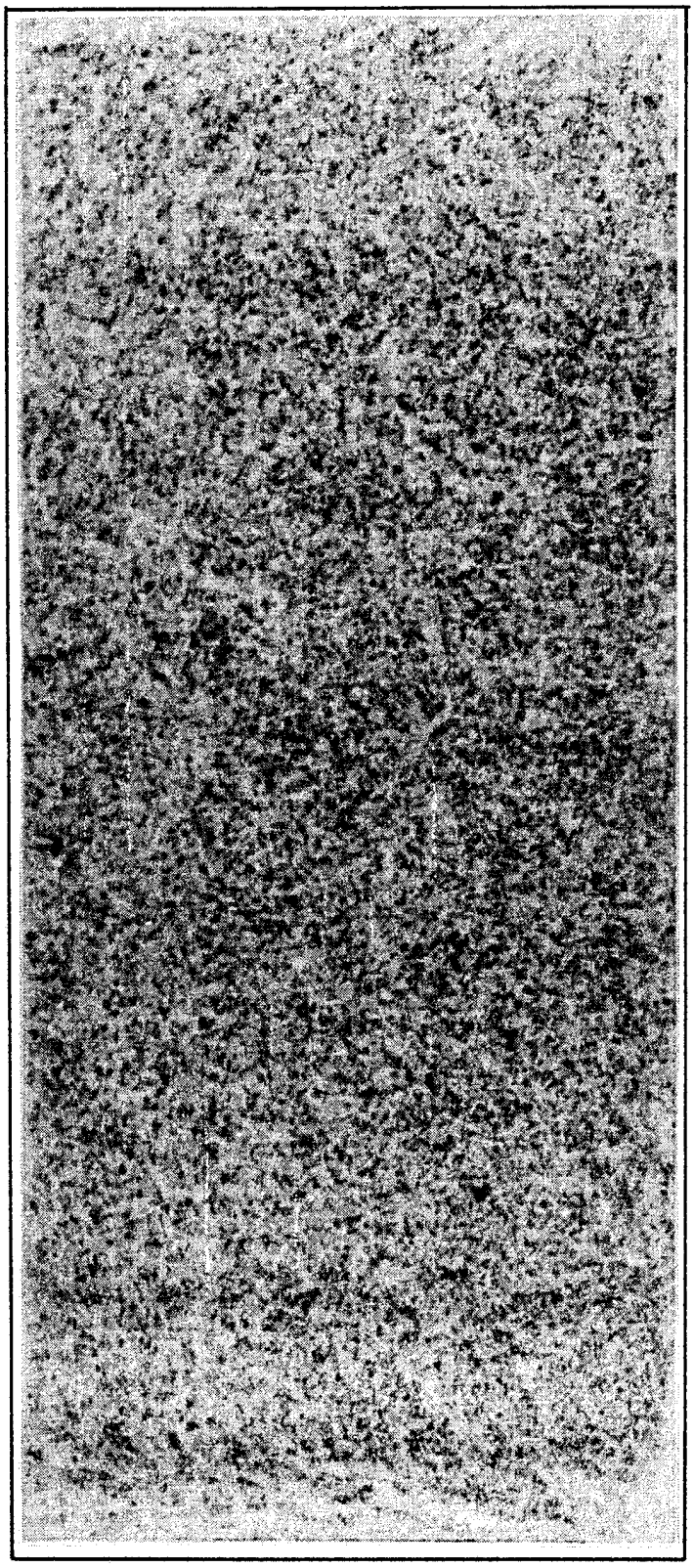

FIGURE 39. NEAR FIELD SMC-65 NEAR SURFACE GATE

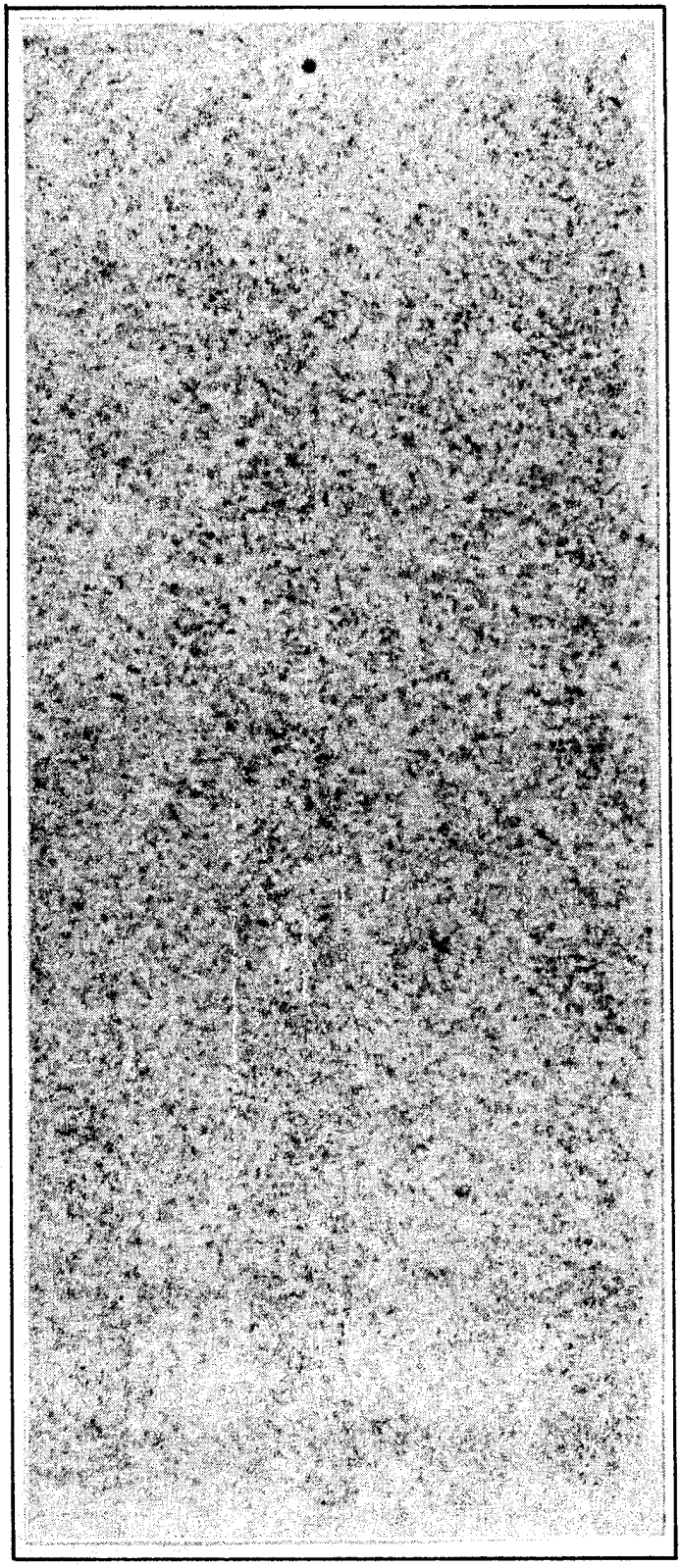

FIGURE 40. FAR FIELD SMC-65 BACK SURFACE GATE

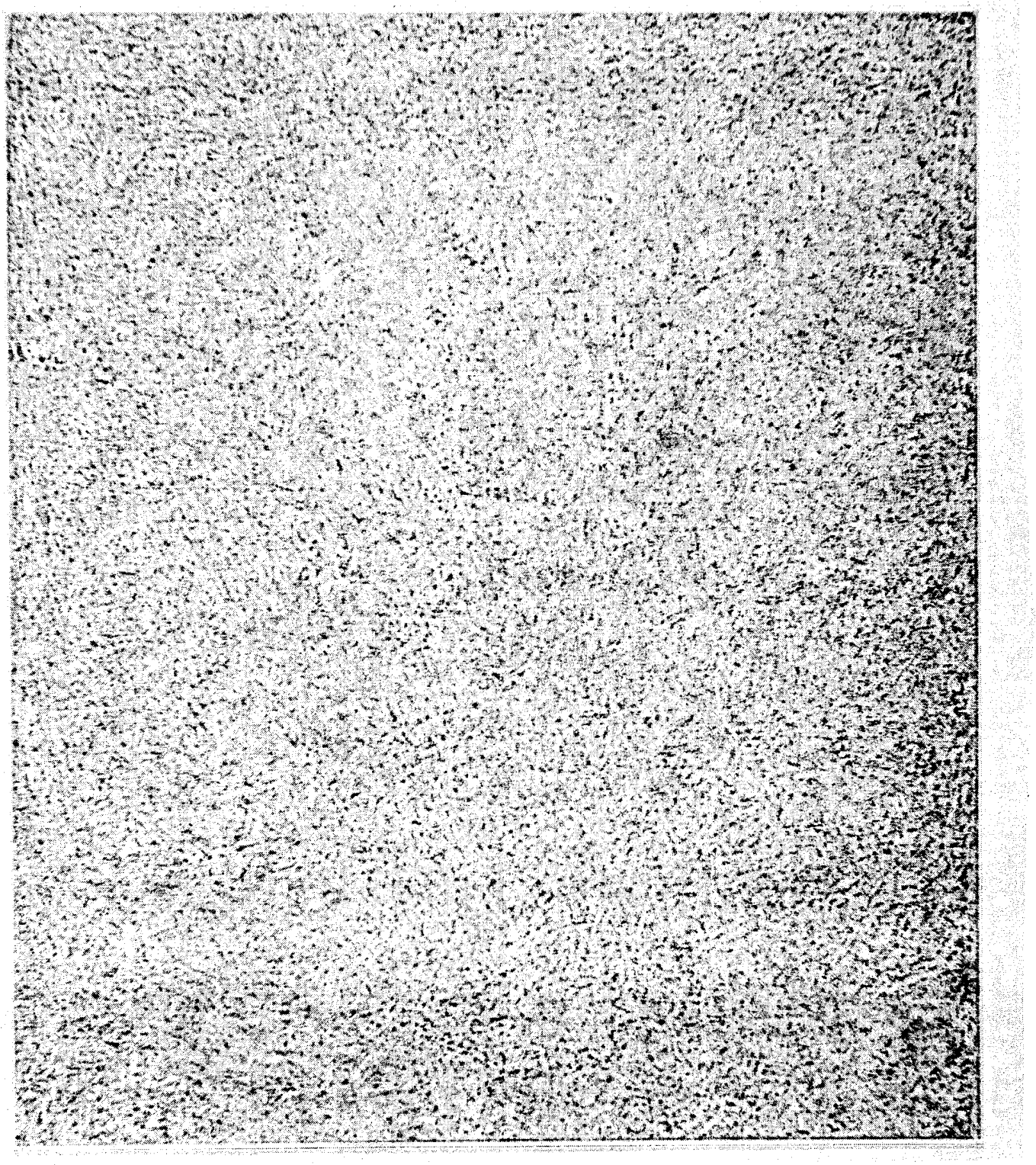

FIGURE 41. SMC-65 SURFACE C-SCAN

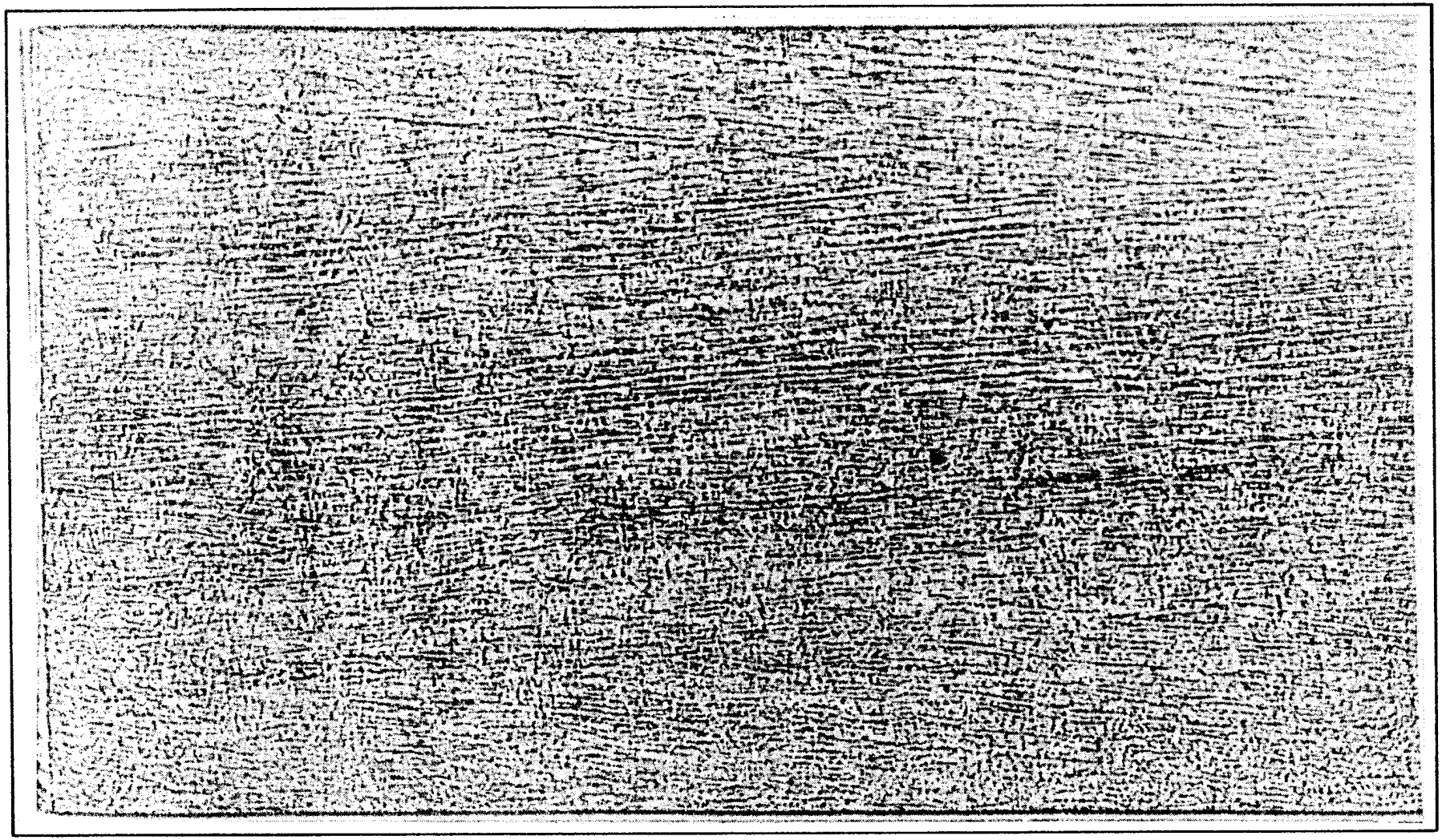

FIGURE 42. C-SCAN - XMC-3

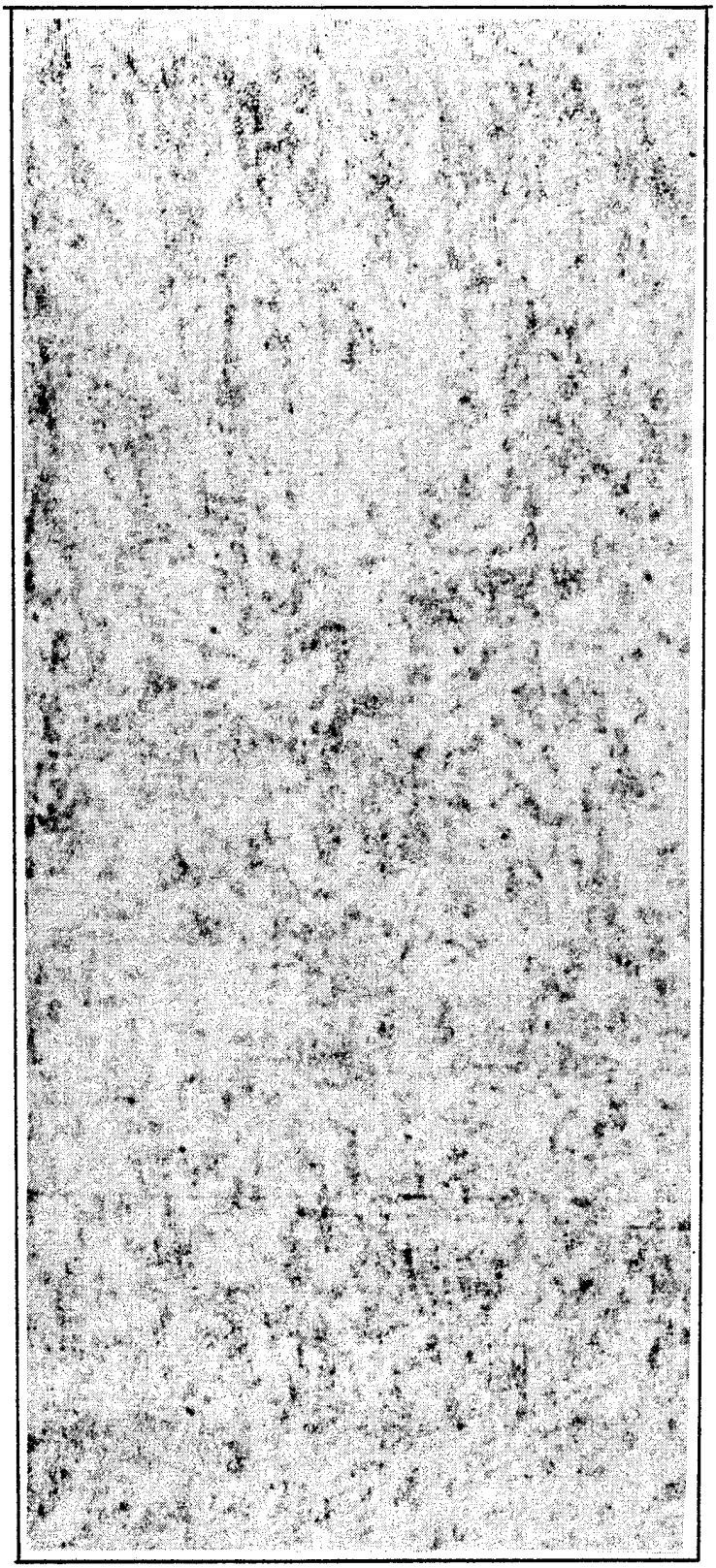

FIGURE 43. DARK FIELD C-SCAN - SMC-65 - 10° ANGLE

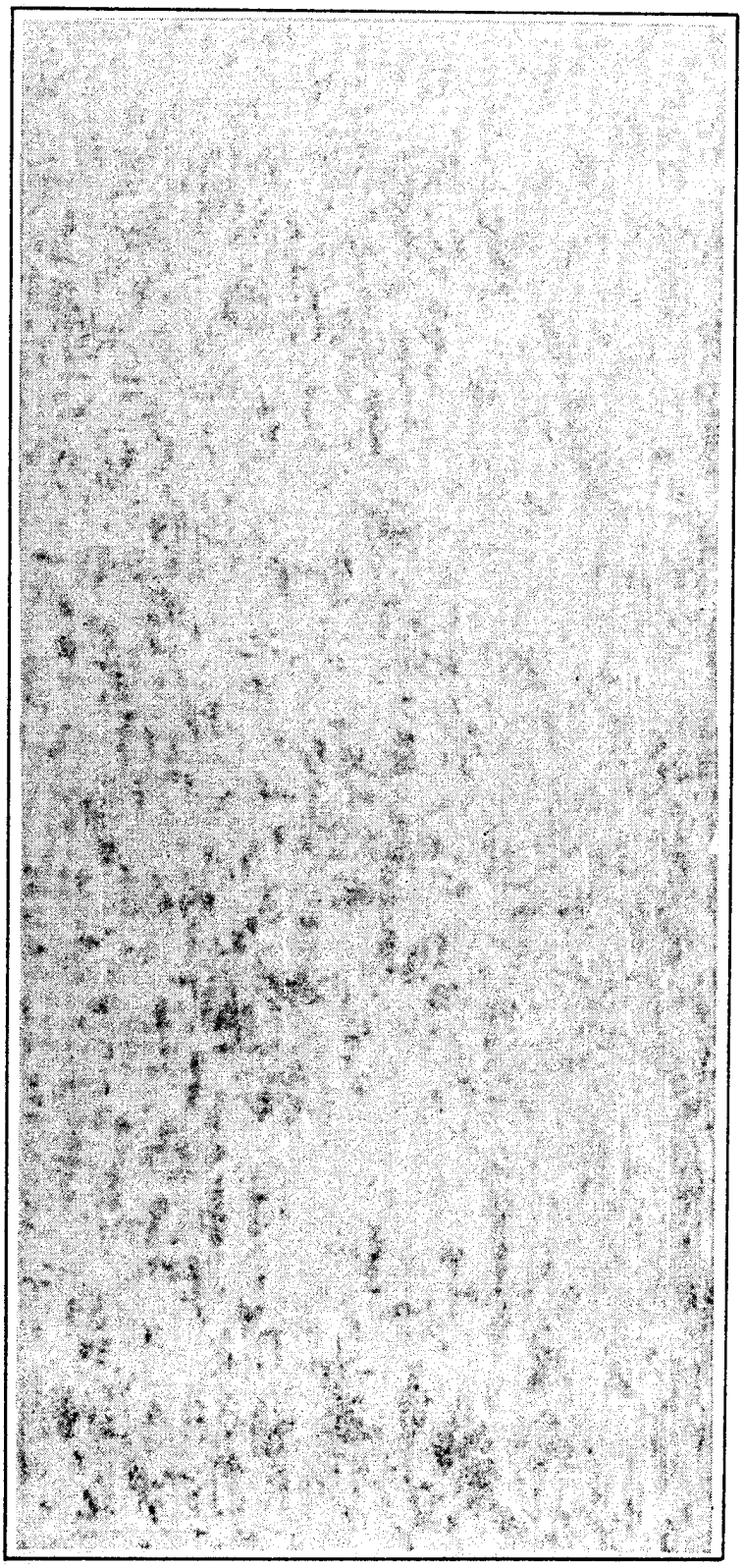

FIGURE 44. DARK FIELD C-SCAN - SMC-65 - 20° ANGLE

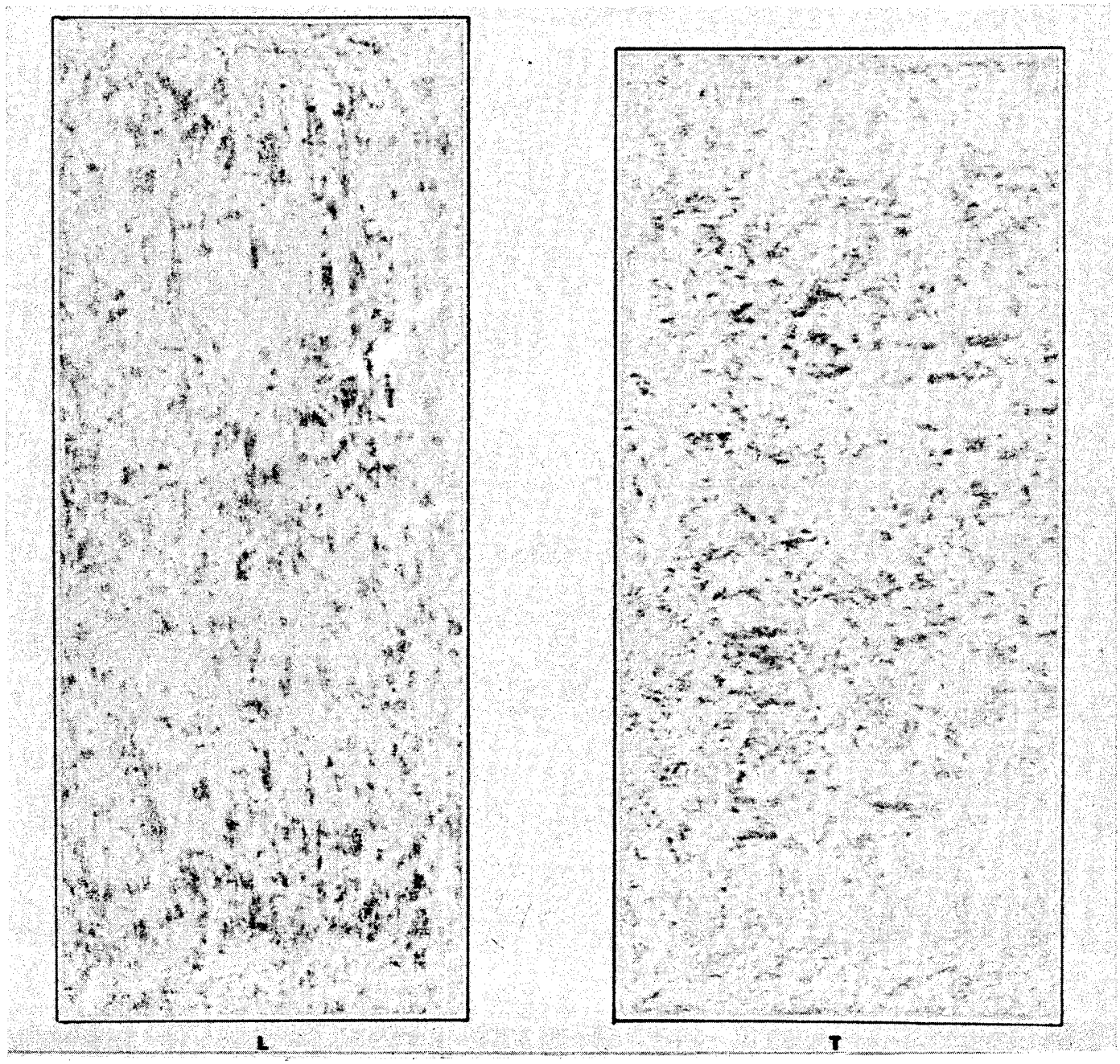

FIGURE 45. DARK FIELD C-SCAN - SMC-65 - 30° ANGLE

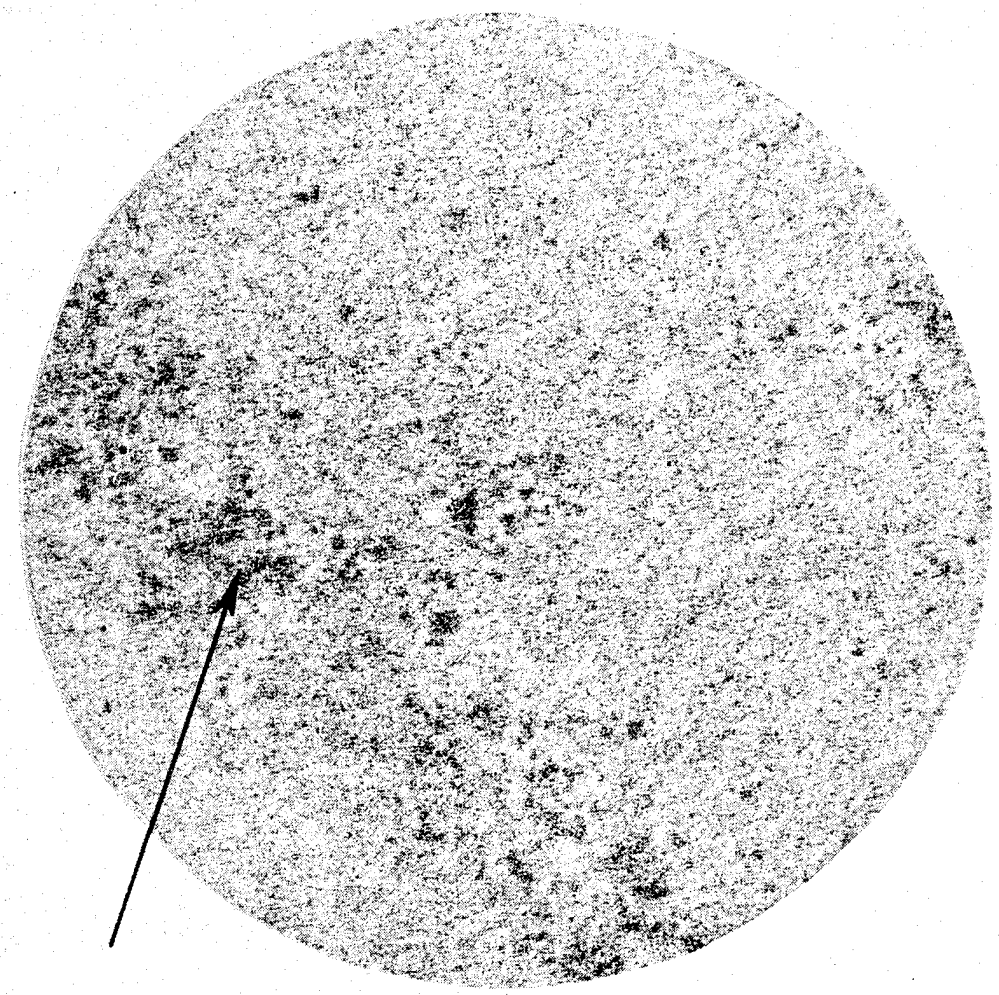

FIGURE 46. C-SCANS OF VOIDS IN SMC-65

FIGURE 47. VOID IN SMC-65

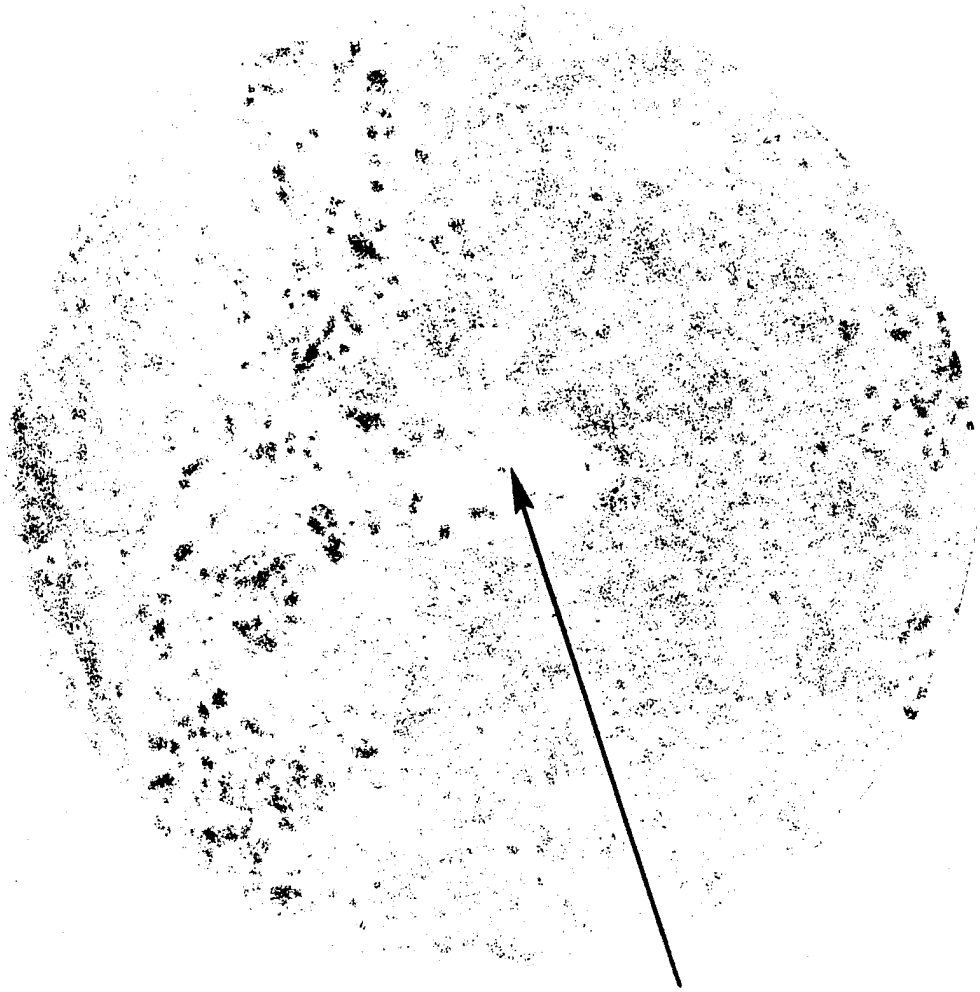

FIGURE 48. SMC-65 DELAMINATION

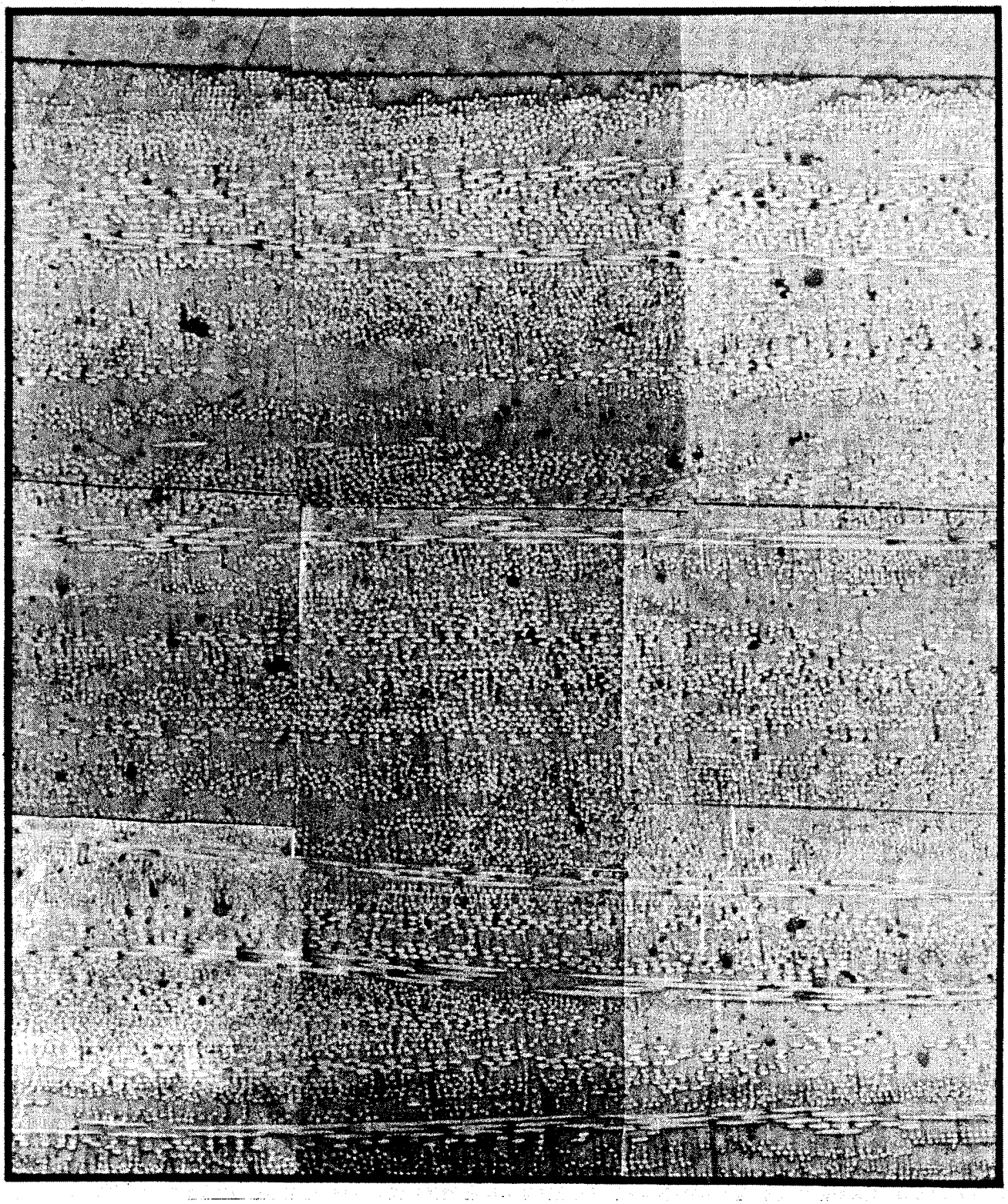

FIGURE 49. PHOTOMICROGRAPH OF SMC-65 - LONGITUDINAL

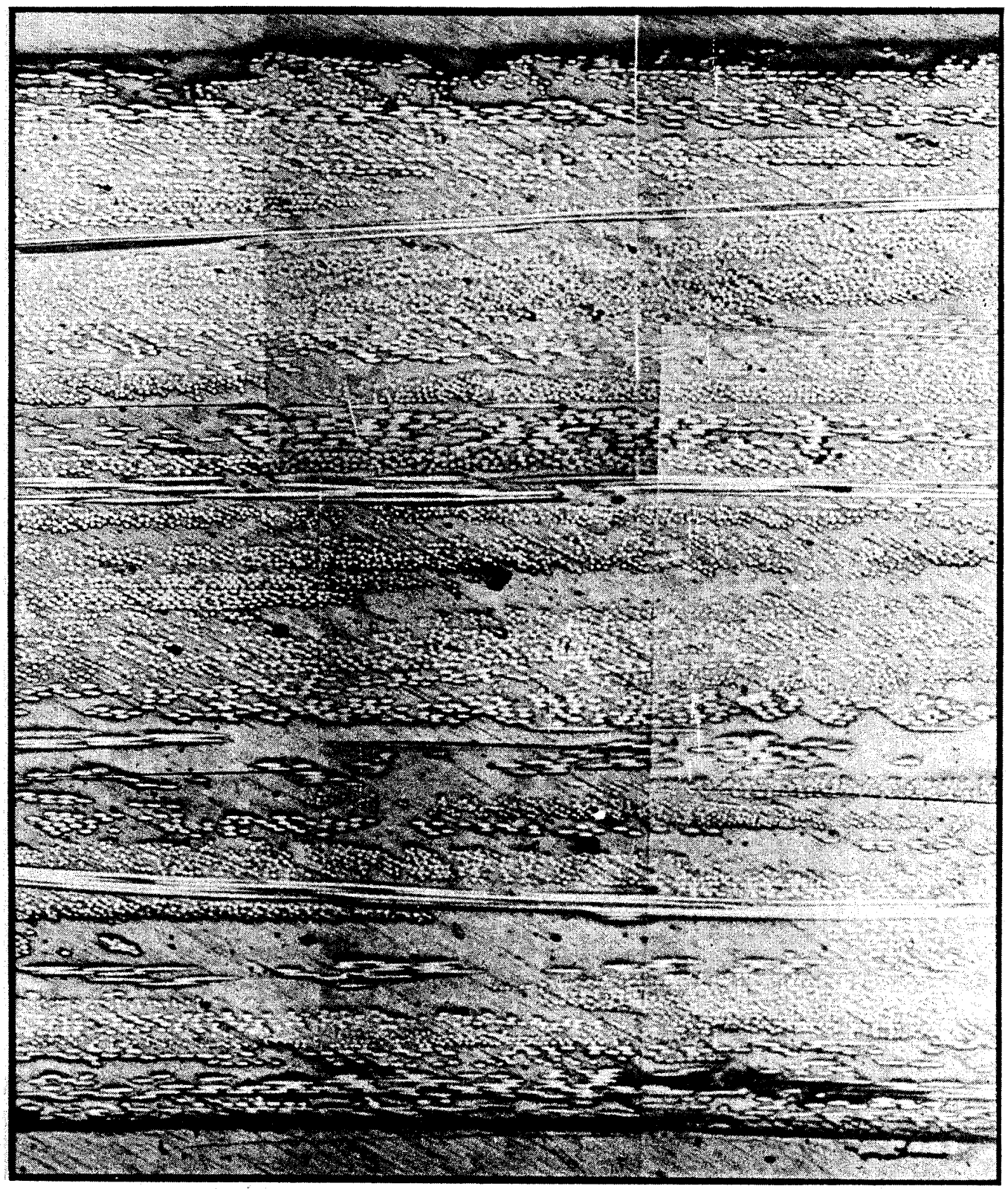

FIGURE 50. PHOTOMICROGRAPH OF SMC-65 - TRANSVERSE

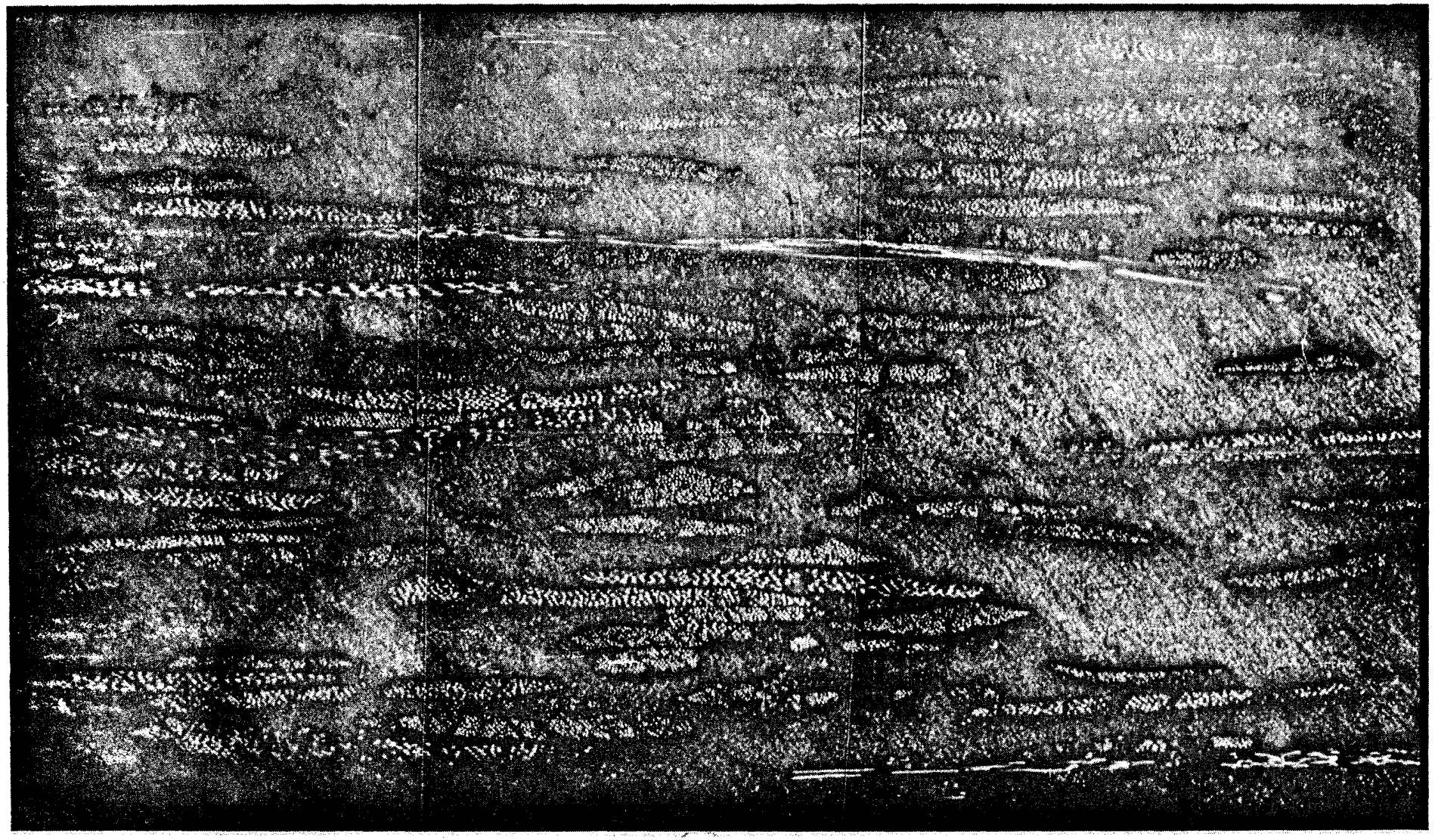

FIGURE 51. PHOTOMICROGRAPH OF SMC - 25 - LONGITUDINAL

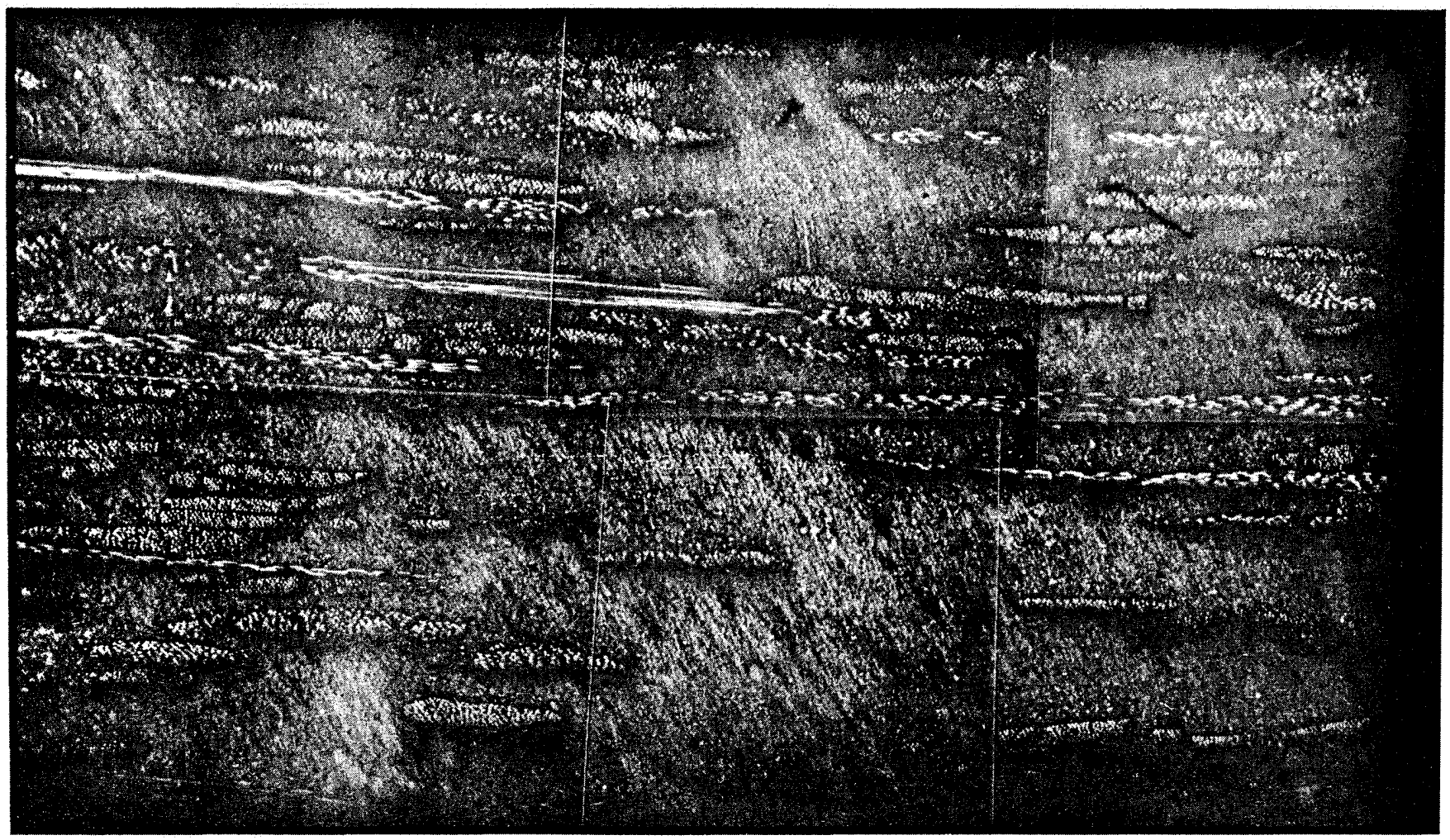

FIGURE 52. PHOTOMICROGRAPH OF SMC-25 - TRANSVERSE

FIGURE 53. PHOTOMICROGRAPH OF SURFACE - SMC-25

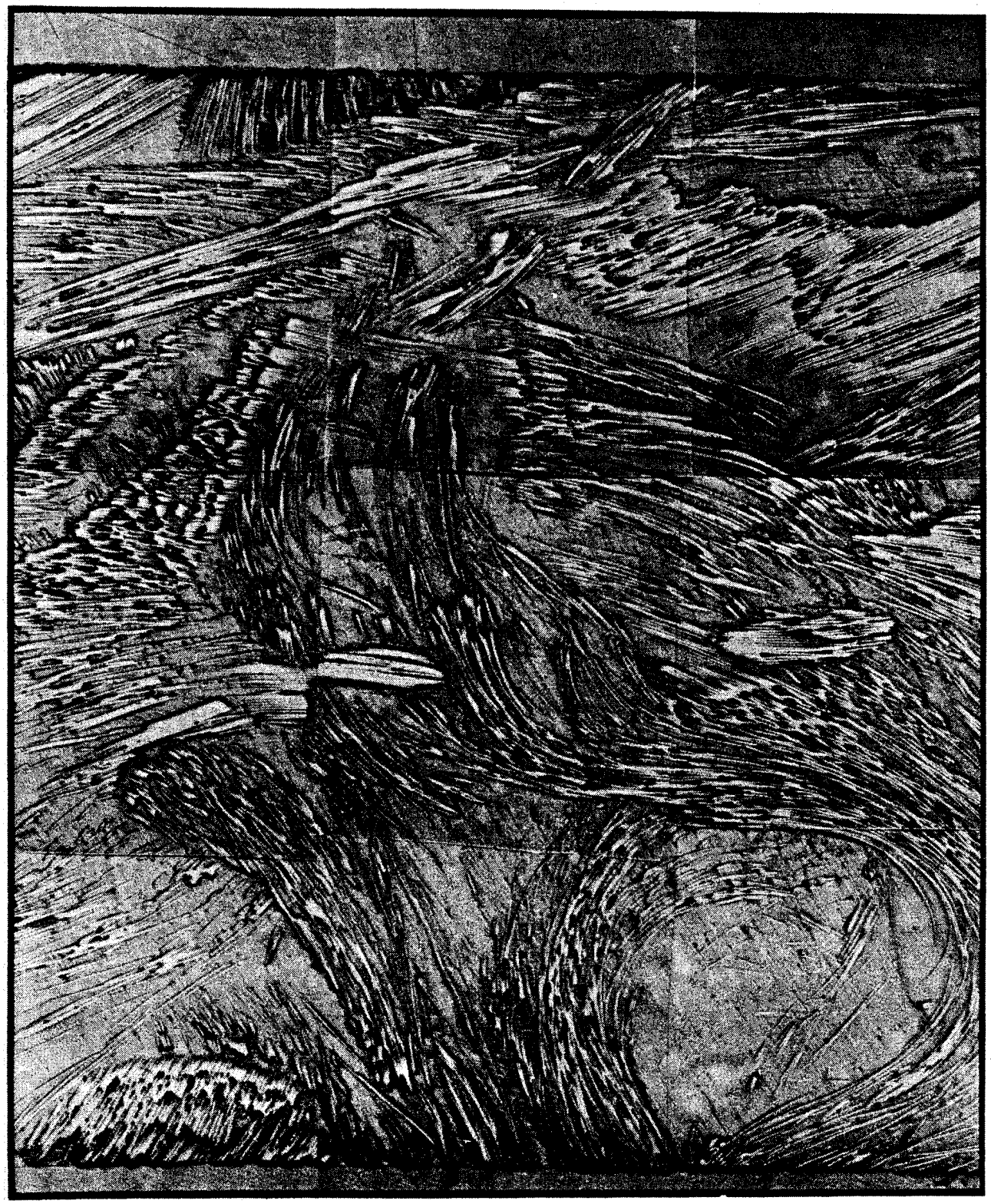

FIGURE 54. PHOTOMICROGRAPH OF SURFACE - SMC-65

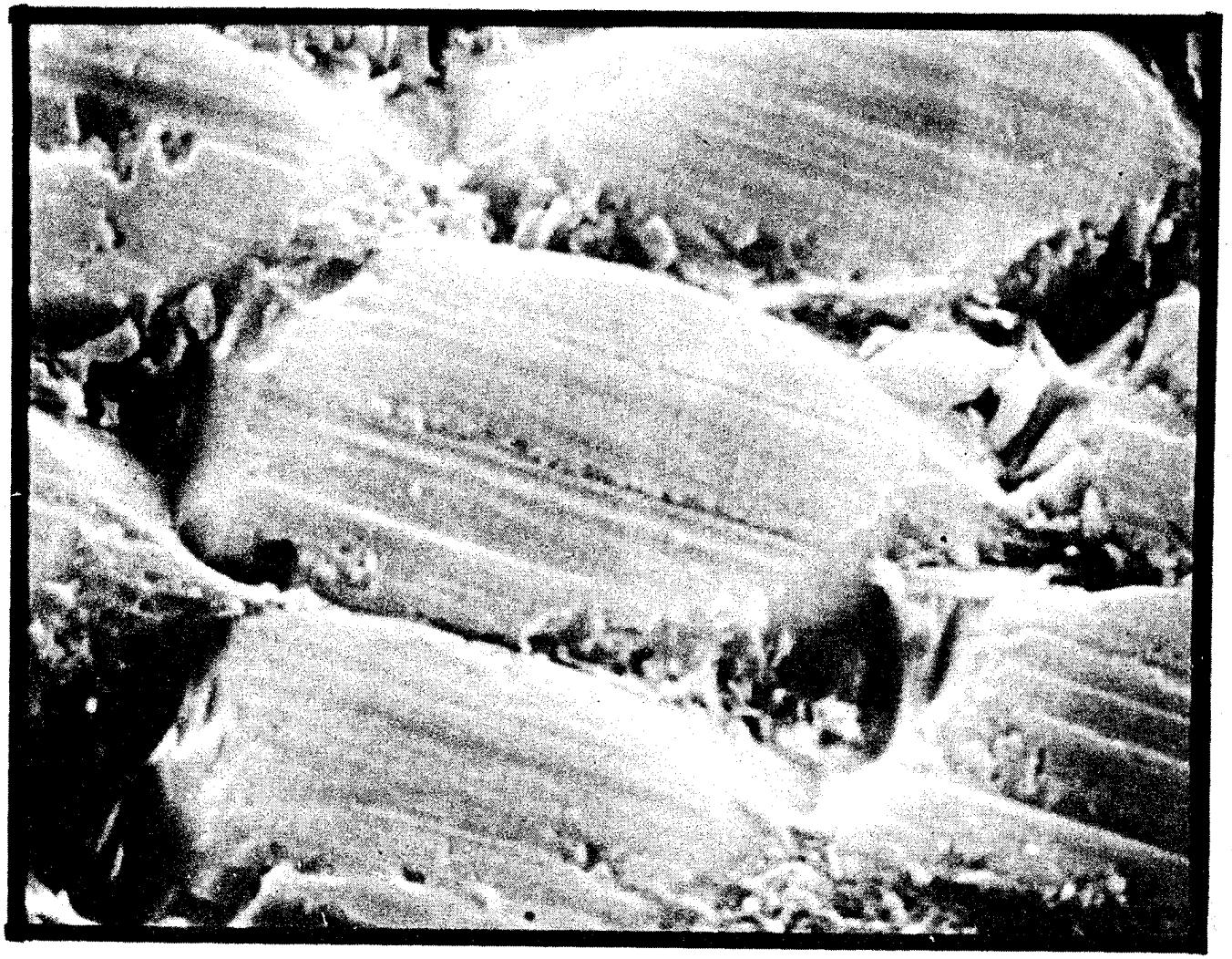

FIGURE 55. SCANNING ELECTRON MICROGRAPH - SMC - 25

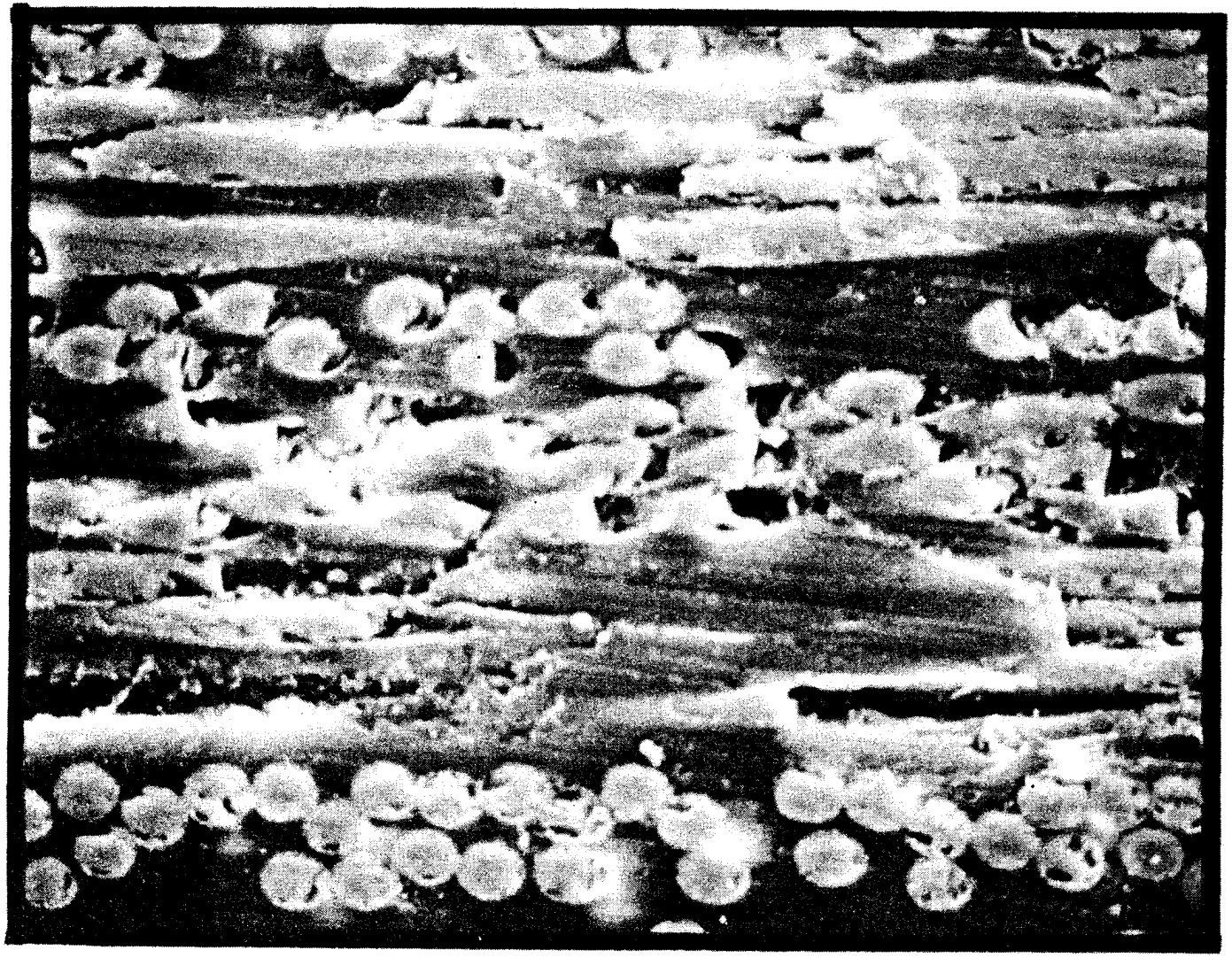

FIGURE 56. SCANNING ELECTRON MICROGRAPH - SMC - 65

FIGURE 57. PHOTOMICROGRAPH OF SMC-C20/R30

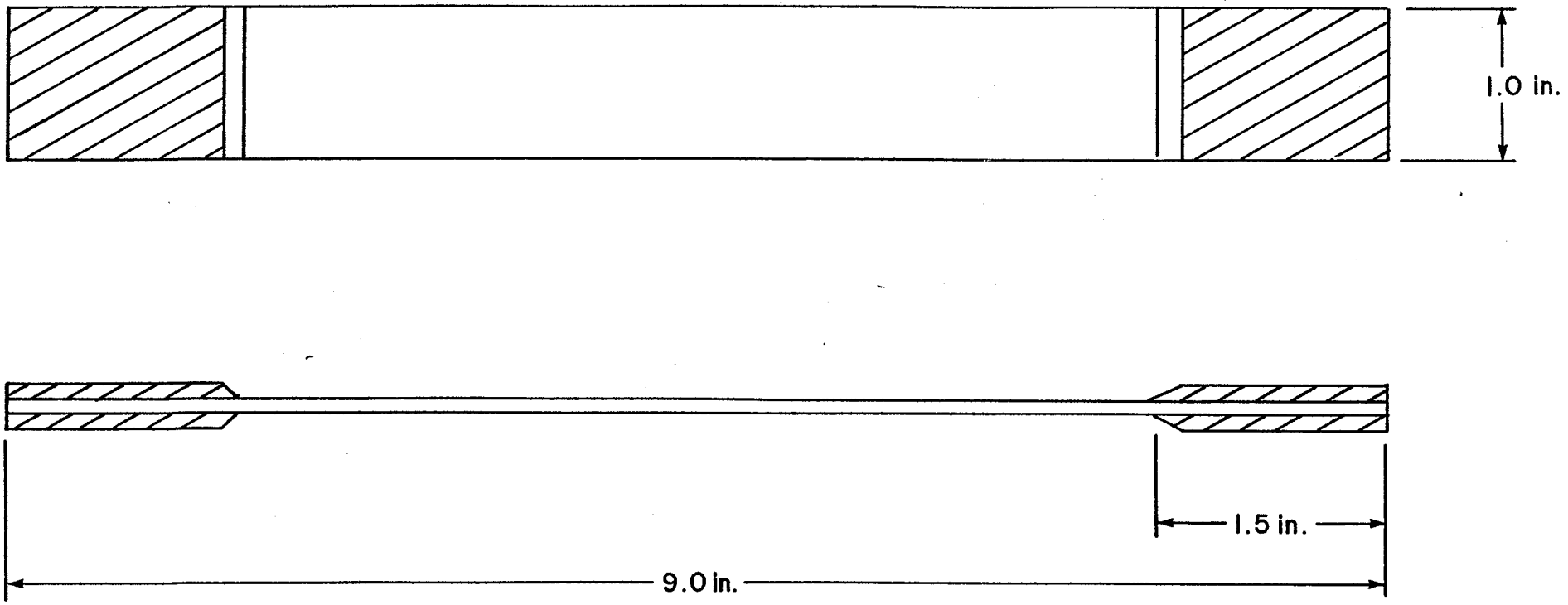

FIGURE 58. TENSILE TEST SPECIMENS

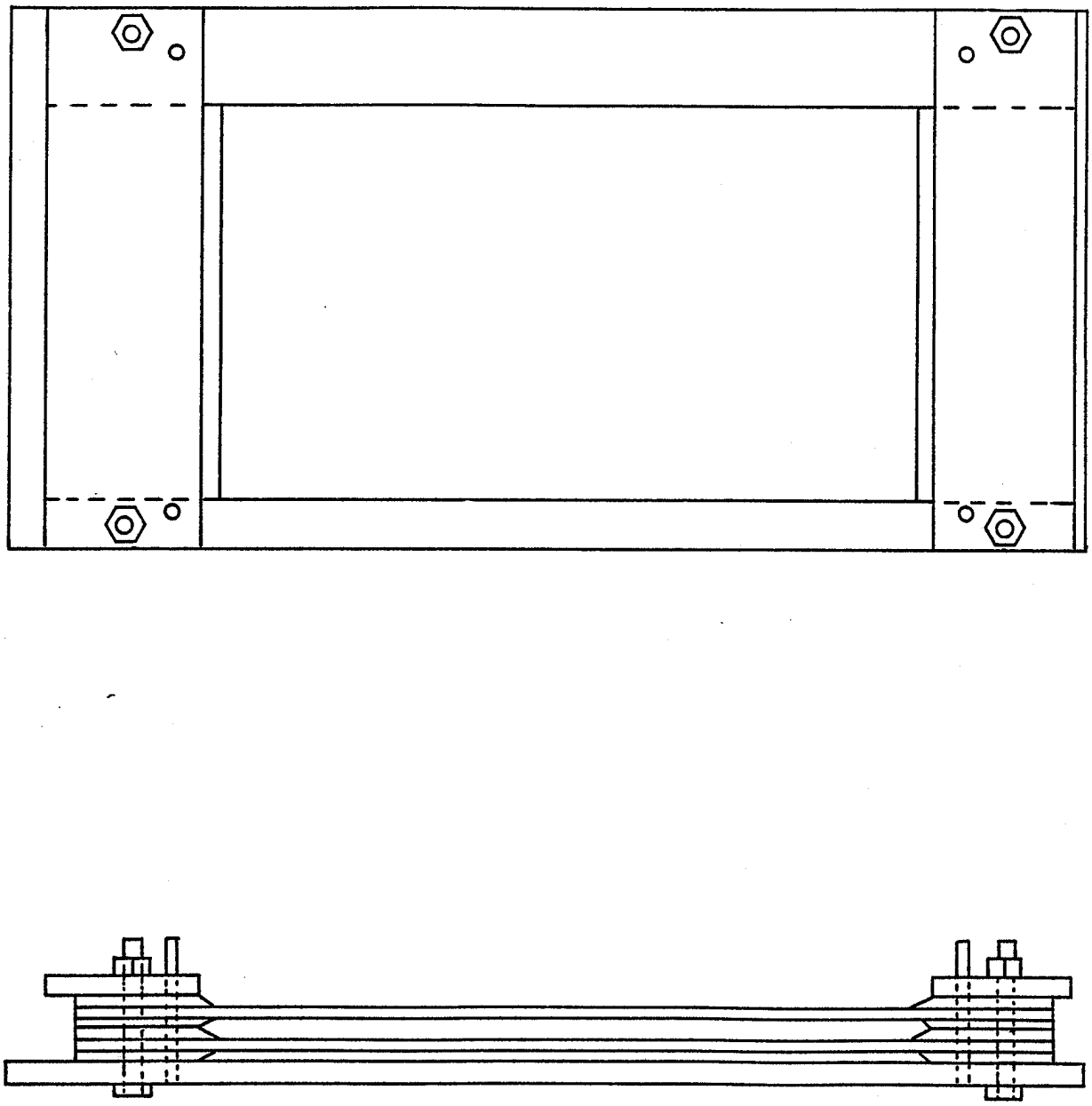

FIGURE 59. TENSION END TAB BONDING FIXTURE

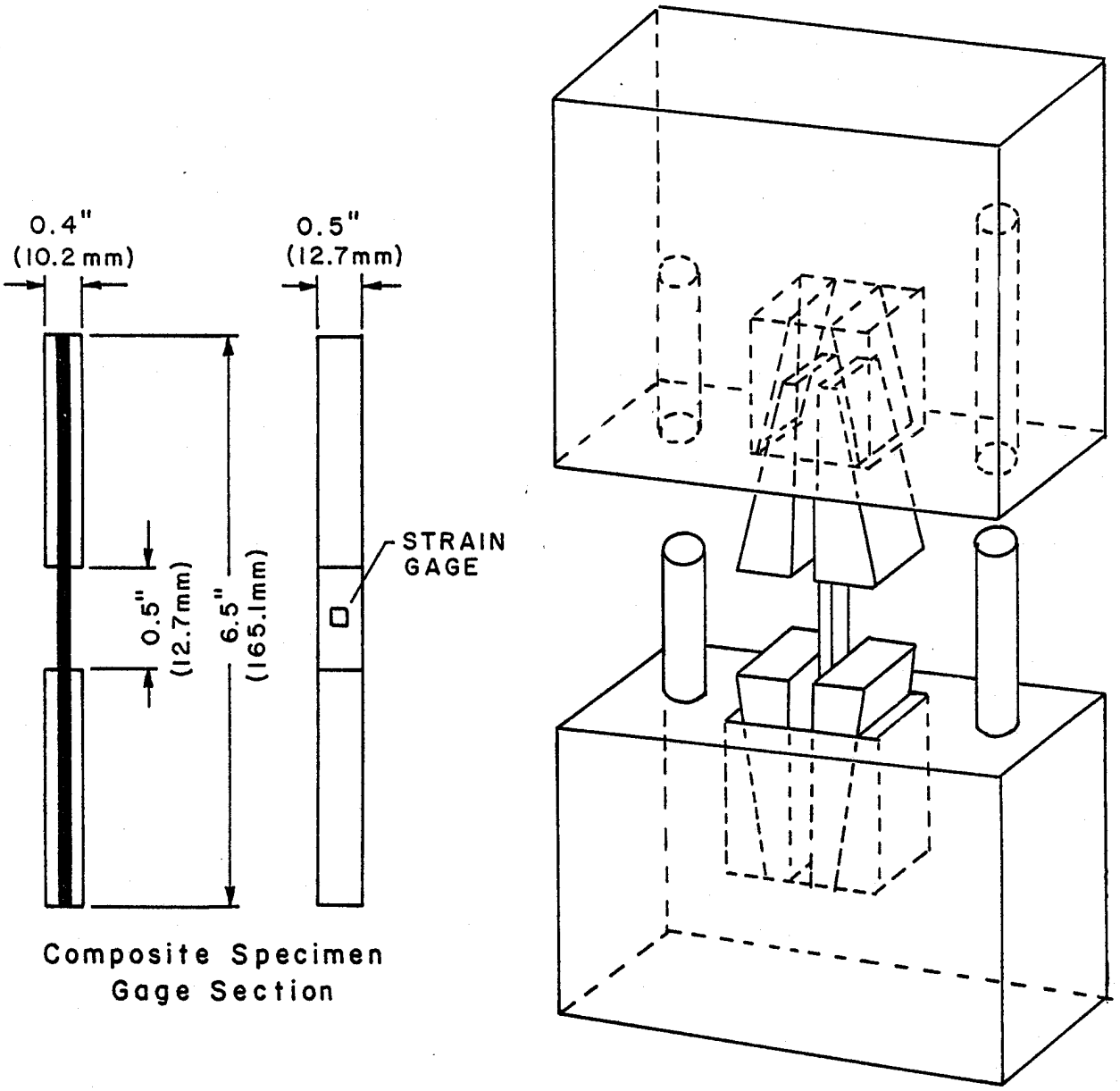

FIGURE 60. MODIFIED IITRI COMPRESSION FIXTURE

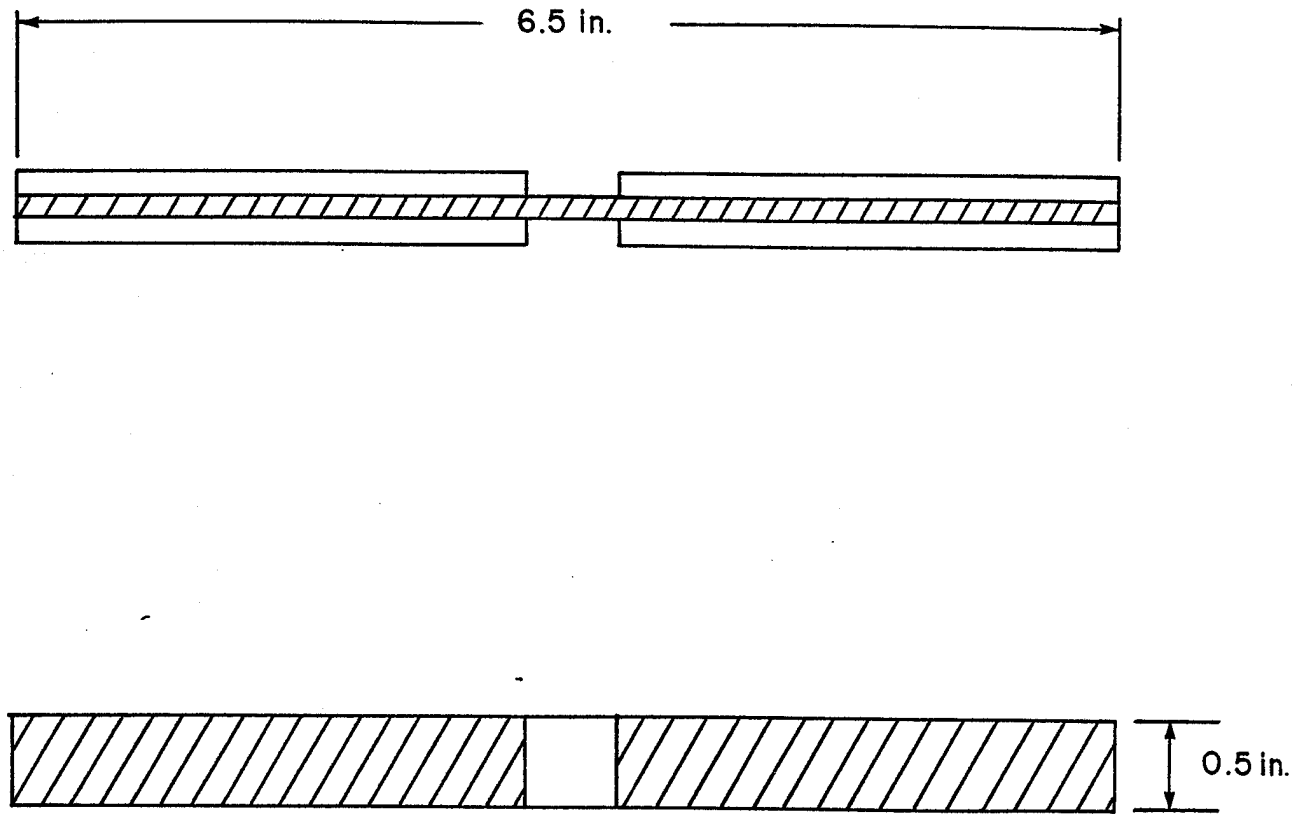

FIGURE 61. COMPRESSION TEST SPECIMENS

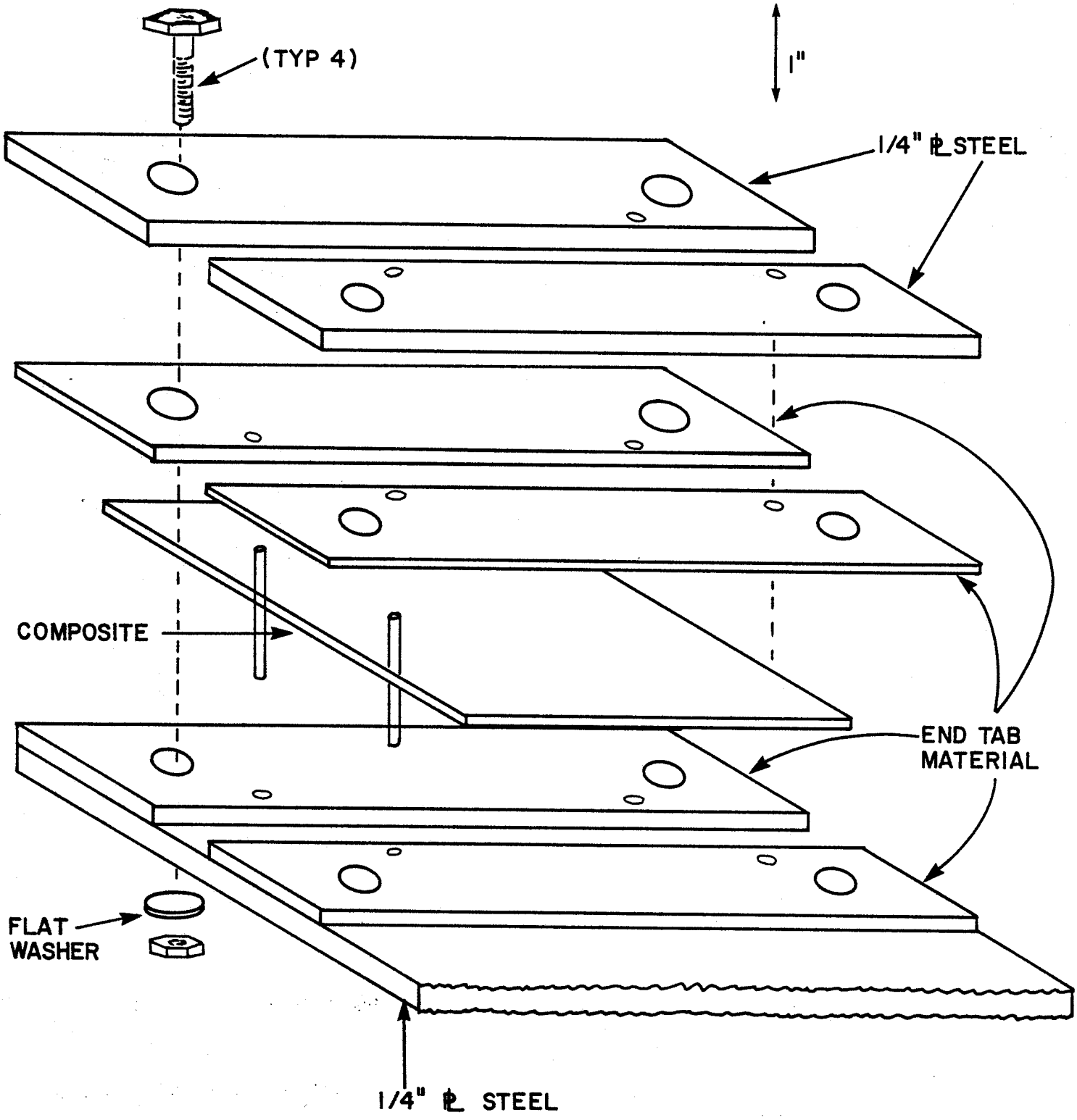

FIGURE 62. COMPRESSION END TAB BONDING FIXTURE

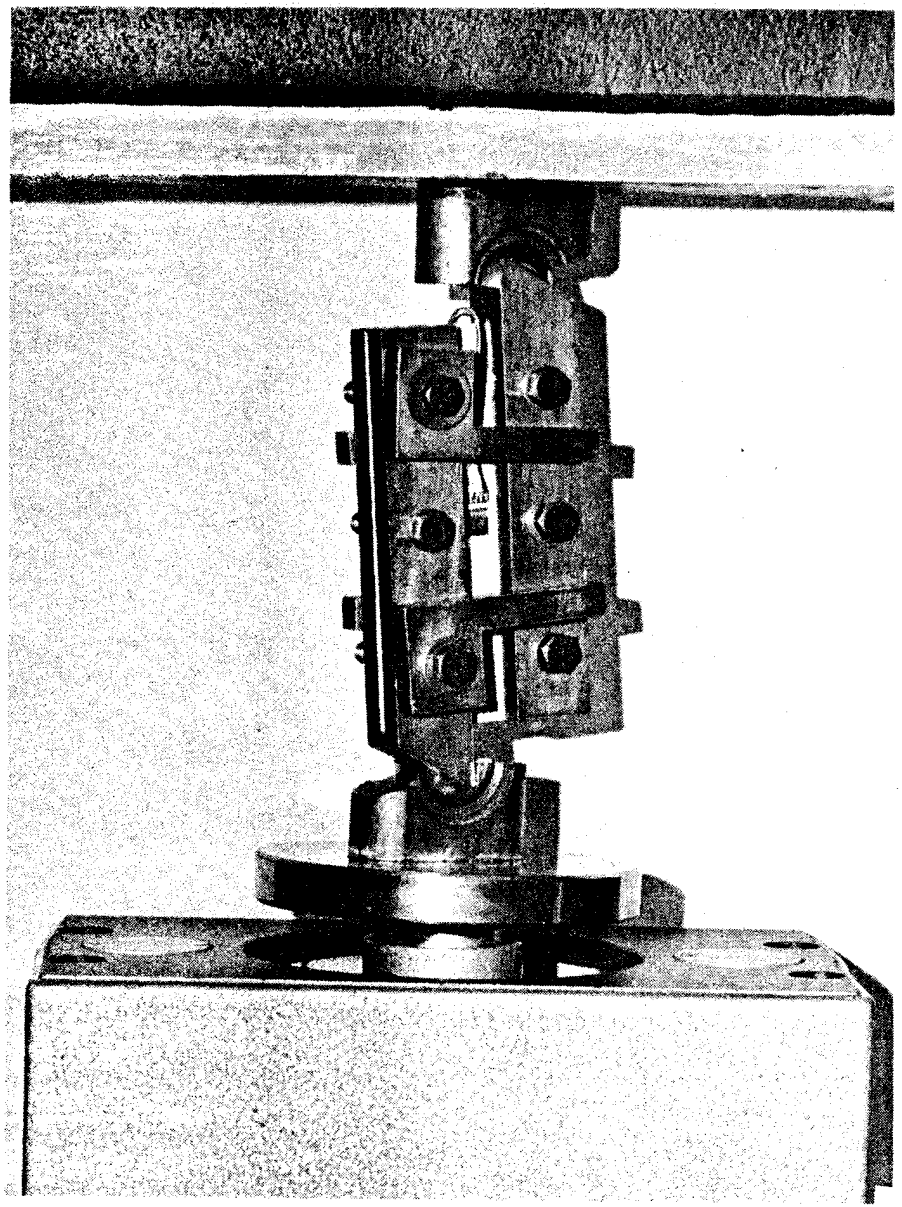

FIGURE 63. TWO RAIL SHEAR TEST - TENSILE

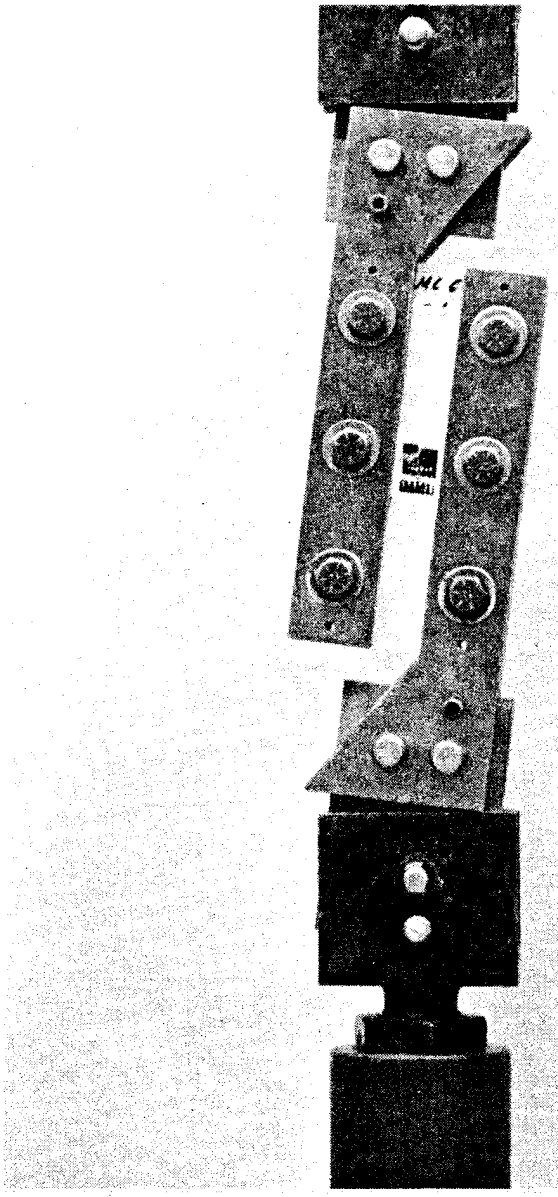

FIGURE 64. TWO RAIL SHEAR TEST

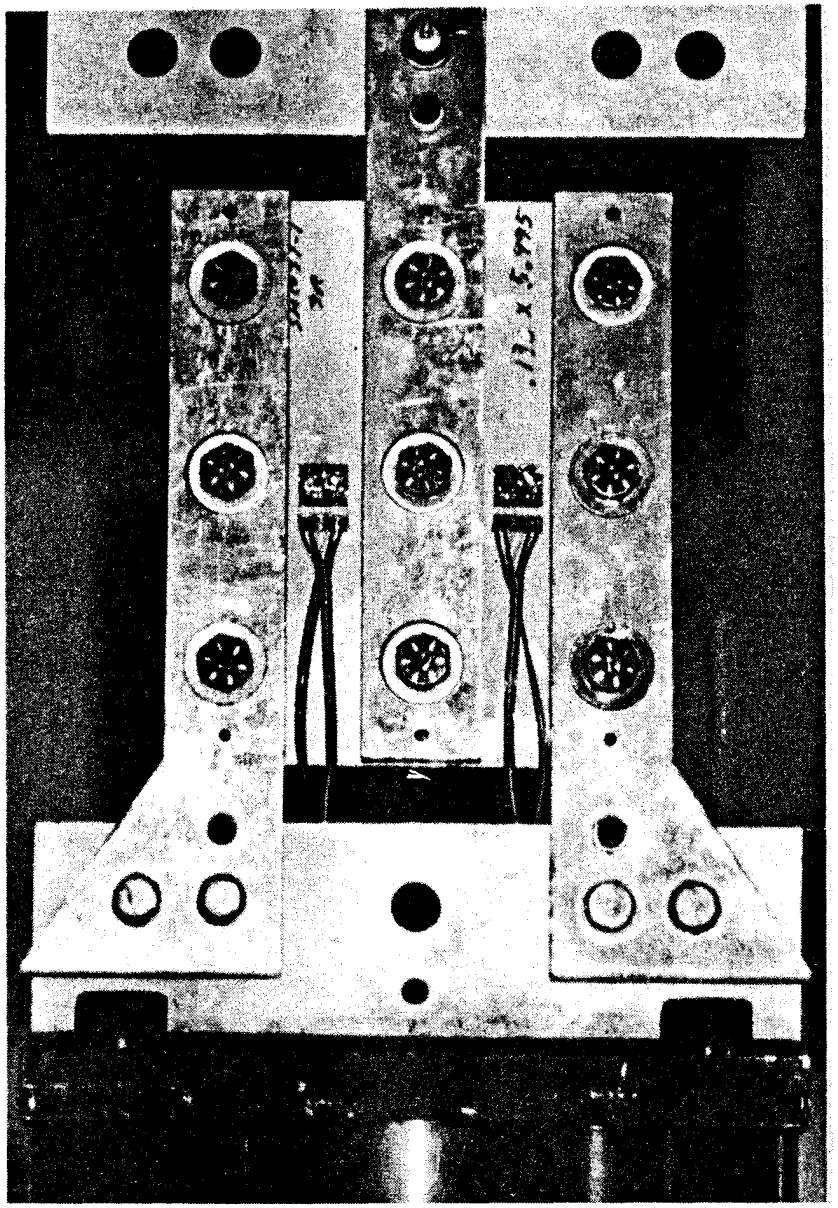

FIGURE 65. THREE RAIL SHEAR TEST

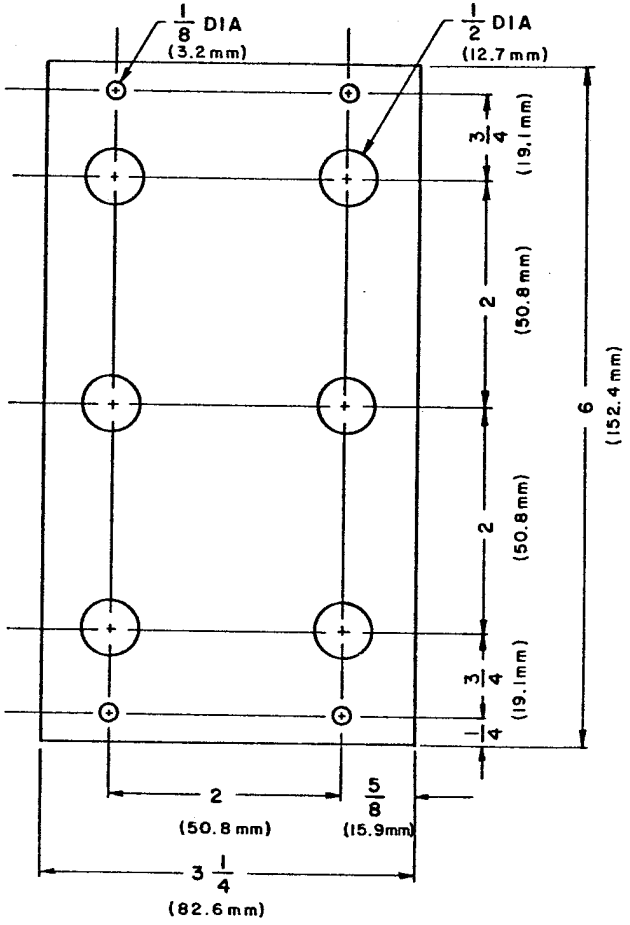

FIGURE 66. TWO RAIL TEST SPECIMEN

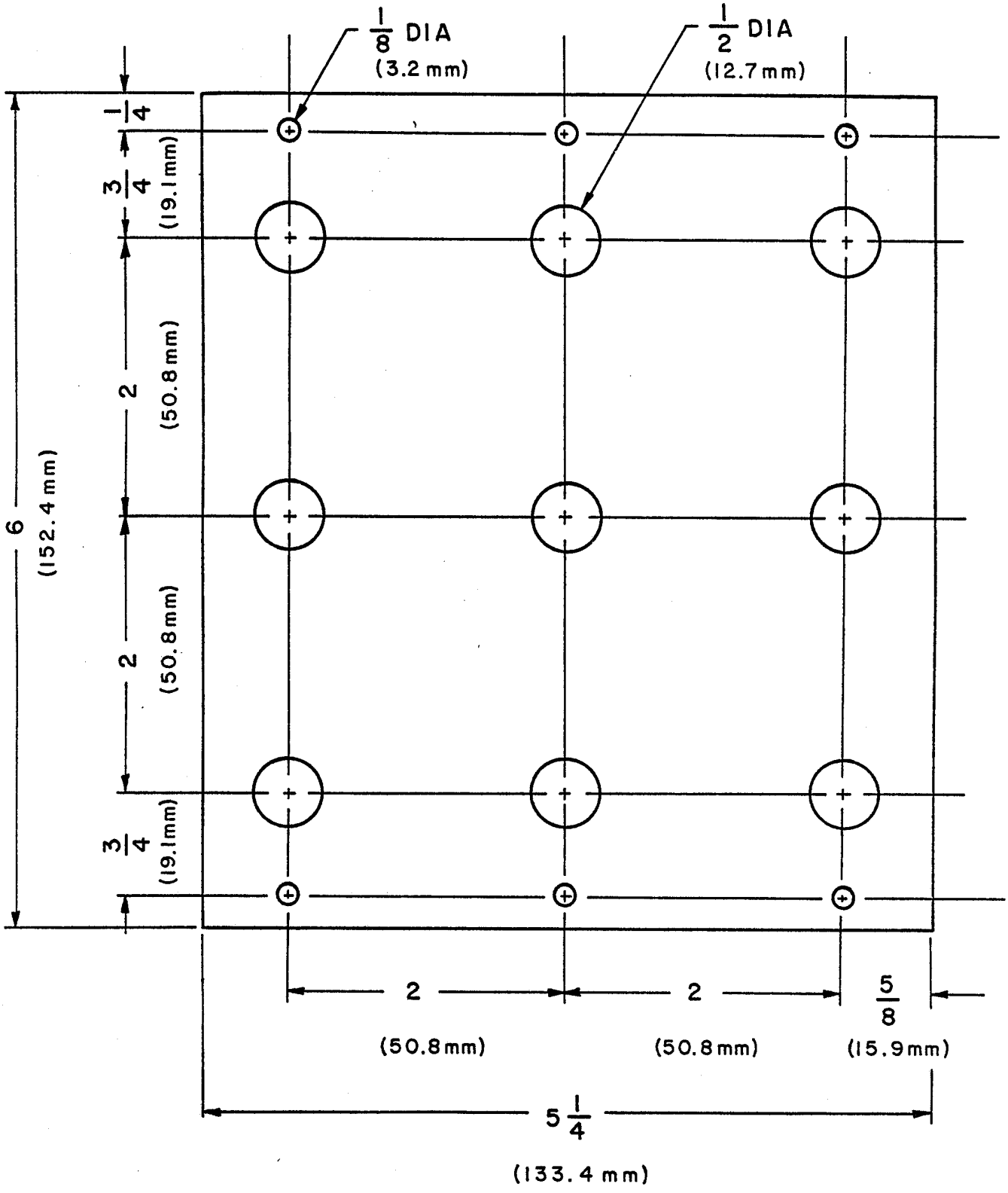

FIGURE 67. THREE RAIL TEST SPECIMEN

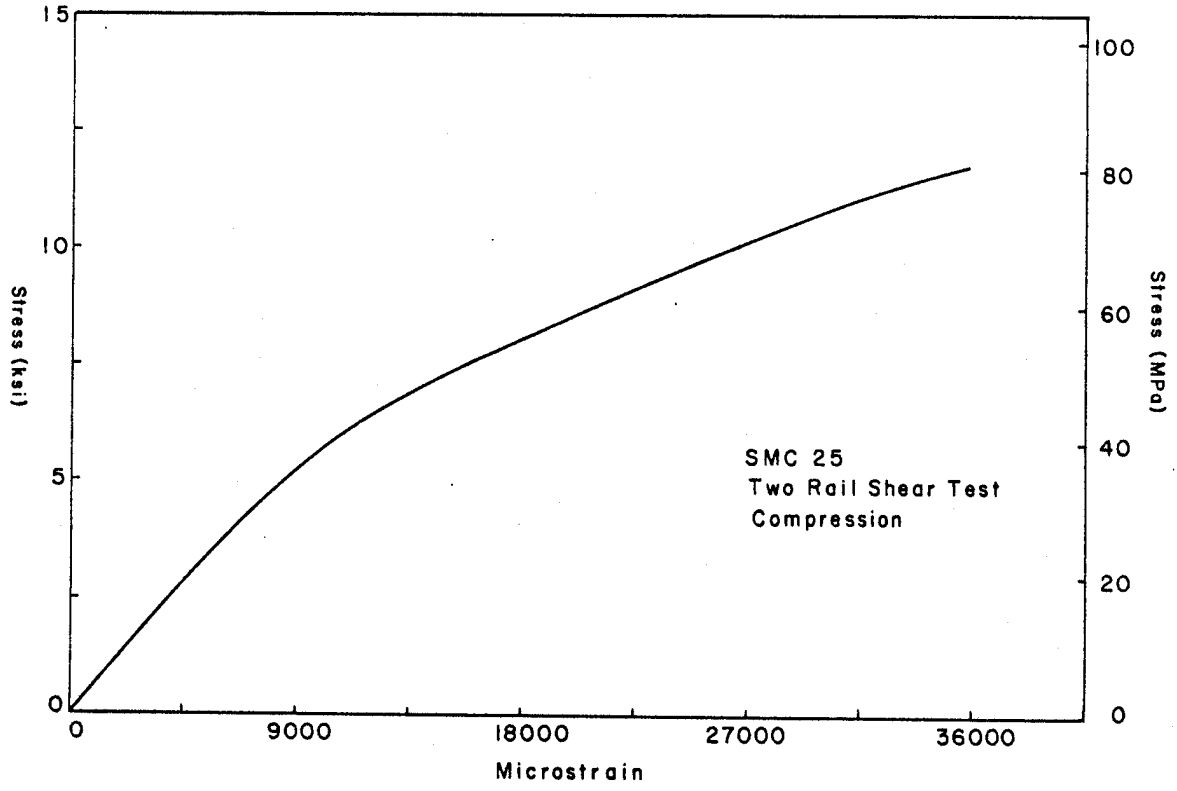

FIGURE 68. SHEAR STRESS-STRAIN RESULTS - TWO RAIL COMPRESSION SMC-25

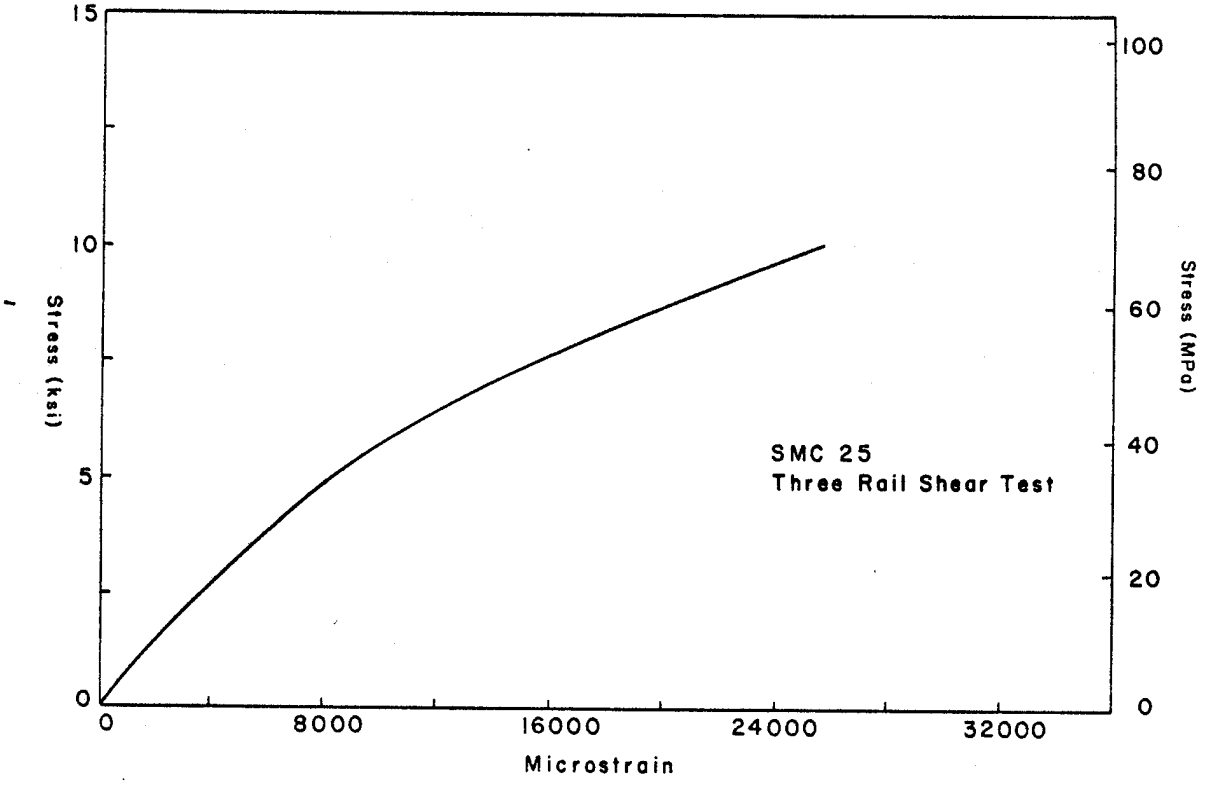

FIGURE 69. SHEAR STRESS-STRAIN RESULTS - THREE RAIL SMC-25

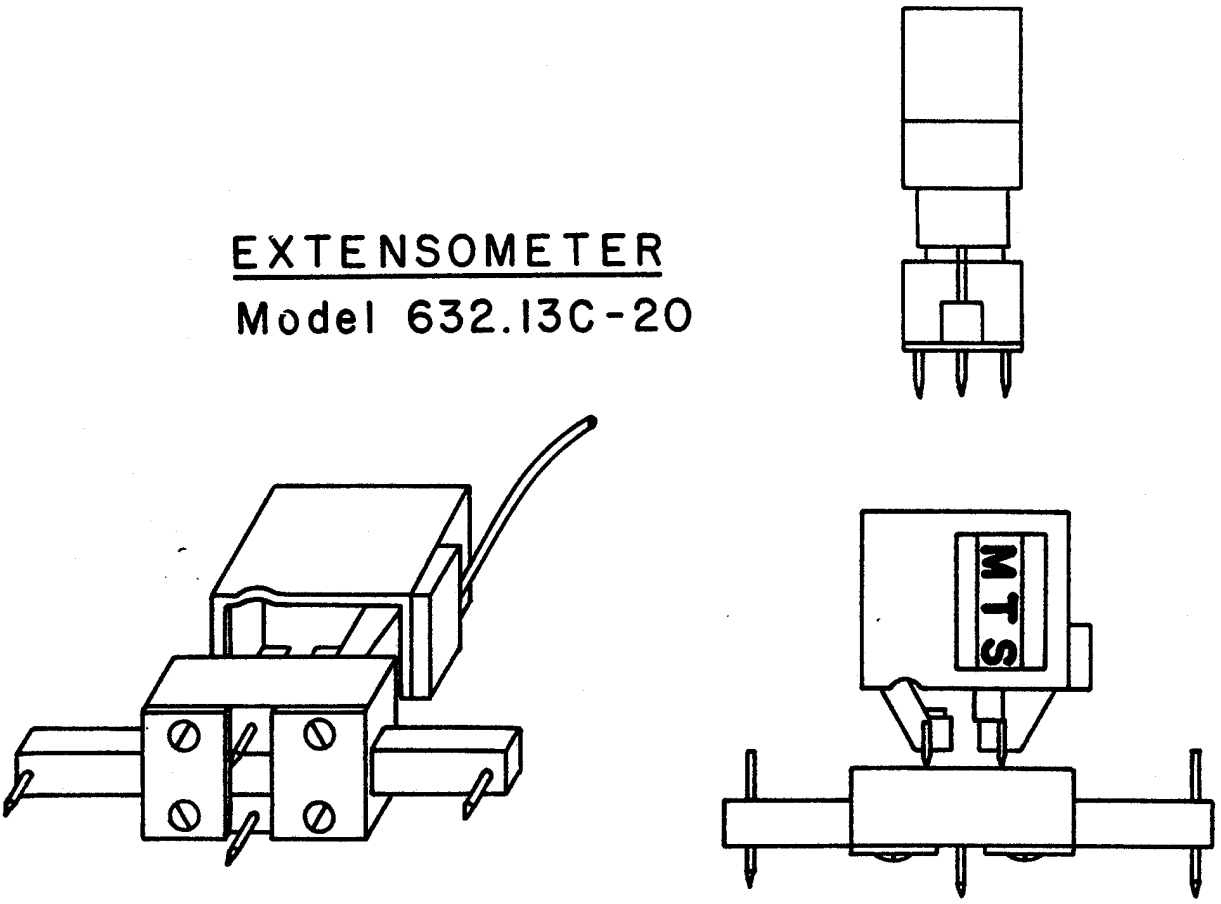

FIGURE 70. SHEAR STRAIN EXTENSOMETER

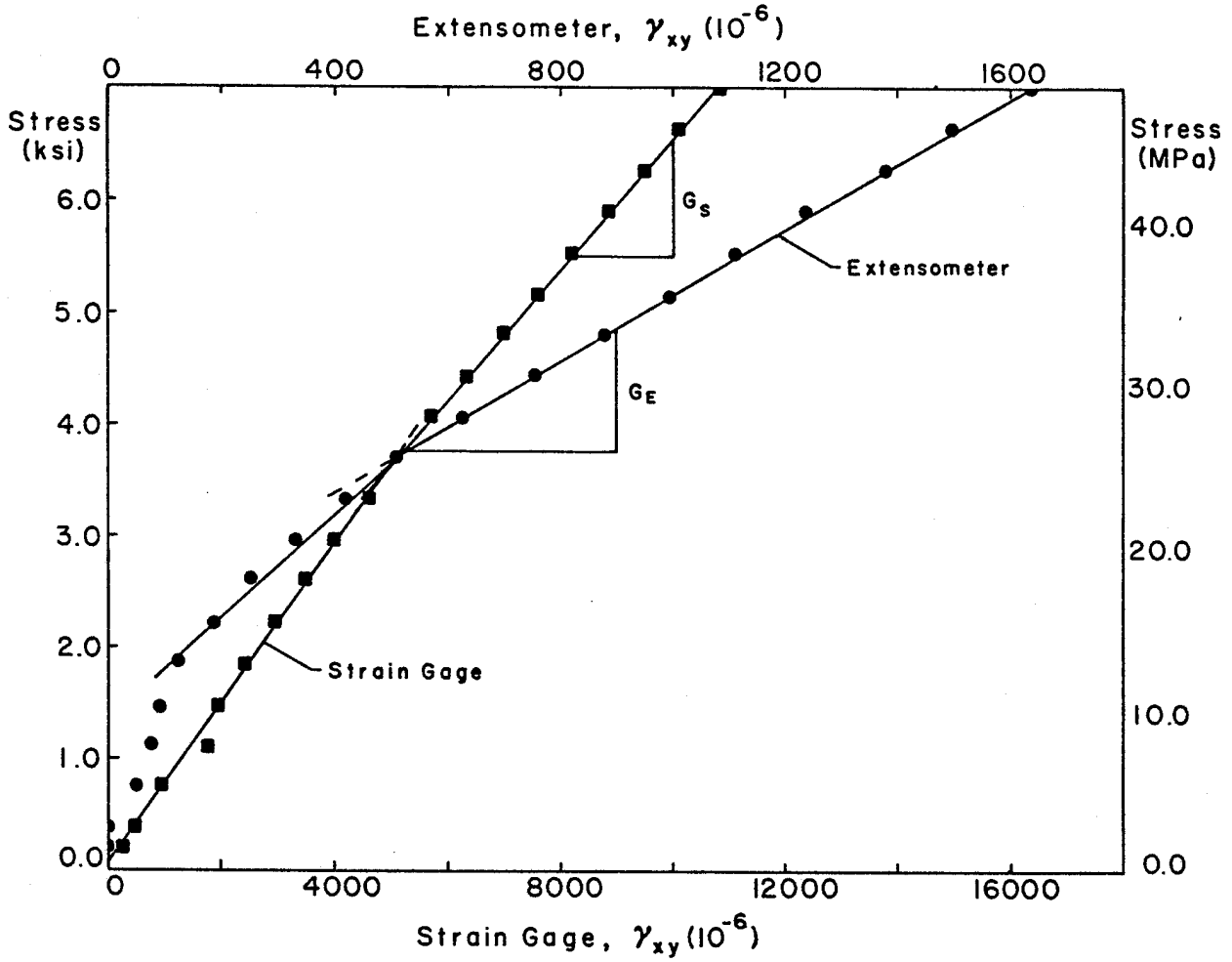

FIGURE 71. STRAIN GAGE VERSUS EXTENSOMETER DATA

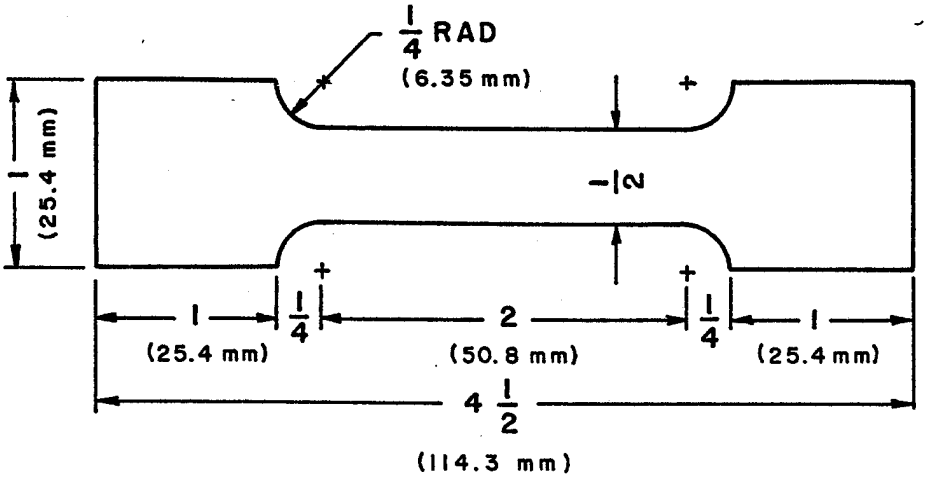

Thickness - 1/8 (3.2 mm)

FIGURE 72. TENSILE STRAIN RATE TEST SPECIMEN

IZOD IMPACT TEST SPECIMEN

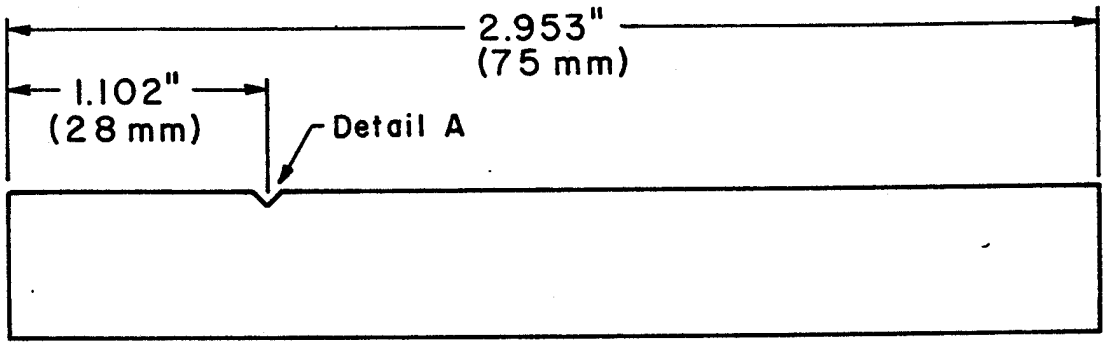

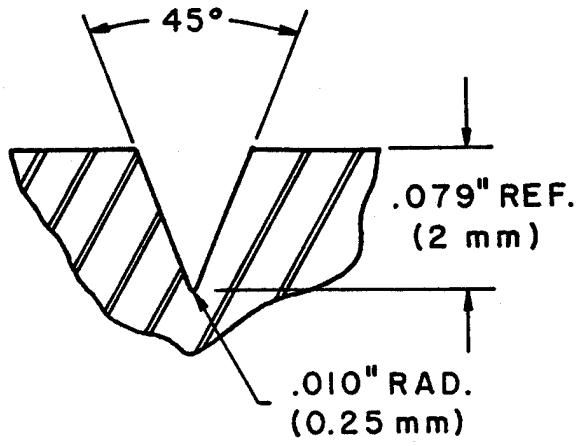

Detail A

FIGURE 73. IZOD IMPACT TEST SPECIMEN

Izod Impact Test Results

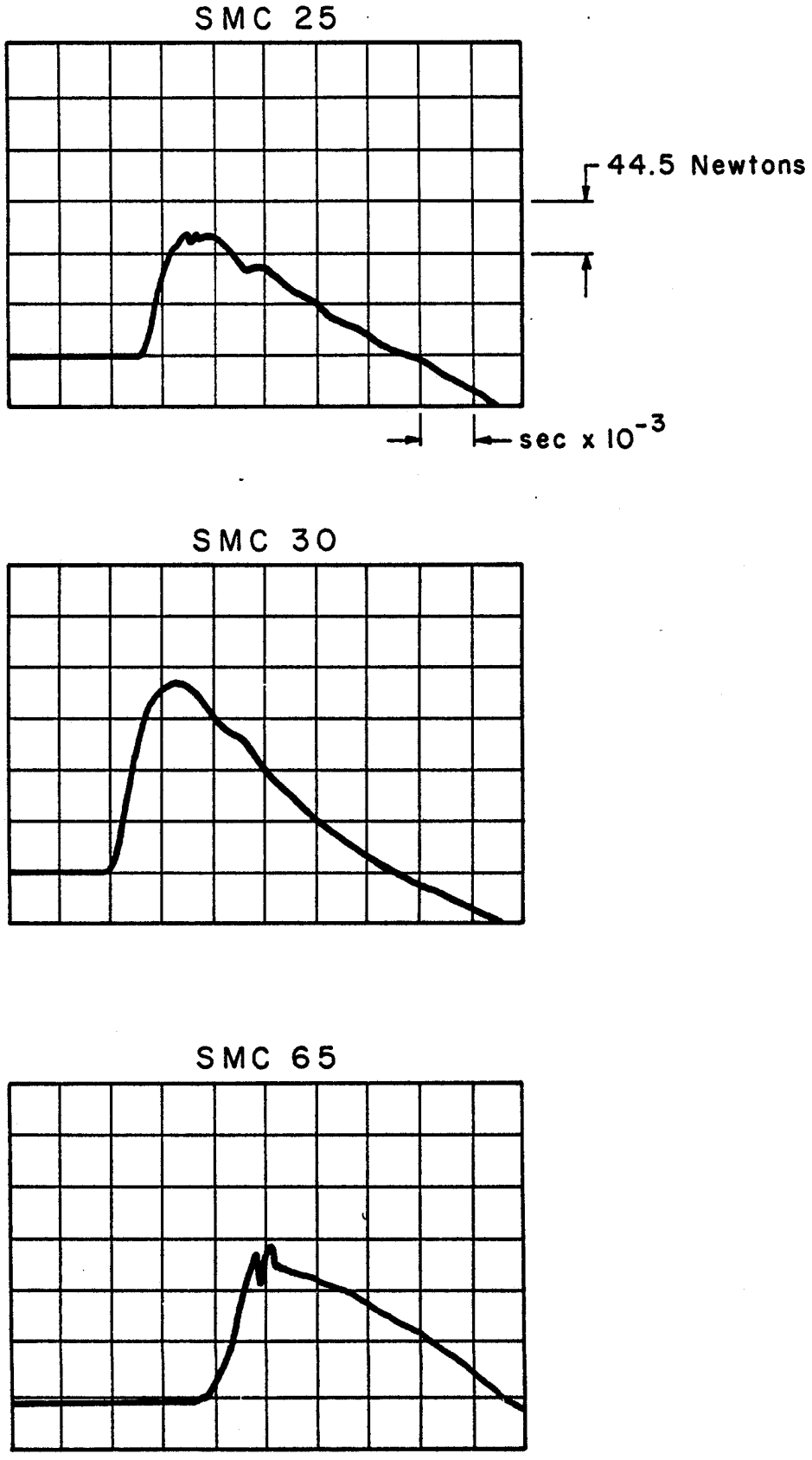

FIGURE 74. IZOD IMPACT TEST RESULTS

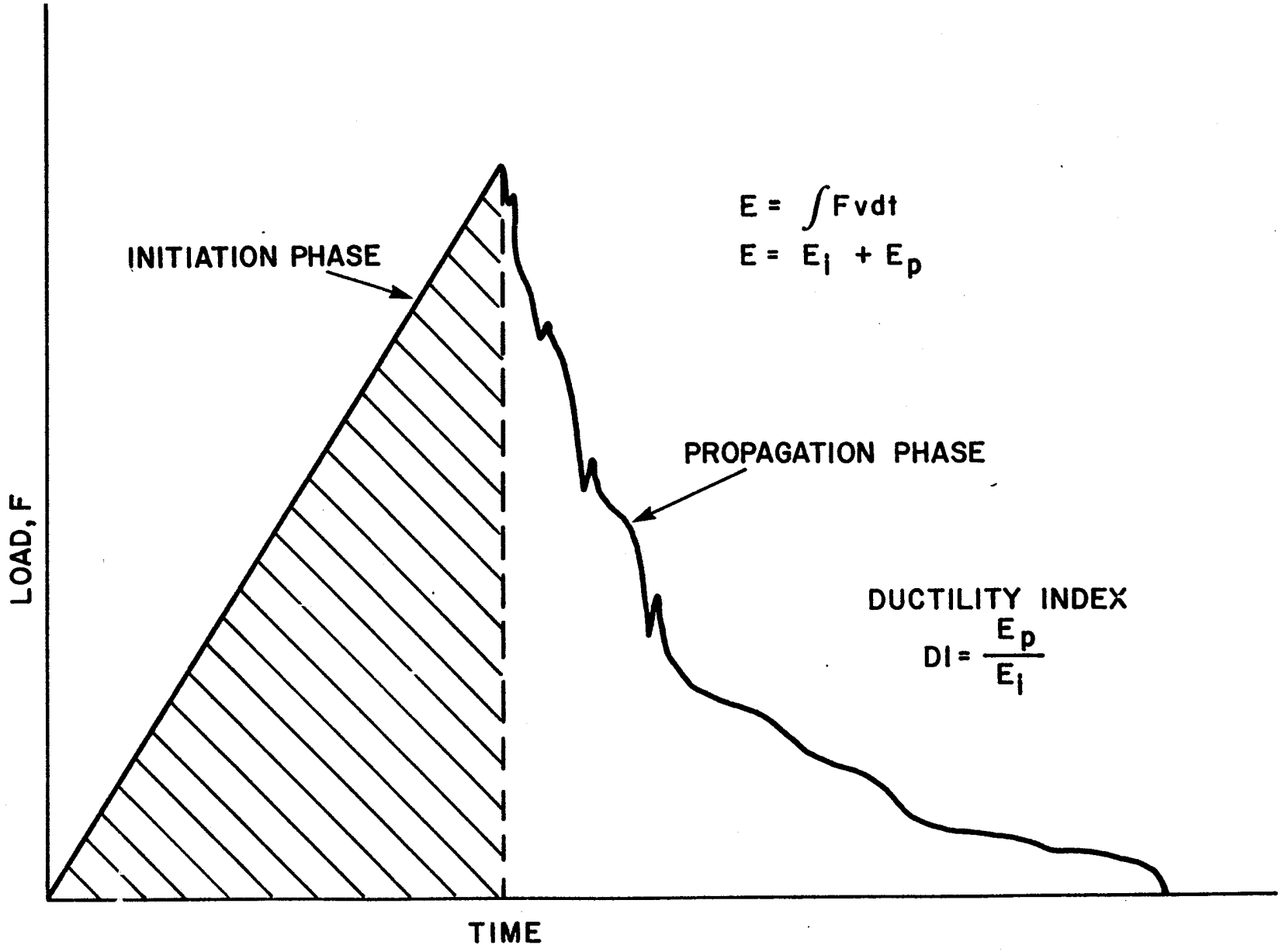

FIGURE 75. SCHEMATIC REPRESENTATION OF LOAD HISTORY IN IZOD IMPACT TEST

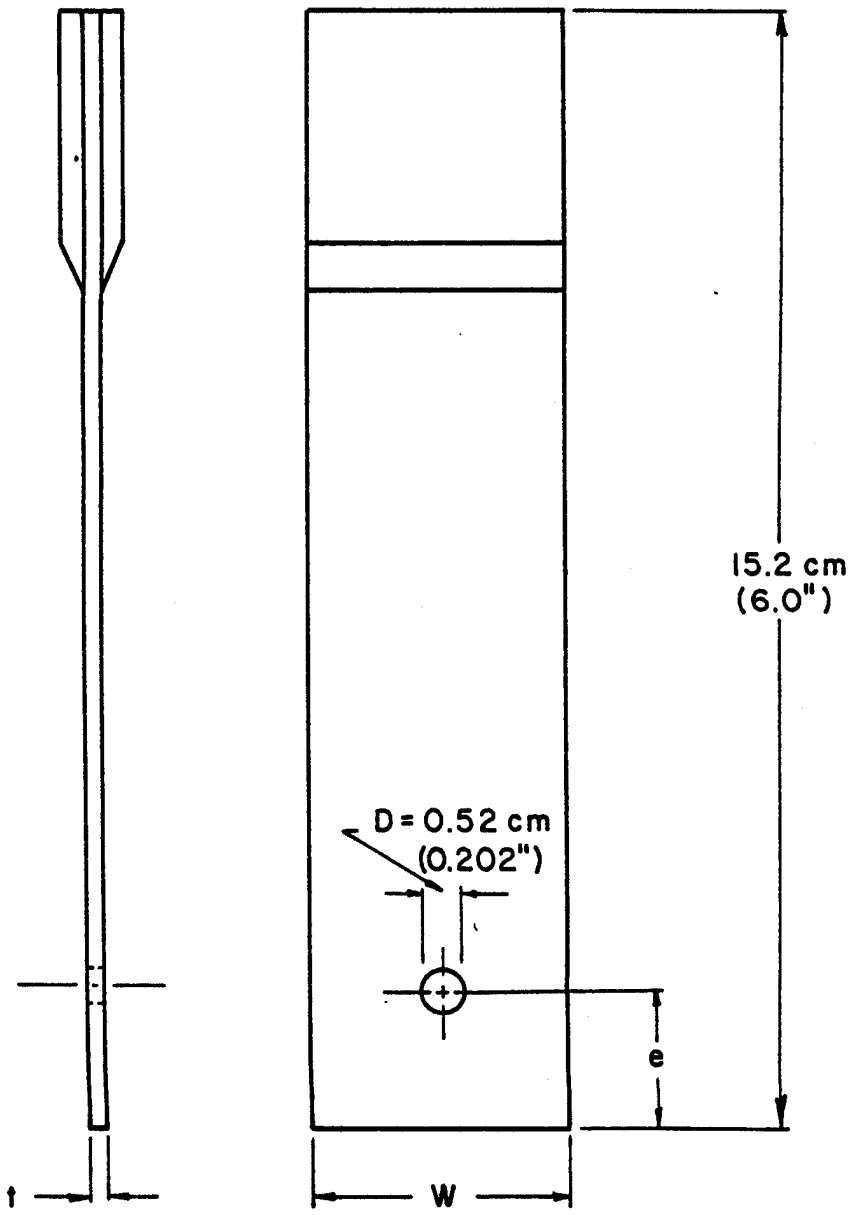

FIGURE 76. BOLTED JOINT TEST COUPON GEOMETRY

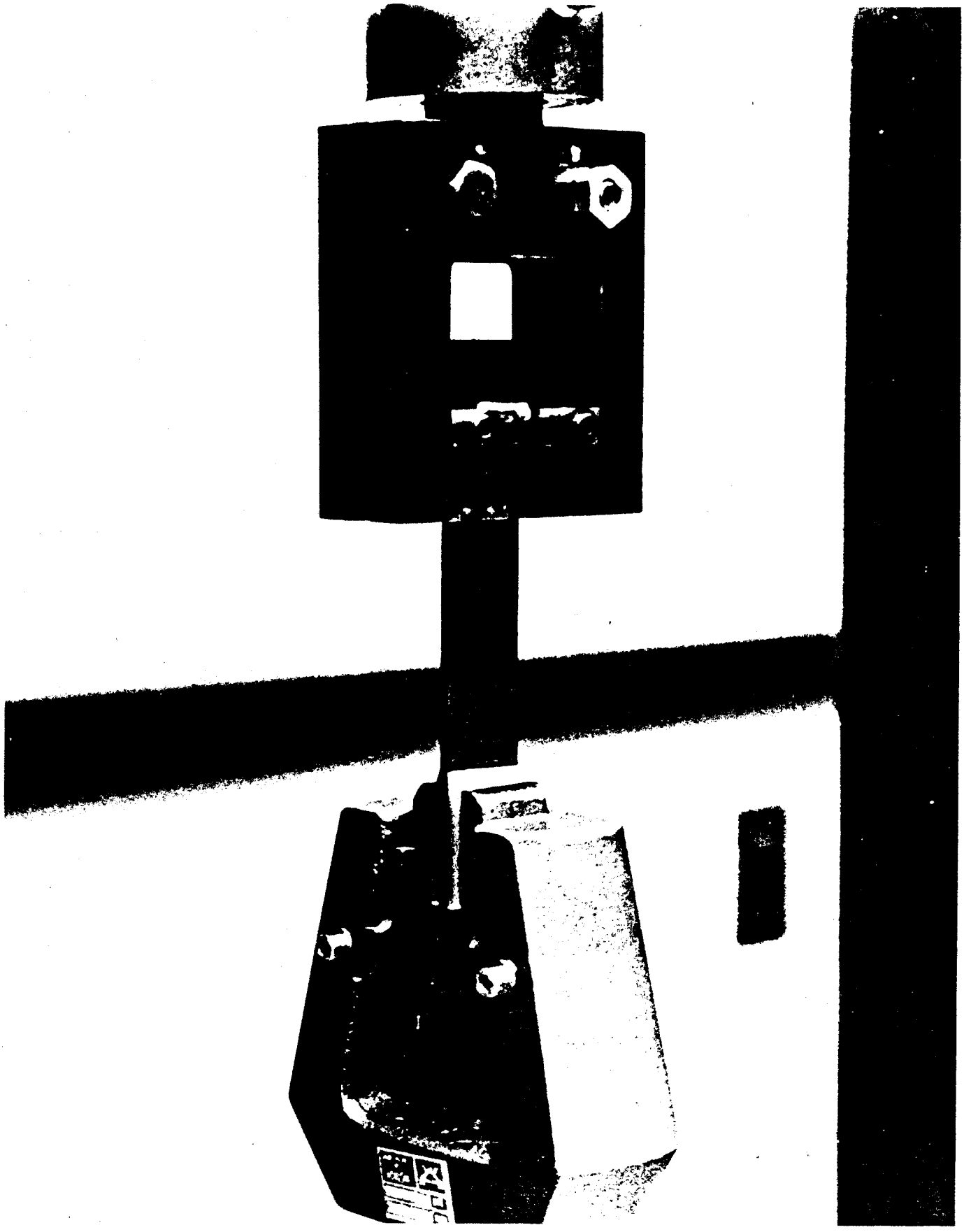

FIGURE 77. BOLTED JOINT CLEVIS FIXTURE

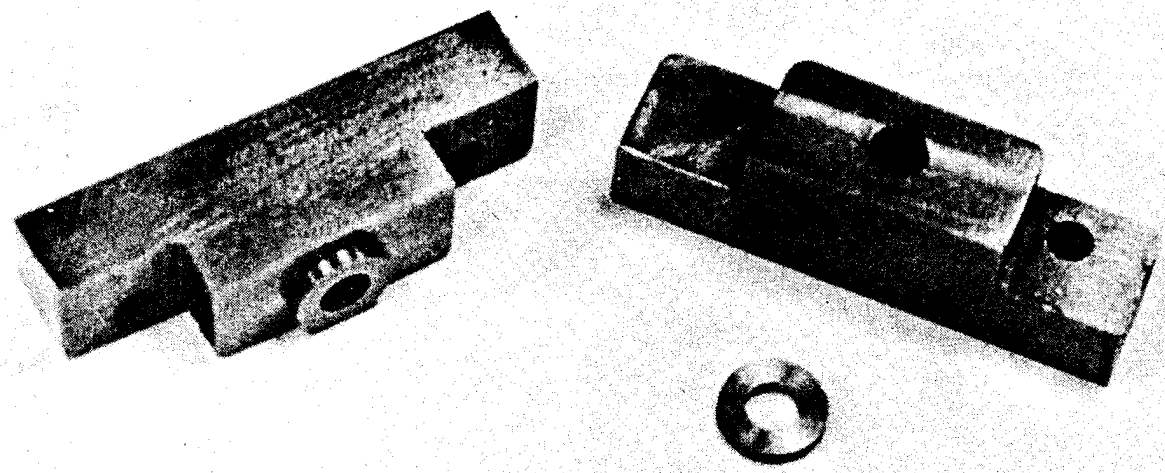

FIGURE 78. BOLTED JOINT - OUT OF PLANE CONSTRAINTS

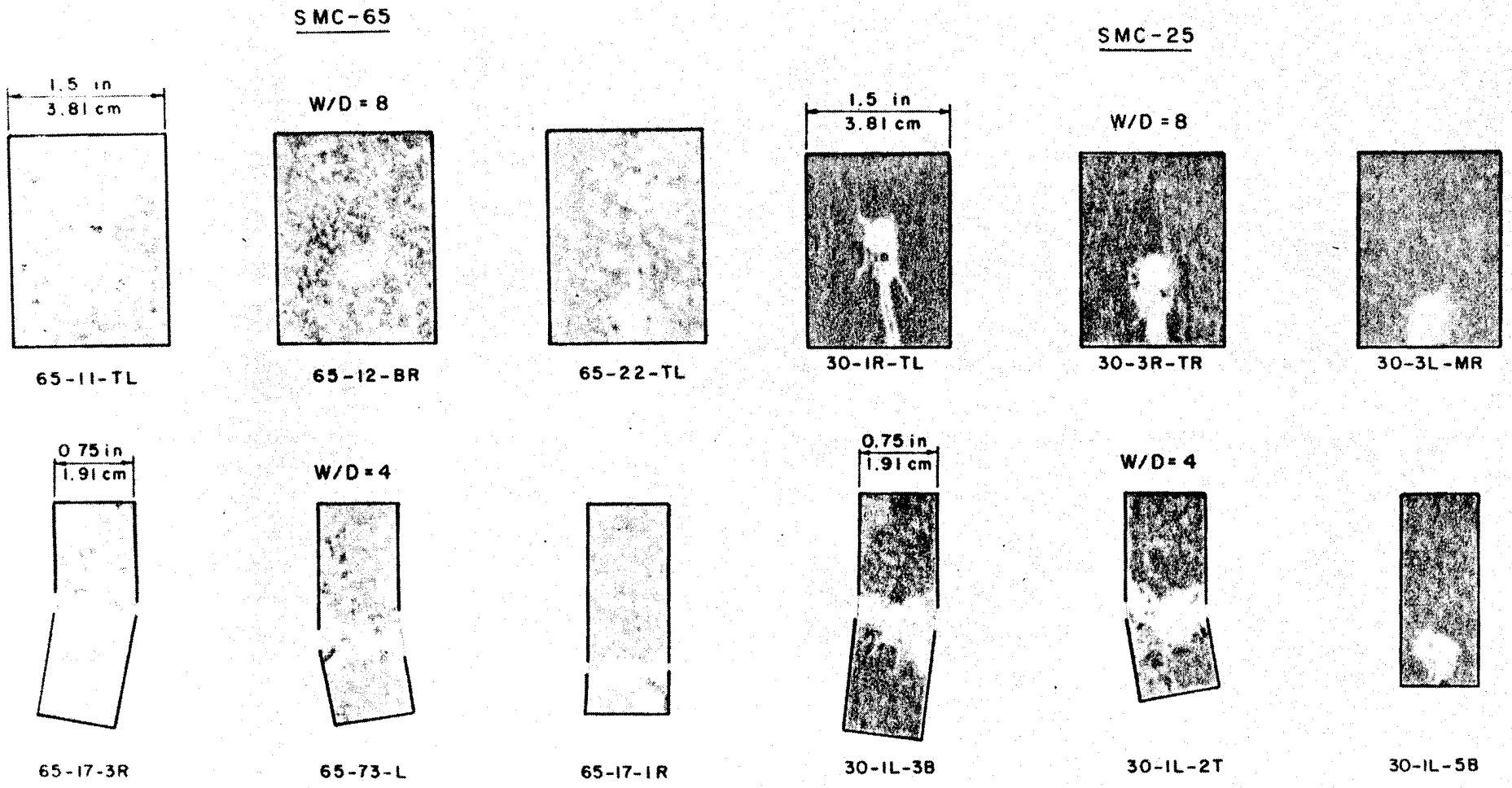

FIGURE 79. BOLTED JOINT FAILED SPECIMENS - TYPICAL C-SCANS

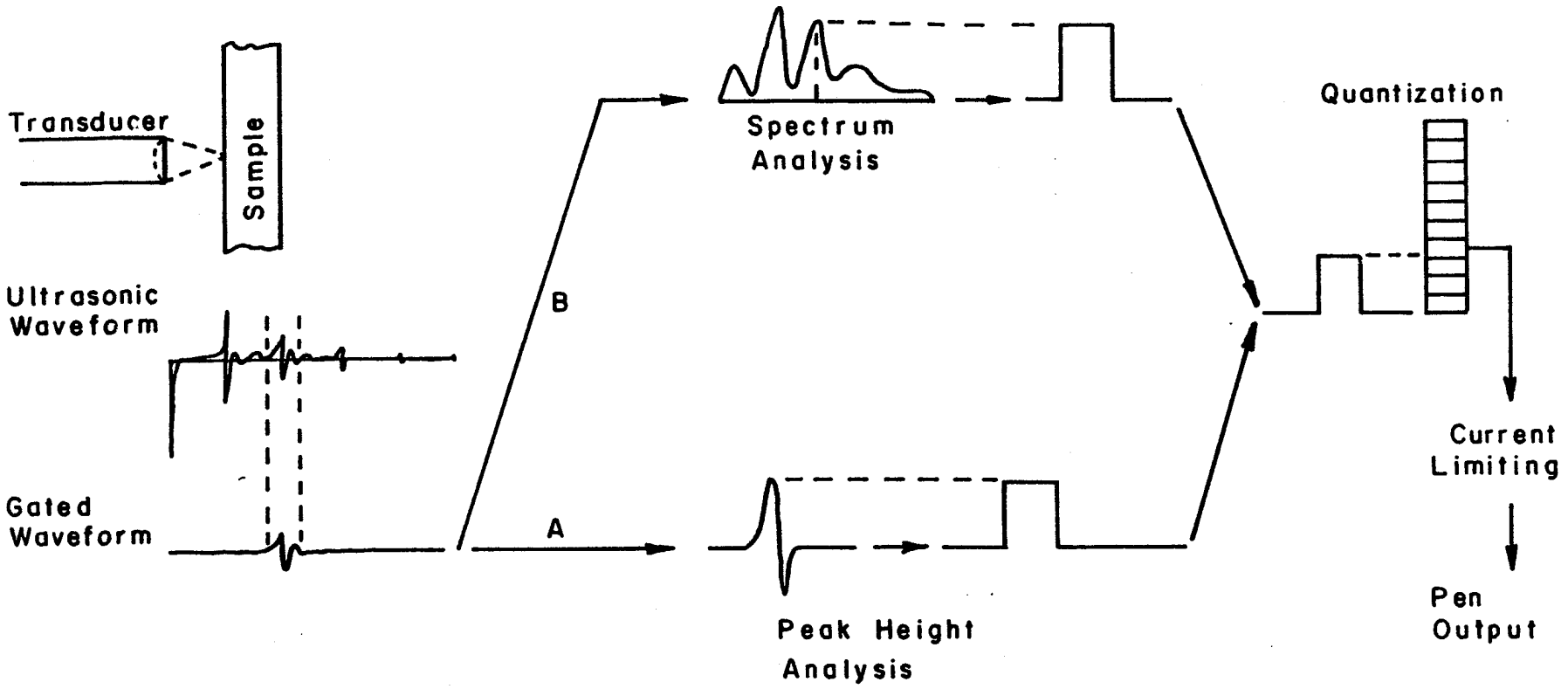

FIGURE 80. WAVEFORM ANALYSIS FOR ULTRASONIC C-SCAN

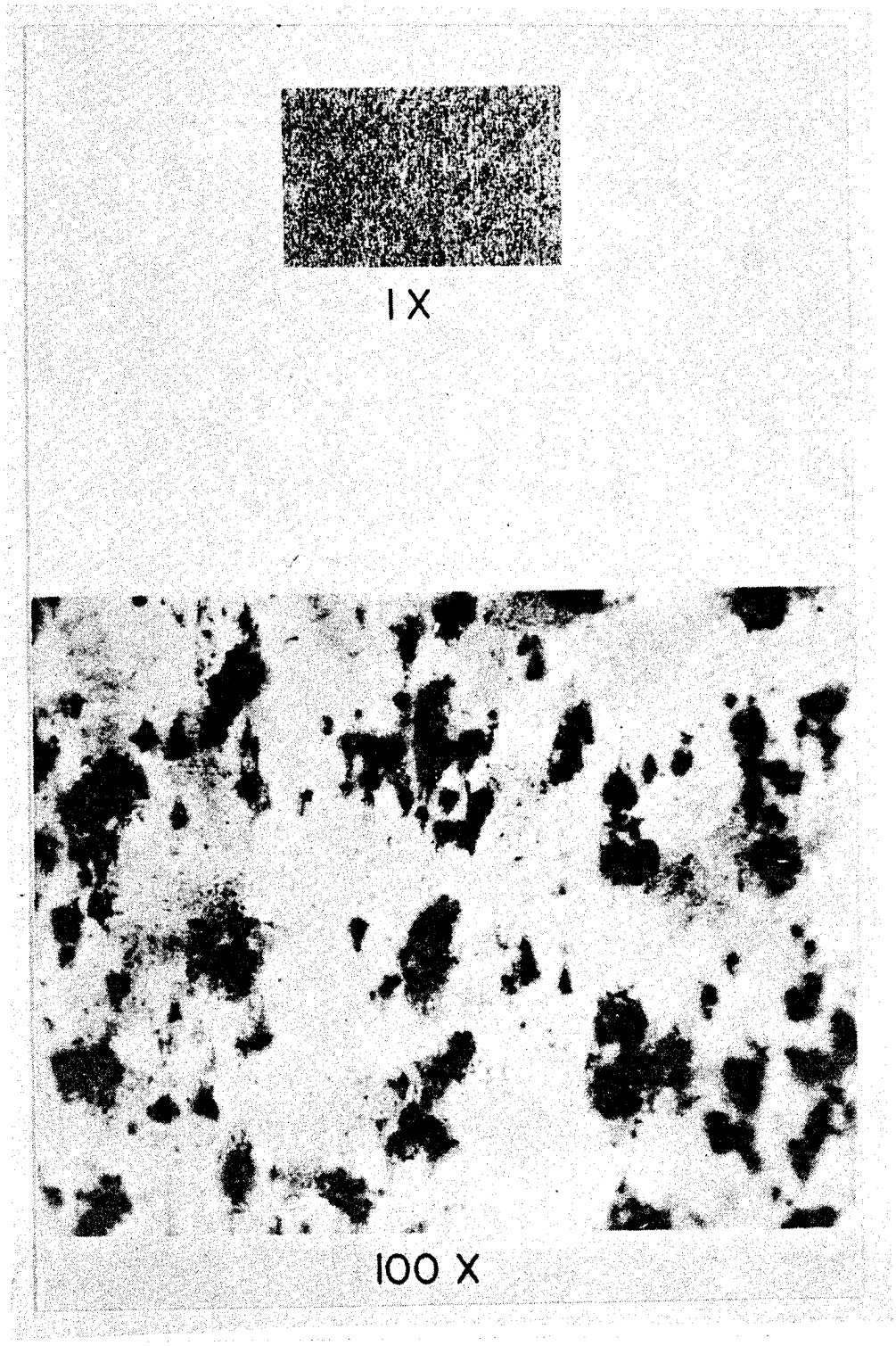

FIGURE 81. C-SCAN IMAGE COMPOSITION

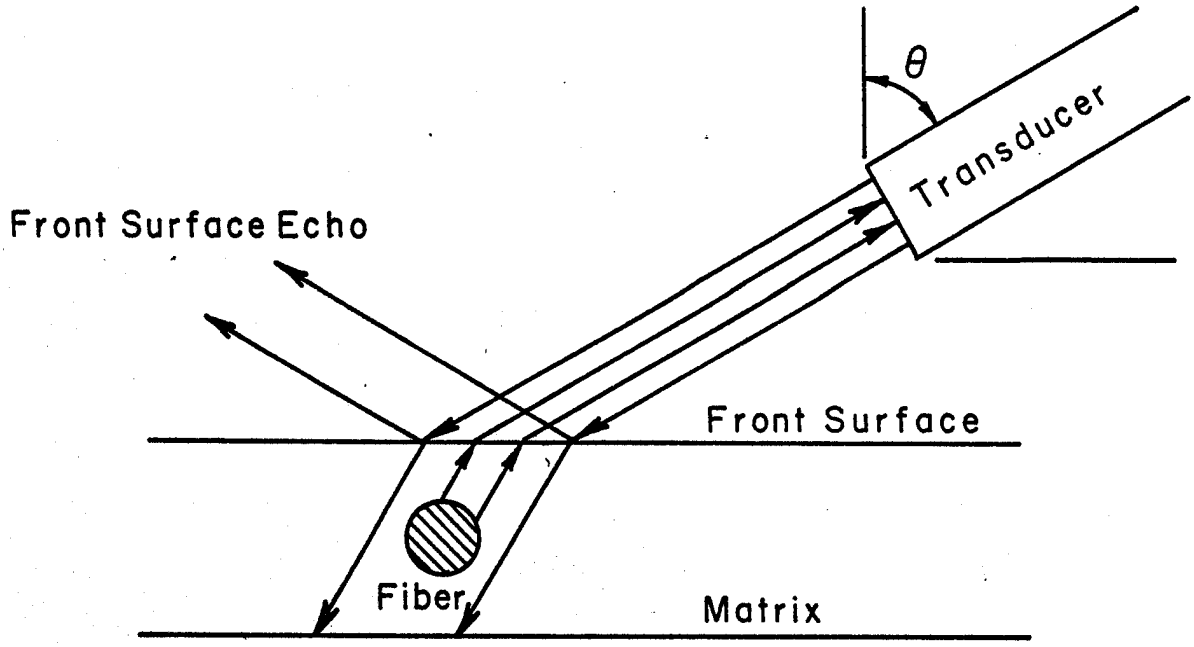

FIGURE 82. DARK FIELD WAVE REFLECTION

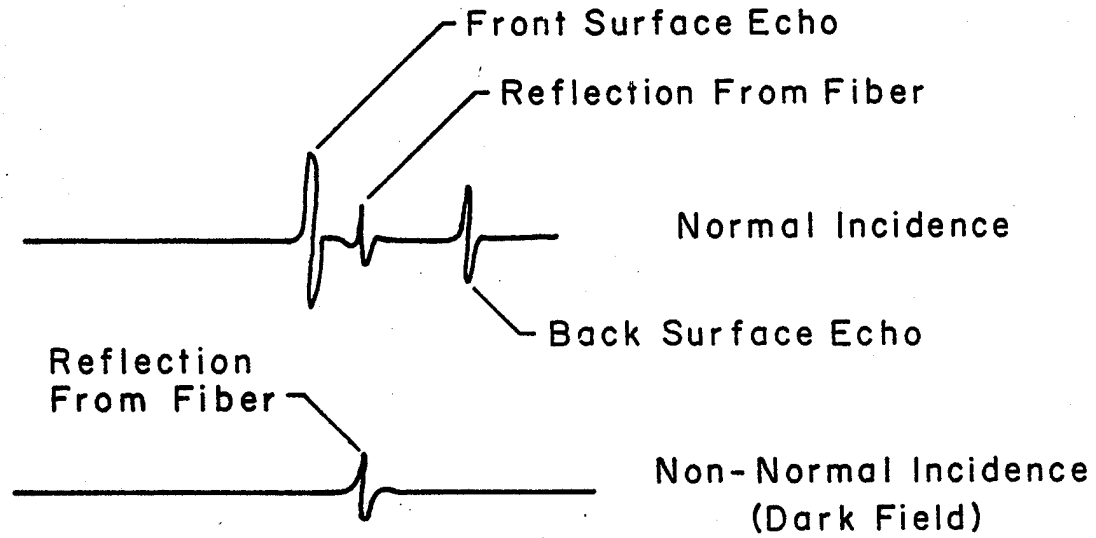

FIGURE 83. DARK FIELD WAVE FORM

UNIVERSITY OF DELAWARE
NEWARK, DELAWARE
19711

CENTER FOR COMPOSITE MATERIALS
107 EVANS HALL
PHONE: 302-738-2310

Center for Composite Materials Research Report

Enclosed is a copy of the latest Research Report from the University of Delaware Center for Composite Materials, Report No. 80-5, 80-7, 80-10*.

Extra copies may be ordered from:

Center for Composite Materials -- Report
University of Delaware
208 Evans Hall
Newark, Delaware 19711

*NOTE: CCM-80-9 not yet available.